Title	A Study Of Weak Nuclear Response By Nuclear Muon Capture
Author(s)	Hashim, Izyan Hazwani Binti
Citation	大阪大学, 2014, 博士論文
Version Type	VoR
URL	https://doi.org/10.18910/52302
rights	
Note	

OSAKA UNIVERSITY

A Study Of Weak Nuclear Response By Nuclear Muon Capture

A thesis submitted in partial fulfillment
for the degree of

Doctor of Philosophy

by

IZYAN HAZWANI BINTI HASHIM

in the
Department of Physics
Graduate School of Science

December 2014

Abstract

Nuclear matrix elements (NMEs) for double beta decays (DBD) are crucial for extracting fundamental neutrino properties from DBD experiments. In order to study the DBD NMEs, single β^+ and β^- NMEs are required. The present research developed an experimental approach towards the determination of weak nuclear response (square of the NME) for the importance of fundamental properties of neutrinos. Hence, the present research aims at experimental studies of muon capture strength distributions, the β^+ side responses, to help/confirm theoretical evaluation for DBD NMEs.

Nuclear muon capture induced the excitation of the nucleus by compound nuclear formation and de-excitation of the compound nucleus by neutron emission. However, captures on the excited states of nucleus are preferable in comparison with capture on the ground state. The gamma rays accompanied the neutron emission is from the transitions from an excited state to the ground state. The production of isotope after muon capture evaluated the capture strength via observation of nuclear gamma rays and X-rays. We used the enriched molybdenum thin film in our first measurement at J-PARC, MLF.

The statistical neutron decay calculator explained the theoretical approach with the limitation to the excitation energy which corresponds to the Q-value of muon captures. Neutron binding energy is the threshold energy for emission of neutron and their cascade process after nuclear excitation is explained by emission of the fast pre-equilibrium neutrons(PEQ) and evaporating neutrons(EQ) fraction.

The second part discusses the experimental observation of isotope production after (μ,xn) reaction on ^{100}Mo target with x = 0,1,2, ... neutron emission. The isotopes are identified by their gamma-rays following the capture reaction and the observed half-life from the decay curve.

The final phase elaborates the comparison of previous feasibility test on ^{Nat}Mo and the current ^{100}Mo experimental observations with the neutron statistical calculations for both natural and enriched Molybdenum targets. From the population of isotopes produced by the reaction, one may get the muon-capture strength distribution, which can be used to help deduce the nuclear responses relevant to neutrino less double beta decays.

Acknowledgements

It is my exquisite pleasure to consummate doctor course and take a degree of Doctor of Philosophy in Osaka University. I would like to express my gratitude here to many people supported this accomplishment for over 3 years of my stay.

First, I would like to show my greatest appreciation to Prof. Yoshitaka Kuno who is my supervisor for the valuable advices and persistent helps from him to ameliorate my study. My deepest appreciation goes to Prof. Hiroyasu Ejiri who first suggested the muon capture reaction for the study of neutrino-less double beta decay. He lets me know how interesting particle physics is. His valuable discussions, advices, and incisive comments help me a lot in my study and experiment. My heartiest thanks to Associate Prof. Akira Sato who taught me how to perform the experiments and helping out in completing the details of the analysis. Associate Prof. Tatsushi Shima and Dr. Keiji Takahisa supported me in RCNP, Osaka University. Their technical advice, educational comments and useful feedbacks have been a great help to me to understand and operate the detectors and apparatus on-site.

I would like to thank the collaborators in MuCID, Dr Hideyuki Sakamoto, Associate Prof. Kazuhiko Ninomiya, Prof. Atsushi Shinohara, Yuko Hino, Nguyen Duy Thong and Nam Tran Hoai. Under their mentorships, I learnt many things besides physics. My intellectual debt is especially dedicated to Dr. Itahashi Takahisa who helped and supported me in the analytical processes. In addition, my life in Osaka has been enjoyable together with them and also the students in Kuno Laboratory. These three years has been a great pleasure, priceless and precious memory. I will always treasure them in my life.

I am also gratefully appreciate the financial support of UTM and KPM that made it possible for me to complete my challenge.

Finally, I would like to express my gratitudes to my husband and family for their moral supports and encouragements.

Contents

List of Figures

Chapter 1

Introduction

The study of neutrino fundamental properties are crucial because of its neutral charge and unknown mass. In a radioactive decay, W.Pauli has observed a non-conserved energy apparent energy which contributed to the postulation of neutrino as a neutral particle. The discovery of neutrino 20 years later at the nuclear reactor augmented the interest to study the basic properties of neutrino [1]. The fundamental properties of neutrino and astro-neutrino nuclear interactions studied by single β decay, $\beta\beta$ decay, the inverse β decay and neutral current nuclear excitations experiments.

Up till now, the accord of neutrino properties such as its mass hierarchy, or it's characterised as Majorana or Dirac neutrino etc. are still ambiguous resulting from the unknown absolute neutrino mass scale. This mass scale information procured from the transition rate of $0\nu\beta\beta$ decay experiment. However, this experiment is beyond the standard model(SM) and a very rare process. Moreover, the accurate value of the coupling constant and correlation parameters are not well known causes the nuclear matrix element(NME) to be undetermined.

This research report will provides the new information for the NME by studying the β^+ side of the double beta decay (DBD) using the nuclear muon capture reaction. We aim to provide the theorist the strength distribution of muon capture reaction for understanding the coupling constants and correlation parameters relevant to DBD experiments. This chapter will briefly explains the neutrino physics background, experimental probes for the neutrino studies and the advantages of weak nuclear probes.

1.1 Neutrino Physics

Neutrinos passing through the universe like a mere spectators. Their discovery become unnoticed due to their ability to travel through the earth without any interaction. Even though, after half a century, we still know less about them. Once the interaction between a neutrino and weak force known as the weak interaction was realised, neutrino has an insignificant gamble of interacting with anything.

In 1930, W.Pauli proposed that the apparent violation of energy and momentum conservation can be easily avoided by postulating another particle produced along with the electron in beta decay. This elusive particle has no charge like neutron, almost no mass and has 1/2 spin. In three years later E. Fermi [2] developed a beta decay theory based on the interaction between neutrino and other particles.

$$n \rightarrow p + e^{-} + \bar{\nu}_e \tag{1.1}$$

E.Fermi established the theoretical equations of beta decay by assuming the neutrino mass is zero considering the empirical energy spectrum of decay electron. The zero mass neutrino was introduced into the SM. Their existence was unknown until 1956, after Clyde Cowan and Fred Reines performed an experiment at nuclear reactor [3]. Their experiment observed the cross sections of inverse beta decay of protons from fission fragment [1].

Later in 1962, L. M. Lederman, M. Schwartz and J. Steinberger detected the interactions of muon neutrino by spark chamber experiment. They concluded that there were more than one type of neutrinos exists. Fundamental properties of neutrino was aggressively studied since 1970s by double beta decay experiment, inverse beta decay and neutral current nuclear excitations [3] [1]. Consequently, the heaviest tau neutrino was discovered on 2000 by DONUT. The intense neutrino beam was fired on a target consists of iron plates with layers of emulsion sandwiched between them to produce tau lepton which then subsequently decayed by leaving a characteristic track in the emulsion.

1.1.1 Dirac and Majorana Neutrino

In the SM framework, $2\nu\beta\beta$ decays are followed by two neutrino and anti-neutrino and thus the lepton number is conserved. Meanwhile, the $0\nu\beta\beta$ decays violated the lepton number conservation law by ΔL=2 with the decay associated with neutrinos and weak interaction beyond the SM. Majorana neutrino assume that the have masses and neutrino and anti neutrino posses the same energy. In order to establish that neutrino is a Majorana particle, one requires a measurement of decay rate, the data of neutrino oscillation and a good and reliable calculation of nuclear matrix element is very important [4] [5] [6]. However, it is important to clearly know the nuclear matrix element of the transition to yield the neutrino mass Eigen states and gives accurate information about nuclear structure. From Majorana and Dirac neutrino description, a mathematical representation is necessary to explain a peculiarity which does not exist in case of charged fermions.

Until 1995, only ν_L and $\bar{\nu}_R$ have been detected experimentally. The spin and momentum remain constant by charge conjugation, thus ν_L does not corresponds to the $\bar{\nu}_R$. However, they were related by CP operation which was responsible for the change of the sign of handedness $\nu_L^{CP} = \bar{\nu}_R$. In relativistic quantum theories, half integral spin fermions were described by 4 components spinor which gave solution to Dirac equation. The following mass term of Dirac and Majorana neutrinos are summarised from [7].

The left and right handed components of $\psi(x)$ are easily obtained by applying the P_L and P_R

$$\psi_L = P_L\psi \tag{1.2}$$

$$\psi_R = P_R\psi \tag{1.3}$$

The four components of Dirac field $\psi(x)$ is the sum of the Weyl Spinors (ψ_L and ψ_R) and the Dirac's field is represent by the following equation.

$$\psi(x) = \sum_{S=L,R} \int \frac{d^3p}{\sqrt{2\pi^2 2E}} (b_S(p) u_S(p) e^{-ipx} + d_S^{+}(p) \nu_S(p) e^{ipx}), \tag{1.4}$$

b_S and d_S^{+} were the annihilation operators and their corresponding creation operators, while u_S and ν_S were independent basic spinors.

Assuming that ν_R existed and they are distinguishable as ν_R^C. The four components of Dirac particle can be written as

$$\nu_D = \nu_L + \nu_R \tag{1.5}$$

and

$$\nu_D^C = \nu_L^C + \nu_R^C \tag{1.6}$$

In Lagrange density derived from the Euler-Lagrange equation is expressed in term of mass of different helicities and simplify hermitian conjugate.

$$\mathcal{L}_D = m^D \bar{\nu}_L \nu_R + h.c = m^D \bar{\nu}_D \nu_D \tag{1.7}$$

The Dirac equation is divided into 2 coupled equations with 2 fields with different handedness where Dirac mass, m_D denotes the coupling strength.

Majorana neutrino introduced different types of coupling for the case of electrically neutral neutrino. If ν_R and ν_R^C are physically indistinguishable, two components theory of neutrino are resolves from Dirac equation. There are 2 Majorana mass term corresponds to the left and right handed field with their CP conjugate.

$$\mathcal{L}_M = \mathcal{L}_M^L + \mathcal{L}_M^R \tag{1.8}$$

where

$$-\mathcal{L}_M^L = \frac{1}{2} m_L^M (\bar{\nu}_L \nu_R^C + \bar{\nu_R^C} \nu_L) \tag{1.9}$$

$$-\mathcal{L}_M^R = \frac{1}{2} m_R^M (\bar{\nu}_R \nu_L^C + \bar{\nu_L^C} \nu_R) \tag{1.10}$$

All ν_L and ν_R^C with their conjugate ν_R and ν_L^C are combined into Majorana mass eigenstates ν_1 and ν_2 which are their own antiparticle. The Lagrange density can be rewrite in terms of ν_1 and ν_2

$$-\mathcal{L}_M^L = \frac{1}{2} m_L^M (\bar{\nu}_1 \nu_1) \tag{1.11}$$

and vice versa.

Majorana case can be distinguished from Dirac case when:
a) the mass term m=0 causes either 2 or four degrees of freedom are detectable.
b) for massive neutrino, the magnetic moment are indicates from CPT theorem due to opposite signs of neutrino and antineutrino.

1.1.2 Neutrino Mass Beyond the Standard Model

The standard model of particle physics assumes that neutrinos are massless. In order for neutrino oscillations to occur, some neutrinos must have masses. Therefore, the standard model of particle physics must be revised. There are two possible types of neutrino oscillation experiments. Firstly, a pure beam of known flavour ν_x are used, and the number of disappeared neutrinos are observed . This is a "disappearance" experiment and measured the survival probability:

$$P(\nu_x \rightarrow \nu_x) = 1 - sin^2(2\theta) \times 1.27 sin^2 \Delta m^2 \frac{L}{E} \tag{1.12}$$

where Δm^2 is the squared mass difference and L/E is the control parameter for the distance between source and the detector and the energy of neutrino. The second type of experiment is an "appearance" experiment, which starts with a pure beam of known flavour ν_x and to see how many neutrinos of a different flavour ν_y are detected. The values of the different neutrino masses may be clues that lead to understanding physics beyond the standard model of particle physics. Assuming there are 2 flavours involve, there will be 2 mass states. This parameter is the difference in squared masses of each of these states:

$$\Delta m^2 = m_1^2 - m_2^2. \tag{1.13}$$

For the neutrino oscillation to occur, at least one of the mass states must be non-zero. This simple statement gives huge implications that the neutrino must have mass. Furthermore the masses of the mass states must be different, else $\Delta m^2 = 0$ and P$(\nu_x \rightarrow \nu_y) = 0$. We can see that the masses control the relative phase of the two mass wave functions.

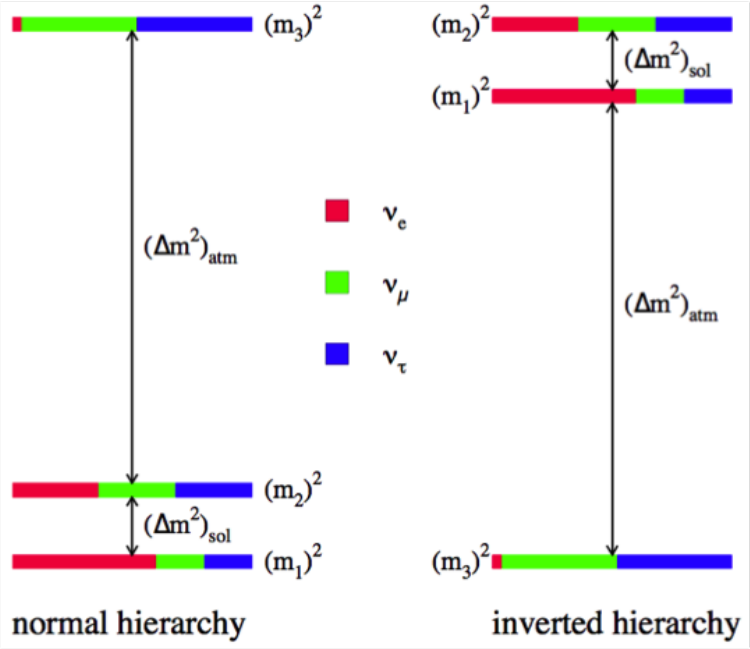

Figure 1.1: Neutrino mass hierarchy[12]

There are limitation of neutrino oscillation experiments, they can give us detailed information on the squared mass difference values, but cannot tell us what the absolute mass of the corresponding states. Neither can they tell us whether m_1 is larger in mass than m_2. If $\Delta m^2 \rightarrow -\Delta m^2$ the probability will still be the same. The relations between the mass description and the associated-particle description involved certain constants, called "mixing angles", whose values are potentially important clues that may help lead to an improved theory of how elementary particles behave [8].

The magnitude of the mass-squared splitting between states ν_1 and ν_2 is known from the KamLAND reactor experiment, and the much larger mass splitting between the third, ν_3 state and the ν_1 - ν_2 pair is known from atmospheric and long-baseline experiments. However, pure neutrino oscillations are sensitive only to the magnitude of the mass splitting, not the sign. Defining the ν_1 state as having the largest admixture of the electron flavor eigenstate, the sign of the mass splitting between states ν_2 and ν_1 is determined to be positive (Δm^2_{21} >0) using the pattern of neutrino oscillations through the varying-density solar medium. However, the corresponding sign of $\Delta m^2_{32} \approx \Delta m^2_{31}$ remains unknown. There are two potential orderings for the neutrino mass the "normal hierarchy", which showed ν_3 is the heaviest, and the "inverted hierarchy", which showed ν_3 is the lightest. This is illustrated in figure 1.1.

1.2 Neutrinoless Double Beta Decay

The doubt of neutrino masses and mixing is one of the most important issues of modern particle physics. One of the method to study the fundamental properties of neutrino is by double beta decay, a rare nuclear process observable in even-even nuclei. The ordinary beta decay is energetically forbidden or highly suppressed by large spin differences. An initial nucleus X(Z, A) decays to X"(Z+2, A), emitting two electrons in the process. The level diagram shows in figure 1.2 of nucleus X'(Z+1, A) is higher than that of the initial nucleus, and it is forbidden to decay.

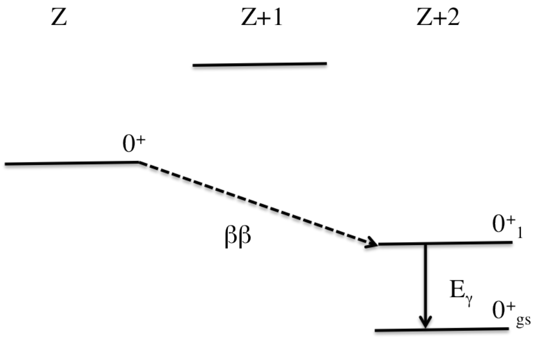

FIGURE 1.2: Level diagram for double beta decay reaction

About a year after Fermi introduced the idea of weak interaction theory, Maria Goeppert-Mayer published an article about double beta decay, $\beta\beta$. In the publication, she derived $2\nu\beta\beta$ transition rate and the half-life of the decay are estimated, assuming that the Q-value is 10MeV.

$$^A_ZX \rightarrow ^A_{Z+2}X" + e^- + e^- + \bar{\nu}_e + \bar{\nu}_e \tag{1.14}$$

Fireman reported the first observation of $\beta\beta$ decay of ^{124}Sn in laboratory experiment in 1949, however he disclaimed it later. So far, 35 nuclei has been recorded as candidate of $\beta\beta$ decay but most popular nuclei used by major DBD experiments are ^{48}Ca, ^{76}Ge, ^{82}Se, ^{96}Zr, ^{100}Mo, ^{116}Cd, ^{130}Te, ^{128}Te, ^{150}Nd, ^{136}Xe and ^{238}U. The process of $\beta\beta$ decay is experimentally demonstrated over a period of more than 20 years.

In 1937, Ettore Majorana formulated a new theory about neutrino where the neutrino and antineutrino are indistinguishable. The antineutrino induced by β^- decay are suggested for experimental verification.

$$\nu +^{A'}_{Z'} X \rightarrow^{A'}_{Z'+1} X' + e^- \tag{1.15}$$

Here we will describe briefly the theory of $\beta\beta$ decay referring to the explanation and elaboration by [6] and [4]. The schematic diagram of two neutrino double beta decay and neutrino less double beta decay is shown in figure 1.3 which illustrated the difference mechanism occured during the decay process where A: $2\nu\beta\beta$. B: $0\nu\beta\beta$ with single Majoron emission. C: $0\nu\beta\beta$ with Majorana neutrino exchange. D:$0\nu\beta\beta$ with SUSY particle exchange.

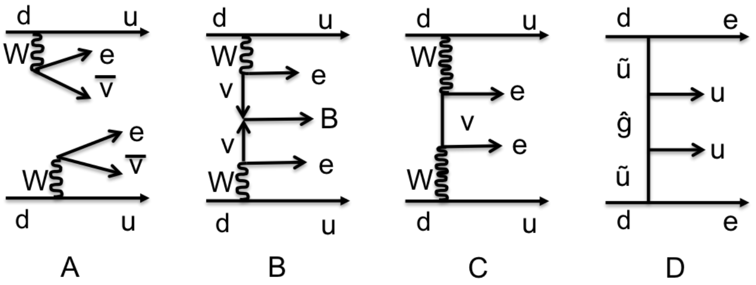

FIGURE 1.3: Schematic diagram of two neutrino and neutrino less double beta decay experiment [3][21]

In later description, T represents the transition rate(probability), M$^{0\nu}$ is the nuclear matrix element, G$^{0\nu}$ is the kinematical factor including the phase space volume and double weak coupling constant. The transition rate for $\beta\beta$ decay is simply expressed in terms of M$^{2\nu}$ and G$^{2\nu}$. The $2\nu\beta\beta$ is a four body process with fixed total energy of Q$_{\beta\beta}$. The rate of $2\nu\beta\beta$ increased rapidly with the increment of Q$_{\beta\beta}$ since the Coulomb effect favours $\beta^-\beta^-$ rates at higher Z nuclei(most of double beta decay candidates are medium or heavy nucleus).

$$T^{2\nu} = G^{2\nu}|M^{2\nu}|^2 \tag{1.16}$$

The transitions in $2\nu\beta\beta$ are mainly Gamow Teller (GT) type since beta rays are mostly low-energy s-wave electrons. The important coupling constant $(g_A G_F cos\theta_C)^4$ given by axial parameter, g_A, Fermi coupling constant, G$_F$ and θ_C as the Cabibbo angle. From the allowed GT($\tau\sigma\tau\sigma$) and Fermi ($\tau\tau$) matrix element, the nuclear matrix element, M$^{2\nu}$ can be deduced.

In the case of light Majorana neutrino emission, one neutron is reabsorbed by the other neutron of the same nucleus. This process requires coexistence of left and right hand helicity which is relevant with weak Hamiltonian symmetric model. the $j_{L\mu}$ and $J_{L\mu}$ indicated the left-handed lepton and hadron current and the subscripts of R indicate the term for right handed.

$$H = G_F cos(\theta_C)(2)^{-1/2}[j_{L\mu}J^{+}_{L\mu} + \chi j_{L\mu}J^{+}_{R\mu} + \eta j_{R\mu}J^{+}_{L\mu} + \lambda j_{R\mu}J^{+}_{R\mu}] + h.c. \tag{1.17}$$

The first term is the neutrino mass term and the following terms associate with the right handed weak interaction where interaction coefficients (χ, η, λ) are given by the θ_{LR} between left and right W bosons (W_L and W_R) and their respective masses term.

$$\chi = \eta \approx -tan\theta_{LR}, \lambda \approx (\frac{M_L}{M_R})^2 \tag{1.18}$$

The left and right handed eigenstate neutrino ν is expressed in mass eigenstate, ν^m are

$$\nu_L = U\nu^m_L, \nu_R = V\nu^m_R \tag{1.19}$$

In different case, the neutrino less double beta decay transition deduced from $T^{0\nu}$=$\frac{ln2}{T^{0\nu}_{1/2}}$ is expressed with particular M$^{0\nu}$ which is the nuclear matrix element, while G$^{0\nu}$ is the kinematical factor for the decay. The current G$^{0\nu}$ is smaller by a factor of ln 2 than the kinematic factors for the inverse half-life.

$$T^{0\nu} = G^{0\nu}|M^{0\nu}|^2 K_{\nu R} \tag{1.20}$$

where $K_{\nu R}$ stands for the neutrino mass and right handed current term which deduce the neutrino mass effective terms. They are expressed as

$$\begin{aligned} K_{\nu R} = [(\frac{< m_\nu >}{m_e})^2 + C_{\lambda\lambda} < \lambda >^2 + C_{\eta\eta} < \eta >^2 + C_{m\lambda}\frac{< m_\nu >}{m_e} < \lambda > cos\psi_1 \\ + C_{m\eta}\frac{< m_\nu >}{m_e} < \eta > cos\psi_2 + C_{\eta\lambda} < \lambda >< \eta > cos(\psi_1 - \psi_2)] \end{aligned} \tag{1.21}$$

$$< m_\nu >= |\Sigma m_j U^2_{ej}| \tag{1.22}$$

$$< \lambda >= \lambda|\Sigma U_{ej}V_{ej}| \tag{1.23}$$

$$< \eta >= \eta|\Sigma U_{ej}V_{ej}| \tag{1.24}$$

In the study of $0\nu\beta\beta$, the effective mass terms are expressed in terms of the neutrino mixing coefficients and the absolute mass of the eigenstates. The neutrino oscillation data provides the mass-square differences and the mixing coefficients. The neutrino flavour eigenstates and the mass eigenstates is connected by the mixing matrices U and V. In light Majorana-ν mass left handed weak current term explicitly expressed by Majorana phase matrix U$_p$ as U = $U_m U_p$. Finally the $0\nu\beta\beta$ rate simply written as $T^{0\nu} = G^{0\nu}|M^{2\nu}|^2| < m_\nu > |^2$ and the effective mass term is $< m_\nu >= |\Sigma|U_{ei}|^2 m_i e^{i\alpha_i}|$.

1.3 Neutrino Nuclear Responses

There are several ways to determine the NME, either experimentally tested by direct kinematical approach through nuclear beta decay and double beta decay experiments or theoretical approach by the evaluation from various calculation models. The neutrino nuclear response is equal to the square of NME but we can not deduce the phase of NME due to the square value. The effective mass of neutrino is extracted from the transition rate of double beta decay experiment. The NME has contribution from the axial coupling constant, g_A and nuclear spin-isospin correlation parameter, g_V and theoretical model dependent. The uncertainty of NME is quite large due to these not well known parameters.

The early study of double beta decay structure calculations are mostly focused by using the nuclear shell model as a commencement point. Shell model has some limitation to only single particle motion in bound orbitals in response to the remainder of the system. In theoretical description of double beta decay process proceed through intermediate double-odd nucleus virtual states [9] [4]. The extreme single particle model works well near the vicinity of closed shell, but requires more approximations as we move to several nucleons away from the major closed shell. Pauli Exclusion Principle provides a little philosophical support for proceeding with development of such a model.

The entrance of the different energies on the nucleons of different angular momentum states. Hence causes the nucleus to move in a harmonious fashion, to avoid suffering from frequent collisions. However, it still remains in the discrete orbitals for the validity of the model [10] [11]. The saturation of nuclear forces resulting in an approximate constant binding energy for each constituent nucleon, independent of the details of nuclear structure. This is attributed to the fact that the size of the nucleus is basically proportional to the number of nucleons and hence the nucleus seems to be a rather compact object with nucleons basically touching each other.

Due to the fact that double beta decay nuclei are mostly medium-heavy nuclei or heavy nuclei, a more suitable Quasiparticle Random Phase Approximation (QRPA) have been introduced [12]. Compare to the nuclear shell model, QRPA and pn-QRPA are malleable in heavy nuclei. An adjustable parameter for the proton-neutron interaction, g_{pp} is introduced. The half-life of double beta decay are sometimes strongly depends on the strength parameter g_{pp}. Experiments such as muon capture observables [9] and renormalizing pn-QRPA [13] are some suggested experiments in order to fix g_{pp} parameter.

The $2\nu\beta\beta$ decay ensues from the grandfather nucleus to the daughter nucleus through the 1^+ states of the intermediate nucleus. The corresponding half-life of this decay is factorised by

$$T^{2\nu}_{1/2}(T_i^+ \rightarrow T_f^+) = [G^{2\nu}|M^{2\nu}|^2]^{-1} \tag{1.25}$$

It has been emphasised by previous report of Kortelainen [10], that the Ordinary Muon Capture (OMC) probes for double beta decay only involved one of the two branches $\beta\beta$ decay in a 2 stepped process. From his observation, the total and partial capture rates give enough information about the nuclear structure of intermediate nuclei of any $\beta\beta$ decay candidates. The similar information is also concluded then by log ft value.

Until the 20^{th} centuries, the direct determination covers all nuclear β decays resulting $\bar{\nu}_e$ from β^- decay and ν_e from β^+ decay or EC. These reaction is closely related to the neutrino capture reactions. The Q-value indicates the mass differences between mother and daughter nucleus, where Q-value $\nleq 0$. The β^+ decay and EC leads to the daughter nucleus with same Z.

β^+ decay:

$$Q_{\beta+} = [m(Z,A) - m(Z-1,A) - 2m_e]c^2 \tag{1.26}$$

Electron Capture:

$$Q_{\beta+} = [m(Z,A) - m(Z-1,A)]c^2 \tag{1.27}$$

The probing by electron capture and beta decay only gives the information of the lowest J^π state of the odd-odd nuclei. By muon capture reaction which is relatively known having a higher momentum transfer due to it's mass is 203 times heavier than the electron might probe higher J^π state of the intermediate nuclei. This gives more accurate information to the nuclear structure study of double beta decay.

Nuclear responses for $\beta\beta$ decay are important for neutrino studies in nuclei. The nuclear response are very sensitive to spin isospin interactions and spin isospin correlations. Nuclear matrix element for $2\nu\beta\beta$ decay, $|M^{2\nu}|^2$ have been obtained by half life measurement. The current $|M^{2\nu}|^2$ are only in the order of 10^{-1} to 10^{-2} in units of $(m_e)^{-1}$. The observed $2\nu\beta\beta$ matrix element are suppressed due to possible double GT transition at high excitation region but the value is not so much scattered. In 2002, Ejiri [5] suggested to include the nuclear medium effect on $2\nu\beta\beta$ response and also the future response of $0\nu\beta\beta$. Since the single response is the square of the matrix element, the expected range of single response is only in order of 10^{-2} to 10^{-3}.

1.3.1 Experimental Probes for the Nuclear Responses Studies

The determinations of the nuclear matrix element have been widely studied and in the last few years the reliability of the calculations has considerably improved [4]. Nuclear matrix element is directly proportional to the double beta decay transition rate and can be given by the sum of products of single β^- and β^+ nuclear responses [14] [7]. The $\beta\beta$ decay experiment was developed to study the fundamental properties of neutrino either Dirac or Majorana particle by measuring the double beta decay reaction rates and the upper limits of the neutrino effective mass. The isotopic $\beta\beta$ decay candidates were observed experimentally by calorimetric or spectroscopic method.

However, many newly developed experiments, which study the single beta response by using weak, electromagnetic and strong interaction to accurately describe first and second beta decay involved in the reaction and also studying the intermediate nuclear structure. In comparison to the nuclear matrix element for $2\nu\beta\beta$ and $0\nu\beta\beta$ direct observation, single neutrino responses are more sensitive to the nuclear structures, $\tau\sigma$ correlation, proton-proton correlation, effective axial parameters and others. The value of current limit of nuclear matrix element from the giant resonance (GR) excitation which are mostly from Gamow Teller transitions are extremely small after renormalisation of g_A and other short range correlation [4] [14].

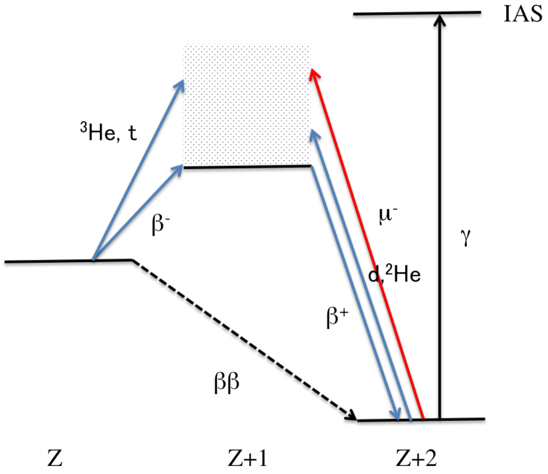

FIGURE 1.4: Double beta and single beta response probe[24]

Figure 1.4 shows the response from single and double beta decay experiments [15]. Double beta decay provide overall response from grandfather nucleus denotes as A to the daughter nucleus (B). While the single response such as nuclear β^- decay and charged exchange reaction by nuclear probe provides the β^- responses from nuclei A to C. Photo-absorption study by photon probes excites the nucleus until Isobaric Analog States(IAS) and gives nuclear structure of particular nuclear. Lastly, the weak probe and β^+ decay provides β^+ response of B and C nuclei.

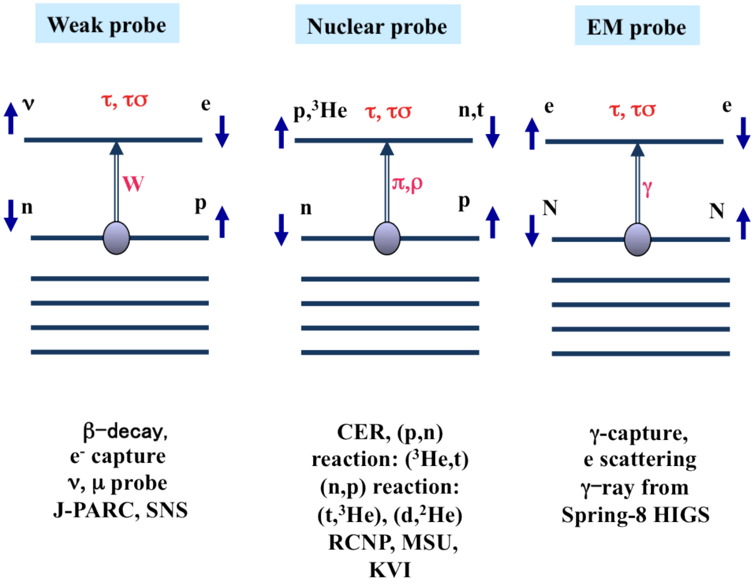

FIGURE 1.5: Nuclear response probe[2][21]

Nuclear and photon probes provides indirect approach towards the study of neutrino response. On the other hand, weak probe can comprehend the direct neutrino response. The nuclear probe gives high sensitivity measurement which accurately shows the 1^+ states of the excitation region it is a complimentary method to the weak probe. This method have been study at IUCF, KVI, RCNP and others to get the vector weak responses and axial-vector weak responses. The charge exchange reaction often studied by (p,n), (n,p), (d,^{2}He), (^{3}He,t), (t,^{3}He) and (^{7}Li,^{7}Be) reaction. The cross section of charge exchange reaction is mainly due to large central isospin and spin-isospin interaction ($V_{\tau\sigma}$) and small distortion interaction (V_0) at medium energy.

Photo-nuclear reaction by electromagnetic probe through isobaric analog states (IASs) of target nuclei was recently study by many researchers. For a medium heavy nuclei, IAS was located on the E1 giant resonance (GR) in the range of high excitation region. Photo nuclear reaction includes isobaric analog resonance(IAR), GR and their interference term shown in equation below. The relative phase ϕ at IAR can be synthesised for matrix element determination. High energy electron are scattered from the laser photons are used during the photo nuclear reaction. The polarisation of the photon can be used to study E1 and M1 matrix element separately. New SUBARU and other electron synchrotrons is used to provide high intense laser electron photons for the photo-nuclear reaction.

The weak probe provides excitation region including 1^+, 1^-, 2^- and higher states by muon capture or neutrino interaction. We can hardly distinguish between these excitation region, however the higher 1^- and 2^- states can gives more information about the intermediate nuclei nuclear structure. In this study, we will demonstrate how lepton or weak probe is a very useful technique to determine the nuclear matrix element. It is best to study the weak interaction by neutrino itself, however due to unknown properties and characteristics of neutrino interaction give experimentalist the hard work. Investigation of nuclear weak interaction can also be done by lepton [4] [16]. It has been pointed in 1972 [14] and 2001 [17] that muon capture reactions are reliable to get the information on the β^+ side of DBD. RCNP, J-PARC and SNS are reliable facilities to provide high intense muon and neutrino beam for this reaction.

1.3.2 β^+ Nuclear Responses Studies

Instead of muon capture reaction, the (n,p) reaction such as (d,^{2}He) and (t,^{3}He) have also been used to study the β^+ responses for $\beta\beta$ decay. These reaction using deuteron and unstable triton beam provides information on the low lying states of nuclear structure especially the 0^+ and 1^+ states on particular nuclei. Due to the deuteron beam facility at KVI have been currently shut down, data on $\beta\beta$ decay nuclei can not be obtained.

Also previous work by muon capture reaction are focusing on light and medium nuclei which are not the candidate of $\beta\beta$ decay. Most of them are focusing on the comparison with zero neutron emission which in particular have the same outcome with (d,^{2}He) and (t,^{3}He) reaction. This type of reaction provides complicated structure resulting from the momentum transfer of muon capture which is high enough to excite high excited level.

In this present work, the results from muon capture reaction of ^{100}Mo will be presented. ^{100}Mo is the candidate for $\beta\beta$ decay which are used widely by several experiments such as Elegant, Osaka and NEMO III, but we should expect the β^+ response from ^{100}Ru nuclei. Due to it's typical mass number, we will study the β^+ response from ^{100}Mo. The whole excitation region by muon capture up to 50MeV which covers spin of 1^+, 2^- and so on will be discussed corresponds to the analysis of delayed RI gamma rays, which are very simple and clean.

1.4 Outline of This Thesis

The aim of this reports is to provide a new method of studying the NME for DBD by nuclear muon capture. In order to obtained these information, a new experimental techniques by nuclear muon capture is developed. The experimental data was evaluated by the first neutron statistical model for muon capture reaction. The relative muon capture strength will be deduced from the comparison of the statistical model and experimental results on ^{100}Mo.

This research report will be organise as follows, chapter 1 briefly explains the status of neutrino physics, experimental probes of neutrino responses and previous work on β^+ side of NME. The mechanism of muon capture, features of nuclear muon capture and its response for DBD NME estimation will be described in chapter 2. Chapter 3 will includes the detailed explanation of the development and performance of neutron statistical model. Further explanation on the methodology of the experiment and analysis will be emphasized in Chapter 4 and Chapter 5. Chapter 6 will showed the comparisons with suggested statistical model. The discussion regarding the problem faced during experiment and the analysis results and the concluding remarks are summarised in Chapter 7.

Chapter 2

Muon Probe Responses

In order to understand the muon capture reaction, we need to know the formation of muonic atom after the target was excited by muon. Muon is a charged lepton which is 200 times heavier than electron. Positive muons behave like a light proton, while the negative muons behave like a heavy electron. Since muon is unstable due to its short mean lifetimes, it does not exist in nature. However, it can be produced through a nuclear reaction in a reactor. Many muon facilities in the world such as MuSIC-RCNP, MLF-JPARC and SμS-PSI provides high intensity muon beam. Muon physics have become the major part towards the extension of physics beyond SM. Ever since its discovery in 1937, many existing reviews proposed by the theorist in different angles but much information which is relevant to an experiment is omitted from such an approach.

The study of particle emitted after muon capture provides additional point of view by obtaining the information on the nuclear structure and becoming an excellent test in understanding the complex nuclei. Indeed the observation of muonic X-ray as the formation of muonic atom after muon capture have been widely use in quantitative analysis on bulk samples since its discoveries [18] [19]. Starting from 1950s the muon capture reaction have been study by various methods, focusing on the capture rate in low Z materials such as ^{16}O, ^{12}C and ^{13}B [20] [21] [22].

Muon activation analysis is used to study the outcome after muon capture reaction by deducing the isotope-mass population from the observation of gamma rays during the experiment. The gamma rays are identified from their observation by beta decay half life. This chapter will explain in the details the interaction of muons, muon activation analysis technique, the feasibility test at MuSIC, RCNP and the overview of this research study to provide NME for DBD.

2.1 Muon Capture Reaction

Muon capture can occurs in any nucleus due to its large capture probability except for light nuclei with Z$\leq$10. The high excitation energy due to high momentum transfer excites the nuclei up to 100MeV. In order to identify the emitting muon neutrino following the reaction, the excited energy level has to be measured are summarised by [14]. When muon reaches to 1s orbital of a muonic atom, it can either decay or captures by the bound proton. In light nuclei, capture process is far more likely than decay due to the Bohr radius is larger than the nuclear radius [19].

$$\mu^- +^A_Z X \rightarrow Y + \nu_\mu \tag{2.1}$$

The Y residual product consists of either heavy nucleus or light particles or both. The daughter nucleus produce after muon capture might be in its ground state(g.s) or in one of its excited states. Most radiative muon capture in intermediate and heavy nuclei, light particles such as neutrons and (or) γ-rays directly emitted and only a few percent of charged light particles(p, d, ^4_2He) are observed. The energy releases when muon capture occurs is mainly donated to neutrino, but the residual nuclei absorbed considerable amount of energy which contribute to many following reactions. Most experiments concentrate on the small fraction of reactions that leaves the final nucleus in a bound state. The bound state transitions can be observed via γ-rays emission. However these transitions are hidden in the overwhelming background.

Most muon capture in a spin zero target nucleus [23] gives scalar, pseudo scalar or pseudo vector observables and non-spin zero target extended research determines the pseudo scalar coupling constant from the muon capture rates and recoil nucleus orientations. Scalar observable refers to the total and partial capture rates that are very sensitives to nuclear wave functions. Whereas the pseudo scalar or pseudo vector observables accompanies by the muon capture products such as recoil nucleus, neutron and neutrino. The parity violation stimulates by a lot of activity in search of these observables in various weak interaction processes. The asymmetry, polarization, orientation and angular correlation of pseudo scalar and pseudo vector observables are insensitive to the nuclear structures. Hence can be used for determining the coupling constants of muon capture interaction [23].

The observation of pseudo scalar coupling constant of the nucleon weak current, g_p from muon capture on hydrogen has become the pin point to study two processes, ordinary muon capture(OMC) and radiative muon capture (RMC). The RMC is followed by the gamma emission together with emission of neutron, muon neutrino or light particles [11] [24].

2.1.1 Formation Of Muonic Atom

It is wise to perform a muon capture experiments by using target with pure composition or enriched isotopic targets. Even though using target with impurities is more convenient, but it is not easy to estimate the relative number of capture in mixed targets. Experimental studies using various compound such as oxide, fluorides and chlorides to a lesser extent and few other compounds to study the capture ratios have been measured. Any generalisations must be viewed due to the limited database.

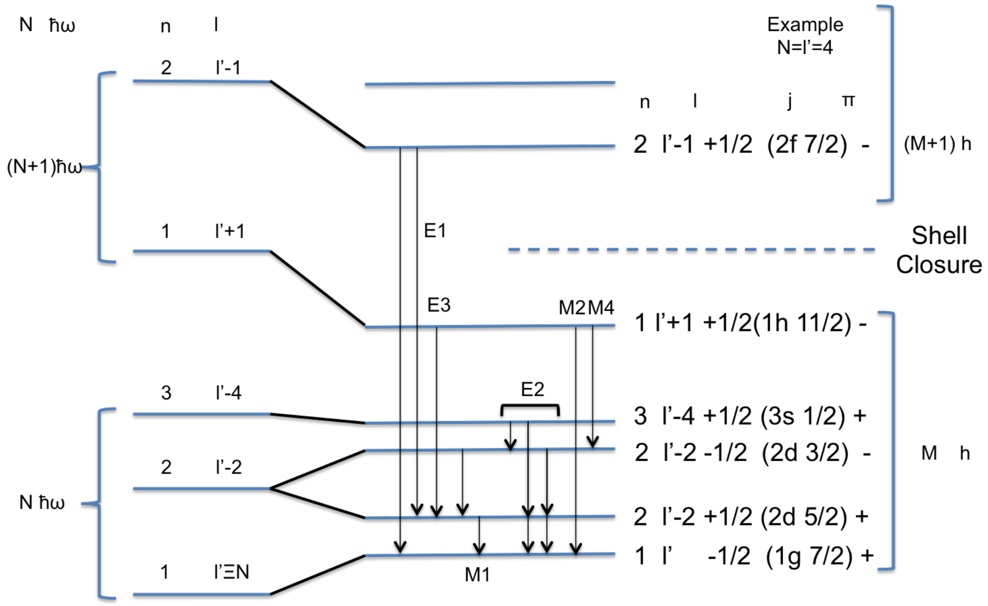

FIGURE 2.1: Gamma branching and magnetic (M1, M2, M3, M4) and electric quadrupole (E1, E2, E3) interactions was shown at each corresponding gamma energy[44].

When a negative muon is captured or stopped in a target material, it quickly became attached to the K-orbital of an atom. The energy released during the capture reaction is transferred to Auger electrons which simply emitted from the atom along with the muonic characteristic X-ray emissions. The muonic X-rays energies are higher than these of regular electronic X-rays due to the large mass of a negative muon. Such muonic X-rays carrying energy in the range of 0.1MeV to 6 MeV are emitted from bulk samples without photon self-absorption. The muonic X-ray has a specific energy to the atomic energy level of the muon described by the Bohr approximation formula below.

$$E_n = \frac{mq^4Z^2}{8\epsilon_0^2h^2c^2n^2} \tag{2.2}$$

where m is mass of muon, q is the charge, Z is the atomic number of the target material, n is the principal quantum number and ϵ_0, h and c are the permittivity, Planck's and speed of light constants respectively. The source elements of these muonic X-rays are easily identified using a semiconductor detector.

In muonic atoms, the transitions of X-ray strongly affected by the size of nuclei and depending on the accuracy of present Ge detectors. Transitions of $2p_{3/2}$ to $2p_{1/2}$ or $2p_{1/2}$ to $2s_{1/2}$ up to 4f-3d levels can be used to study the charge distributions as shown in references [18] and [25].

The depth of muon implantation in sample can be tuned by adjusting the incident muon momentum. In addition, the samples are hardly activated by muon irradiations. These are very important advantages for elemental analysis compared with other methods like X-ray fluorescence and prompt gamma-ray by neutron irradiation. The applications of muonic X-ray spectroscopy to the non-destructive elemental analysis are expected [18].

The levels in muonic atom diverge by the magnetic M1 and electric quadrupole E2 interactions between the muon and the nucleus. Compare to electronic case, the quadrupole splitting in muonic atom is bigger by 100-200keV than the magnetic splitting due to proportionality of quadrupole interaction and M1 interaction towards the mass of muons. In addition, the static quadrupole interaction like some E1 interaction in light nuclei and dynamic E2 interaction in medium heavy nuclei located at high excitation energy region which leads to resonant excitation of the nuclear rotational states [21].

2.1.2 Muon Decay and Cascade Process

Upon spending part of its time when captures into an atomic K-shell, there is a large probability that muon is captured by a proton via weak interaction process in a medium or heavy nuclei. In these process, some of the muons decays to electron and emit neutrino. It is reported that the fraction of decay is lower as the nuclei becomes heavier.

The neutrino takes of most of the energy leaving 10-15% for the neutron recoils process following the reaction. The nucleus and neutron might have an energy distribution, E(Q) which depends on the momentum distribution of the capturing proton. The probability of proton emission is small compared to the neutron emission due to effect of Coulomb barrier at these medium excitations and the gamma is emitted when the excitation does not exceed the threshold for particle emission.

Neutron emissions predominates the reaction and the numbers of neutrons yields information of the population of low-lying states following the μ meson, nuclear-excitation distributions and proton-momentum distribution. The details of nuclear excitations that can be conjectured from the neutron multiplicity measurements and deduced the muon capture rate calculations which are sensitive to the excitation function. The high efficiency measurement of the neutron multiplicities distribution have been done using silver and lead target with cadmium loaded liquid scintillator neutron detector from interaction with cosmic ray muons. Later, muon produced by cyclotron with high purity beam are used on 8 targets ranging from aluminium to lead.

The theoretical part in solving the demanding problem of muon capture process is first performed by Fuji and Primakoff. A single particle j-j coupling shell model from Primakoff theory of muon capture based on an effective Hamiltonian, H_{eff} have been used. Later in 1970s, a similar theory with the extend of allowed and forbidden beta decay transitions was formulated by Fujii and Morita by studying the muon-nucleon interaction. Two types of approach are introduced to study the muon capture which are impulse approximation (IA) and elementary particle approximation (EPA) discussed in [26].

Nuclear reactions induced by hadron projectiles are principally governed by the strong interaction. The electromagnetic interaction is involved in various stages of the nuclear reaction. The nuclear reaction is a fast dynamic process where the time scale is in order of 10^{-22} to 10^{-20} s for direct and pre-equilibrium reactions. The time scale extends to around 10^{-18} s for equilibrium reactions. This time scale is still much shorter than the time scale of γ transitions of around 10^{-15} to 10^{-9} s.

Gamma-ray spectroscopy is mostly concerned with effectively bound states produced after all the prompt nuclear reaction processes which is induced by the strong interaction. Gamma ray spectroscopy yields decisive and detailed information on the residual bound states such as: Identification of reaction products (mass and charge), excitation energy, linear and angular momenta, parities and others [12].

Gamma transitions are partially converted to internal conversion electrons leaving holes in inner electron shells, and the hole is filled by emission of an X-ray characteristic of the atomic number Z. The X-ray may be used to identify the atomic number Z of the residual nucleus. If the reaction feeds the ground state of a β unstable nucleus, β-γ spectroscopy may also be used to identify the residual nucleus.

The studies of the γ rays following the A(a,xy...)B*(γ)B unleash the properties of the residual nucleus B^* such as mass, charge, excitation energy, angular momentum and its direction, linear momentum and so on. Nuclear gamma ray transitions between nuclear excited state are characterised by electric or magnetic transitions. It provides powerful tools for investigating single particle motion with support by simple selection rule. Electric quadrupole(E2) and magnetic dipole (M1) moments frequently observed in low lying state by previous in beam studies.

2.1.2.1 Neutron Emission

Nuclear de-excitation is assumed to occur by neutron boil-off and probability of neutrons by nucleus with a distribution of excitation, E$_i^{ex}$(Q) is defined by following relation.

$$P(E_i^n) = \int_{B_i^n}^{E_0^{ex}} N_i^n E_i^{ex}(Q)dQ - \int_{B_i^{n+1}}^{E_0^{ex}} N_i^{n+1} E_i^{ex}(Q)dQ \tag{2.3}$$

where B_i^n is the binding energy, N_i^n is the constant derivative of neutron emission by the variation of nuclear temperature of compound nucleus, T_{EQ}. The nuclear temperature varies over reasonable range of values which gave small effect on the neutron multiplicities. The nuclear temperature, T_{EQ} is the temperature of a compound nucleus produced by muon capture on medium heavy nuclei, which is in the range of 1 to 4 MeV for projectile energy of 20 to 200MeV. The range of nuclear temperature is in agreement with those reported by Evseev et. al. which increases as the mass number increase. The distribution functions for the kinetic energies can be derived by Monte Carlo statistical calculation.

$$T_{EQ} \propto \sqrt{\frac{E_0^{ex}}{a}} \tag{2.4}$$

The integrals are evaluated numerically for the various excitation distributions. In order to compare with experimental values of neutron multiplicities, a neutron statistical calculator is developed and explained in details on Chapter 3.

2.1.3 Muon Activation Analysis

The details of this section is reviewed from [16]. Activation analysis is widely used in variety of analytical problems which require high sensitivity analysis. The production rate R(X') by (μ,xnγ) reaction is expressed as

$$R(X') = N(X) \times R(\mu X) \times Br(X') \times N_\mu \times \eta_s \tag{2.5}$$

where X is the sample, Y is the production isotope after capture, N(X) is number of isotope X in sample, R(μX) is the probability of muon capture, Br(Y) is the branching ratio of the isotope Y production, N_μ is muon flux intensity and η_s is the muon stopping probability in the sample.

In the case of isotope X with impurity of isotope S with atomic number Z_X and Z_S respectively. The muon capture probability, η_C is given by $N(X)R(\mu X) + N(S)R(\mu S)$ with number of isotope X and S is N(X) and N(S), while R(μ X) and R(μ S) is the probability of muon capture in isotope X and S. If the atomic number, Z for either isotope X and S is bigger than 10 and the sample thickness is larger than the muon range, most of the muon are captured or stopped into either X or S isotopes and $\eta_C =$ 1.

$$N(X) = I(X) \times N(S) \times \frac{Z_S}{Z_X} \tag{2.6}$$

Assuming N(X) $\ll$ N(S), the number of isotope can be expressed in terms of the impurity, I(X) with Z_X and Z_S are their mass number. Using these relation, one gets reaction rates in term of impurity fraction.

$$R(X') = I(X) \times k_{XS} \times Br(X') \times N_\mu \times \eta_s \tag{2.7}$$

The number of isotope X' produced by muon capture reaction is

$$N(X') = \frac{R(X')}{\lambda} \times [1 - exp(-\lambda t_{irr})]) \tag{2.8}$$

where $\lambda = \frac{ln2}{t_{1/2}}$ is a decay constant, t_{irr} is irradiation time and $t_{measure}$ is measurement time. The yield of γ rays from RIs of Y for the measurement time is written as

$$Y(X') = N(X') \times \epsilon(\gamma) \times Br(\gamma) \times [1 - exp(-\lambda t_{measure})] \tag{2.9}$$

2.1.4 Reaction Cross Section

In contrast to other muon induced reaction, muon captures in almost all nucleus, the larger atomic number Z the probability of captures increases. Each captures sometimes results in different isomer It is crucial to know the stopping probability and total atoms per target to estimate the reaction cross section involving muon capture reaction.

2.1.5 Beta Strength Distribution

Beta decay clearly follows the first order kinetics and the rate of decay should be unfold by a single decay constant. Beta strength distribution is a constant associates with the interaction between the nucleons, leptons and neutrino which are so called the weak interaction. In comparable to alpha decay range, it have been observed experimentally that the half life beta decay covers a wide range from few milliseconds to $\approx 10^{16}$ years.

The calculation of the decay rate from the structure of parent, ground state and available daughter states require a full quantum mechanical approach due to the creation of at least two particles involve in the decay process. The gamma transitions following muon capture process helps to study giant multipole excitation of higher angular momentum states and nuclear structure of the low lying states. The population of productions isotope estimate the beta strength distribution of the interactions.

2.1.6 Gamma Rays Analysis

The γ rays emitted following the capture reaction provides us the structure information that is essential to understanding nuclei structure. The ability to make precise energy measurements using the high purity germanium detector(HPGe) relies not only on the hardware itself (detector type, Ge crystal size, logic circuit) but also on appropriate data analysis techniques. Details of these techniques are provided in the following subsections.

2.1.6.1 Calibration

In order to obtain energy measurements of γ rays detected by the HPGe detectors, it is necessary to calibrate each data collected as a function of energy. Calibration and gain matching was achieved through the positioning of known γ-ray emitters in the calibration run at the end of the experiment, when no beam was incident on the target. Calibration data were collected using ^{133}Ba source as this isotope have known γ-ray lines in the energy region of interest(see appendix B). A linear function relating channel number to energy for each detector was obtained through analysis of the source data (see section 6.1) [27].

2.1.6.2 Efficiency Correction

The efficiency of HPGe detector varies depending on the energy of the incident γ radiation. The understanding of this energy dependence is necessary to determine the absolute intensities of γ-ray transitions. Information regarding the peak efficiency and total efficiency of the HPGe detectors is necessary for this thesis work. A functional form of the energy dependence is determined through analysis of calibration data taken with ^{133}Ba γ-ray sources. The number of counts in photo-peaks with known relative intensities are established for both sets of calibration data and renormalised to allow a composite analysis (see section 6.2).

2.1.6.3 Nuclear Gamma Cascade Effect

The γ rays decay in a few seconds to few days. The coincidence γ rays are collected simultaneously and required an analysis of which specify the γ-ray transitions by the correction of total efficiency. This correction is obtained from the simulation of gamma ray energy with the total number of emission. The angular correlation function between 2 gammas are determined by the following equation

$$wcos\theta = 1 + a_2 P_2(cos\theta) + a_4 P_4(cos\theta) \tag{2.10}$$

where $P_n(\cos\theta)$ is a Lagendre's polynomial of n^{th} order and a_2 and a_4 are the coefficients. However, angular correlation of 2 gammas are not necessary in this thesis work.

Let's consider 3 γ rays with energies $E_{\gamma 1}$, $E_{\gamma 2}$ and $E_{\gamma 3}$, detected in coincidence with a single gamma peak. Then, the probability of detector detects γ(j=1,2,3) is described by 2 parameters which are ϵ_i^{jp} the probability of gamma rays in photo peak and ϵ_i^{jt} the total probability of gamma detection. Thus the observed count rates in detector 1 in the photo peak 1 is

$$R_1^1 = A\epsilon_1^{1p}(1-\epsilon_1^{2t})(1-\epsilon_1^{3t}) \tag{2.11}$$

where A is the activity of photo peak 1 and $(1-\epsilon_1^{2t})$ and $(1-\epsilon_1^{3t})$ are the probability for $\gamma 2$ and $\gamma 3$ not to be detected by detector 1.

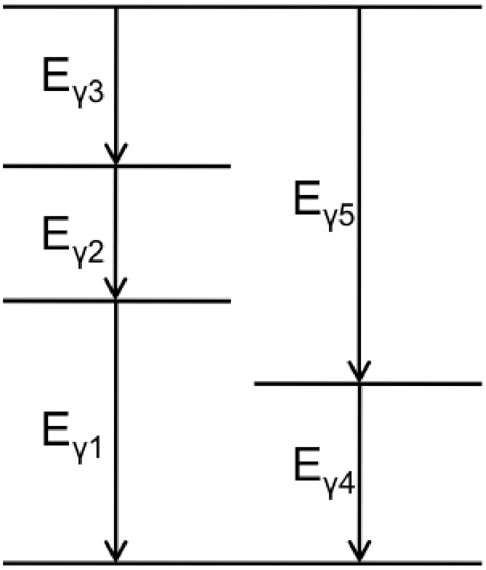

FIGURE 2.2: Example of gamma-decay scheme

The nuclear gamma cascade is strongly dependent to the detector solid angle. In case of very small solid angle, the effect of nuclear cascade is not severe and thus can be assume to be negligible.

2.1.7 Beta Decay Half Life

Each radioactive element, or radionuclide, has a characteristic half-life. The gamma ray is classically produced by the decay from high energy states of atomic nuclei, but are also created through other processes. From the decay curve, the half life of each isotopes is estimated.

$$\frac{dN}{dt} = -\lambda N \tag{2.12}$$

$$N(t) = N_0 e^{-\lambda t} \tag{2.13}$$

where N_0 is number of isotope at time = 0. The negative sign indicates the decreasing N as a function of time. In most beta decay, the daughter nucleus is left in an excited state which immediately decays by emitting one or more γ rays. Some cases occur when there are more than one decay branch from different excited states of daughter nucleus. Each branches have separate end point energy and even decays in different half-life depending on their respective decay probabilities [28].

2.2 Feasibility Test at MuSIC Facility

Four natural molybdenum targets are irradiated with intense muon beam by MuSIC facility for approximately 1hour. Ejiri [16] [29] suggested that by measuring gamma rays following the muon capture reaction, different isotope with nearby isomers of molybdenum target can be observed. The outcome of the observation is the same way as the experiment of measuring neutron emission following capture process. Their difference are the number of production isotopes and the radio isotopes (RIs) production rate is deduced from gamma ray yields. In this feasibility test, we plan to observe delayed gamma rays following the muon capture reaction.

Figure 2.3 shows the gamma rays spectrum of muon capture on natural molybdenum. We can see that the total population observed in MuSIC beam test are around 40% in total from 4 isotopes with mass number 90, 95, 97 and 99. In this test, even though we successfully observed most expected gamma rays except for gamma rays from mass number smaller than A=89. Due the incomplete MuSIC beam line, the contribution from pion capture reaction are unknown.

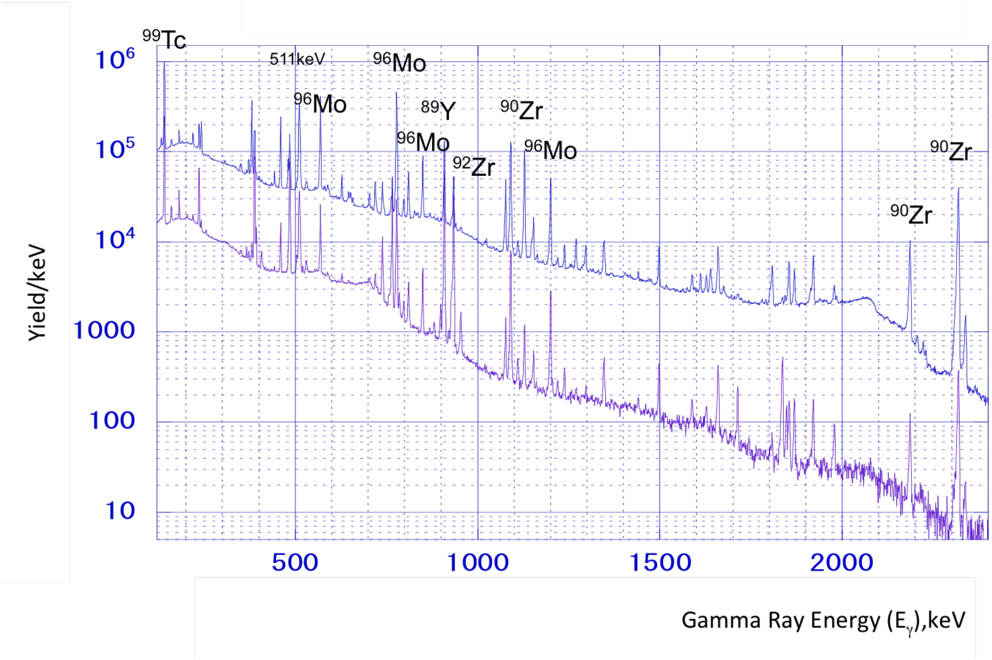

FIGURE 2.3: Gamma rays spectrum from feasibility test at MuSIC facility[7][20].

2.3 Overview of This Method

This new method presented in this thesis consists of experimental part and model calculation part. In experimental part, ^{100}Mo target will be irradiated by muon beam at J-PARC, MLF. The HPGe detector detected the outward gamma rays produce by the muon capture reaction. After 10hours irritation, the target moved to a low background room for delayed gamma rays measurement. The long lived gamma rays with half-life longer than 1hour measured by HPGe detector for 6 days. Finally, the gamma rays analysed by muon activation analysis will deduced the isotope-mass population of the nuclei after muon capture.

On the other hand, 5 models of initial excitation energy, E_0^{ex} are introduced in the model calculation parts. This models simulated the final nuclei observed during the experiments by following the established neutron emission distribution and excitation energy distribution from former neutron statistical model. The outcome of experimental results and the model calculation are compared by the χ^2 fitting and the best models will be determined. In the end, this method will deduce the relative weak strength distribution of the muon capture reaction.

In future, the relative weak strength distribution should be checked with the QRPA theoretical calculation to obtained the g_A value for the muon capture reaction. If this g_A value could reproduce the weak strength distribution, then it should be suitable for the NME calculation. However it does not reproduce this weak strength distribution, then some modification towards the parameters and the model assumptions are necessary.

Chapter 3

Experimental Instruments and Procedures

In the experimental section, two parts of experimental setup and data taking systems are used. The on-beam measurement have more complicated set up and data taking system, while the setup for delayed gamma-rays measurement is much simpler. Incident muons of momentum around 30MeV/c are provided to the thin enriched molybdenum film prepared by depositing of molybdenum powder onto thin mylar films (2.5mg/cm^2 in thickness) specially prepared for double beta decay experiment by Shima's team [30]. Neutron multiplicity distributions for (μ, xnγ) reactions were obtained from γ-ray spectra for the reactions of ^{100}Mo(μ, xnγ)$^{A-x}$Nb/Zr, at $p_\mu = 30$ MeV/c. In this chapter, I will provide details on the beam structure information, experimental setup, shielding and data taking systems.

3.1 Beam Course

The beam profile of D2 beam line will be discussed in the following sections. The proton beam is bombarded on a graphite target which produced pion and decay to muons. Muons are emitted at the end of transport solenoid equipped with high superconducting magnet. A clean muon beam is expected with low neutron and pion background at Material and Life Science Experimental Facility (MLF). At MLF, the proton beam provided by the RCS can generate either single or double-pulsed time structure of 100 ns width, separated by 600 ns with a repetition rate of 25 Hz, and produced the muon beam following the same time structure.

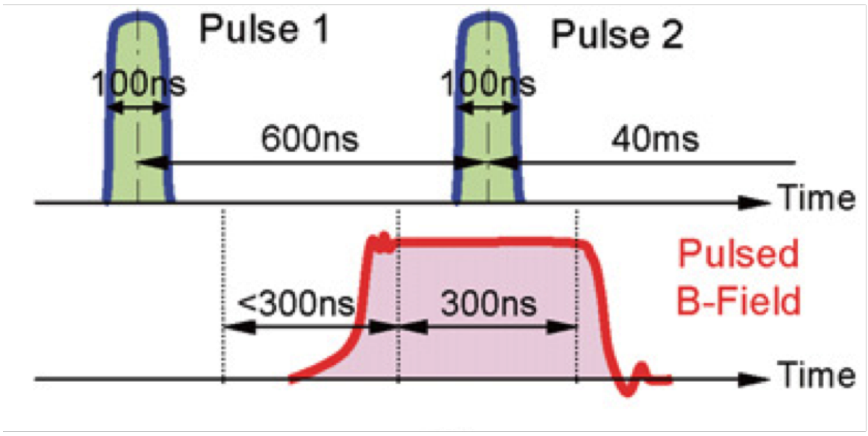

FIGURE 3.1: Double pulse structure of MLF Facility

The MLF have 4 muon secondary lines with different beam energy located in experimental hall 1 and 2. D-line have for 2 experimental areas to provide decay muon of energy up to 50MeV, it had been operating since 2009. The U-line for ultra slow muon beam is in its constructing stage and expected to have highest energy resolution with shortest muon pulse width. In future, the S-line which occupied by 4 experimental area exclusively for material science study by surface muon beam and the H-line for high momentum muon beam will be constructed.

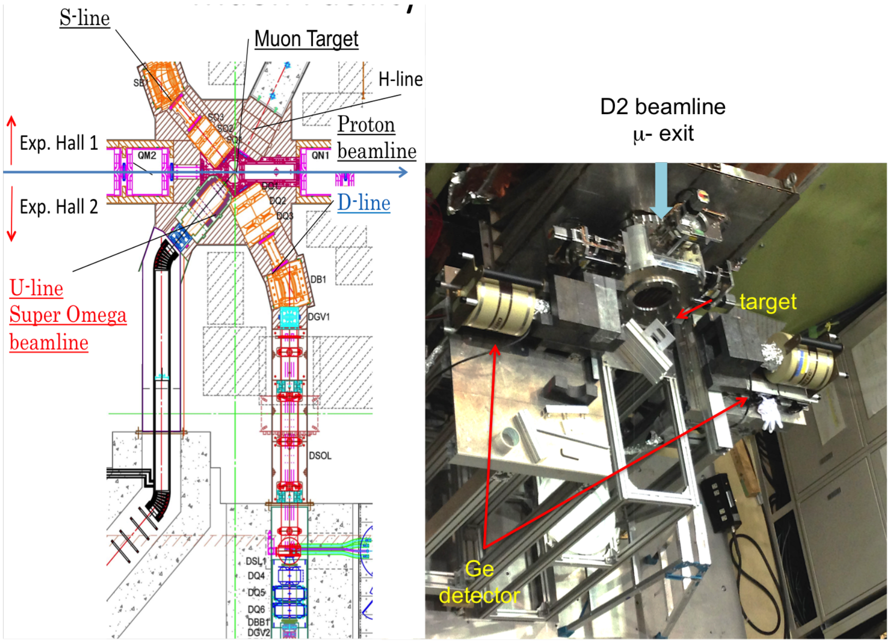

FIGURE 3.2: (a)Muon section at MLF-JPARC (b)D2 beam line at MLF-JPARC

A 300kW proton beam interact with the graphite target to produce muons from pions decay. Positive or negative muons can be produced with momentum as high as 50MeV/c to penetrate the target of a few micron thickness. The negative muon intensity at 220kW is shown by figure 3.3.

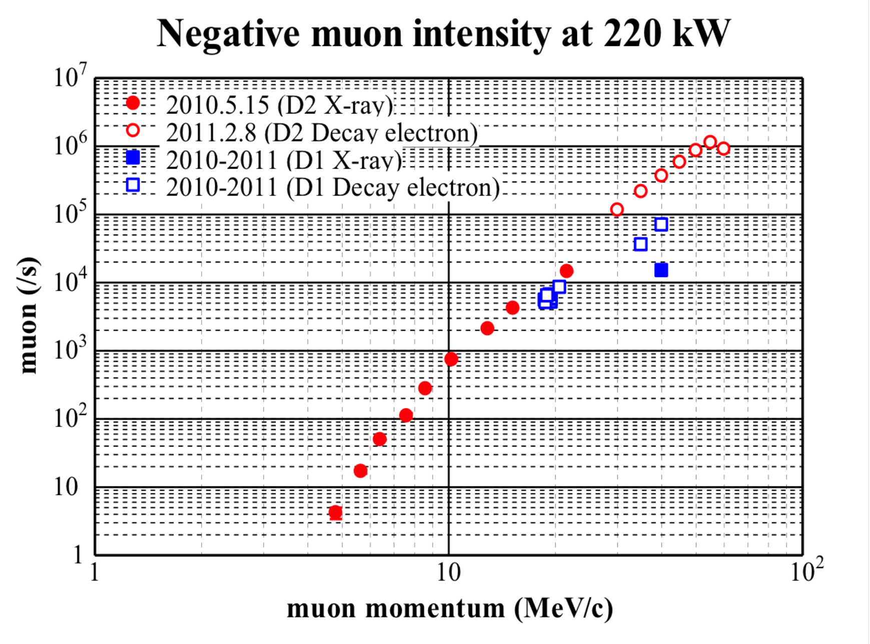

FIGURE 3.3: D2 muon beam intensity at 220kW[26]

Since the operation on November 2009 started, 120kW beam power has achieved world strongest pulsed muon beam with 1.8x10^6 muon per second. Upon achieving RCS proton beam designated value of 1MW, it is predicted that 1.5x10^7 high surface muon field by MUSE. In this current experiment, the beam power is set to be around 300kW and the details of the muon yield will be explained in the corresponding section. The beam energy distribution spread approximately 15% with the beam size at D2 exit 30mm×40mm.

The beam power provides by Rapid Cycle Synchrotron(RCS), delivers double or single pulse beam with a width of 100 ns suitable to users requirement for various solid state physics, material science, physical chemistry, non destructive analysis and particle physics experiment.

3.2 Gamma detectors and shielding

High purity Germanium detector converts gamma rays into electrical impulses which can be used together with suitable signal processing, to determine their energy and intensity. It behaves as the large reverse-biased diode. The contacts on the crystal is required to connect the diode to an electrical circuit to amplify the signal. These thick electrical contacts from Lithium as the N+ contact, and a thin, ion-implanted contact (P+ contact). The lithium contact is thick because the lithium is diffused into the germanium.

The GMX type detector is the n-type coaxial Germanium(Ge) detector with thin entrance windows with thickness from 300μm to 500μm thick. The N-type coaxial (GMX) has extended low-energy efficiency because of the thin contact and has slightly worse resolution specifications at higher energies compare to GEM type detector. Due to clean environment at D2 beam line, only lead blocks are used for shielding. The shielding setup of D2 experiment is shown in Figure 3.2.

3.3 Data taking system

The events needed for the experiment are all muonic X-ray and gamma rays emitted after the muon capture. To make sure that the target is activated, observation of muonic X-ray of the target is very important. In order to realise this, the trigger logic is built with multiple NIM module. The coincidence between muon beam timing and HPGe detector signal is used to check the constructed event of muonic X-ray. The signals through these circuits are processed by the raw data processor and they are written onto PC. The signals from GMX HPGe detector are accumulated in the multi-channel analysers (MCA).

After on beam data taking, the offline measurement are performed. The VME A3400 module is used on the processor the program to transfer the data to the host computer which is called 'Frontend'. There is a main MIDAS server computer which collect all the data from each 'Frontend'. The system is controlled by the main MIDAS server with a web interface. The program which makes online histograms and the program which check the quality of the data is running continuously and connected to the MIDAS server. All the information and errors from each 'Frontend' are issued on the web page.

In offline measurement, the all gamma rays event are needed to enters the HPGe detector. The target is placed as close as possible to the Beryllium window of detector to increase the acceptance of the detector. The off beam measurement is recorded using MCA8000a pocket analyser which connected to HV power supply and CANBERRA Amplifier.

The Amptek MCA8000A is a low power MCA with high performance typically equivalent to the larger MCA systems. It has a significant advantage in size and power compare to other MCAs and requires only computer with a standard RS232 serial interface or USB to RS232 adapter to operate. The performance of MCA8000a is suitable for any solid state detector and at the same time included a friendly software for the user to operate the data acquisition, display, calibration and manipulation of the spectra.

3.4 Experiment setup

Thin enriched molybdenum film with surface thickness of 80mg/cm^2 prepared specially for nuclear rare decay experiment by T.Shima et al. [30] is irradiated by muon beam of 30.0MeV/c. The experimental setup is shown in Figure 3.4. The irradiation of enriched molybdenum target took 8hours and followed by 6 days measurement for delayed gamma rays. The main goal for this experiment is to measure prompt gamma ray and some delayed gamma ray energy which are not observed in MuSIC beam test by double pulse muon beam. However, due to problem with the pile up during the irradiation time, we will not discussed the short-lived gamma-rays ($\tau_{1/2}$ ≤1hour) and only focused on delayed gamma-rays results.

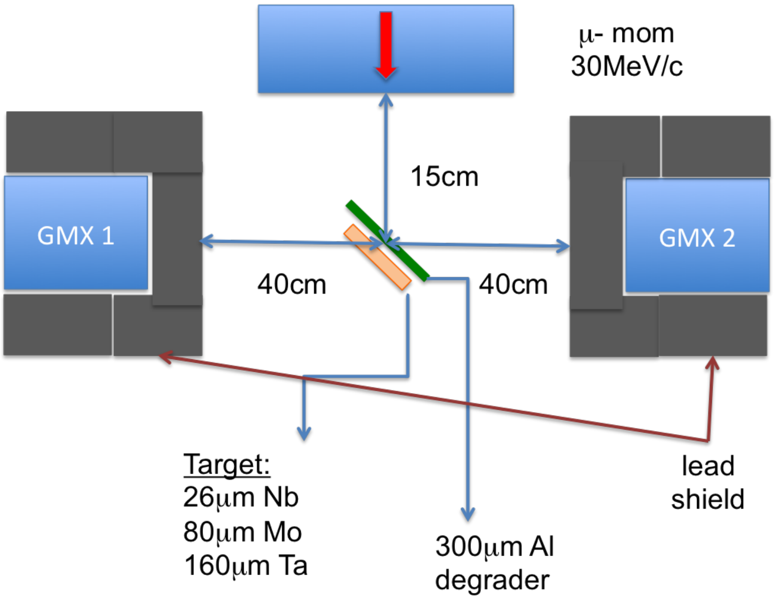

FIGURE 3.4: Muon irradiation at D2

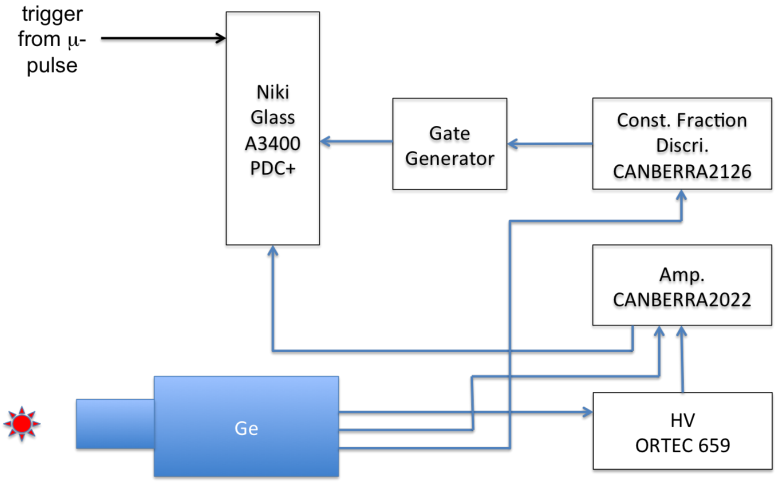

FIGURE 3.5: Trigger logic for D2 beam test

Two high purity germanium detectors are used for the beam measurement, which is set perpendicular from the beam exits. The muon irradiation in MLF-D2 using three targets which are Mo, Nb and Ta. However, only the results of Molybdenum will be discussed here. The HPGe is connected to the amplifier and discriminator to get the timing information for the measurement. The trigger logic of the measurement system is illustrated in figure 3.5.

Chapter 4

Experimental Results

From the gamma-rays spectrum obtained during the measurement, the energy calibration, efficiency correction and nuclear cascade effects have been corrected to get the total gamma yield, Y(γ) at each peaks. The Y(γ) are used further to deduce the decay curve and obtaining the initial radioisotope produce as soon as the beam was stopped. In this chapter, I will presented our first results on the measurement of ^{100}Mo. The detail analysis from the gamma ray spectrum and the decay curve from the measurement will be presented to finally deduced the isotope-mass population distribution.

4.1 Energy Calibration

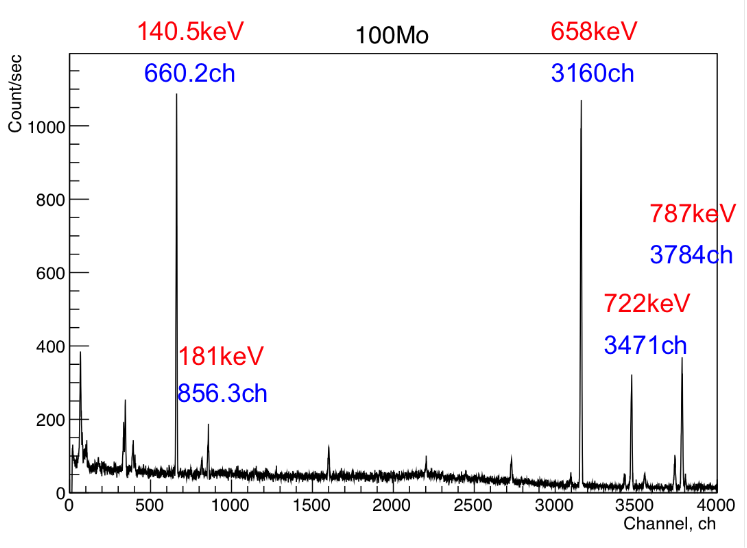

Figure 4.1: Peak assignment from delayed spectrum

The energy calibration of germanium detector is determined by placing the ^{133}Ba standard source (refer to in Appendix B) at the similar target spot during measurement for each detectors. The corresponding energy is assigned to particular channel of potentially high intensity gamma rays emitted by ^{133}Ba source and some gamma rays from background (as shown in Figure 4.1. From energy calibration, the measured channel number can be converted into energy by following Equation 6.1 and 6.2 deduced by Figure 4.2. Since the delayed measurement keep running through around 6 consecutive days, the energy calibration is done by using each molybdenum run. Strong gamma peaks at energy from 140keV to 800keV are used and analysed.

$$Run1 : Energy[keV] = 0.207 \pm 0.001 * ch + 3.853 \pm 0.048 \tag{4.1}$$

$$Run2 : Energy[keV] = 0.207 \pm 0.001 * ch + 3.887 \pm 0.044 \tag{4.2}$$

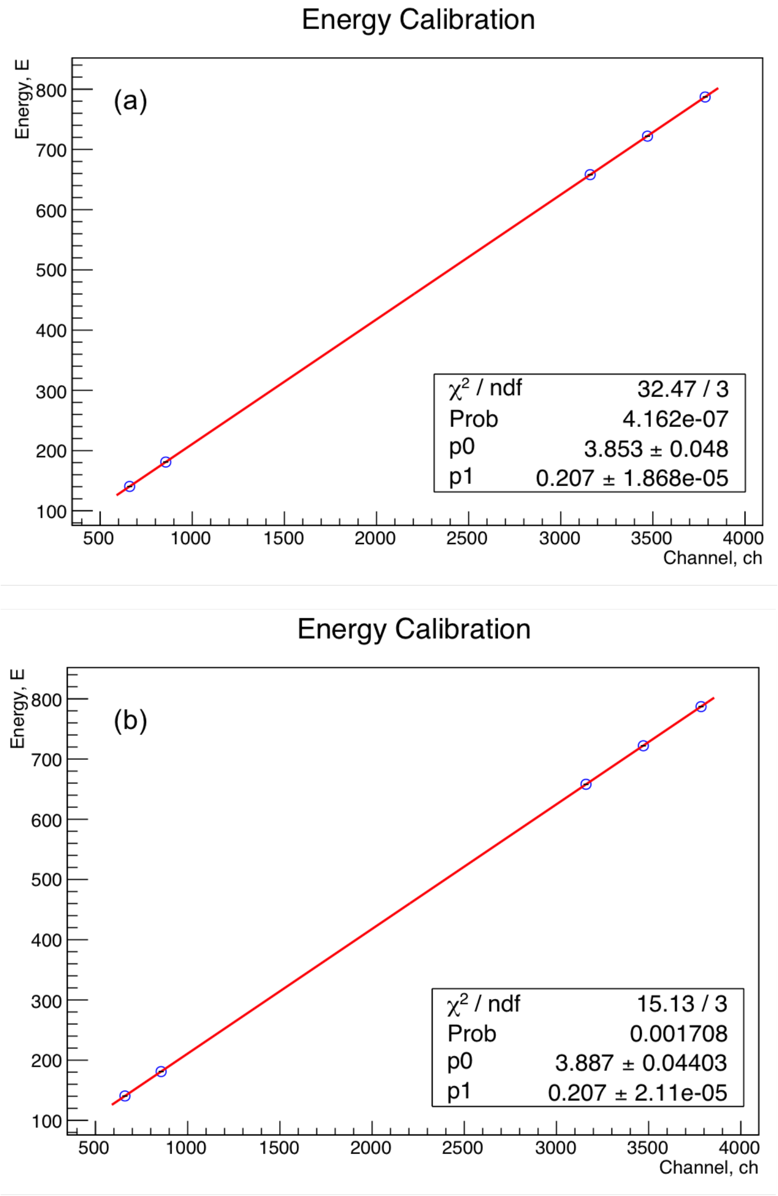

FIGURE 4.2: Energy calibration (a) Run1 (b) Run2

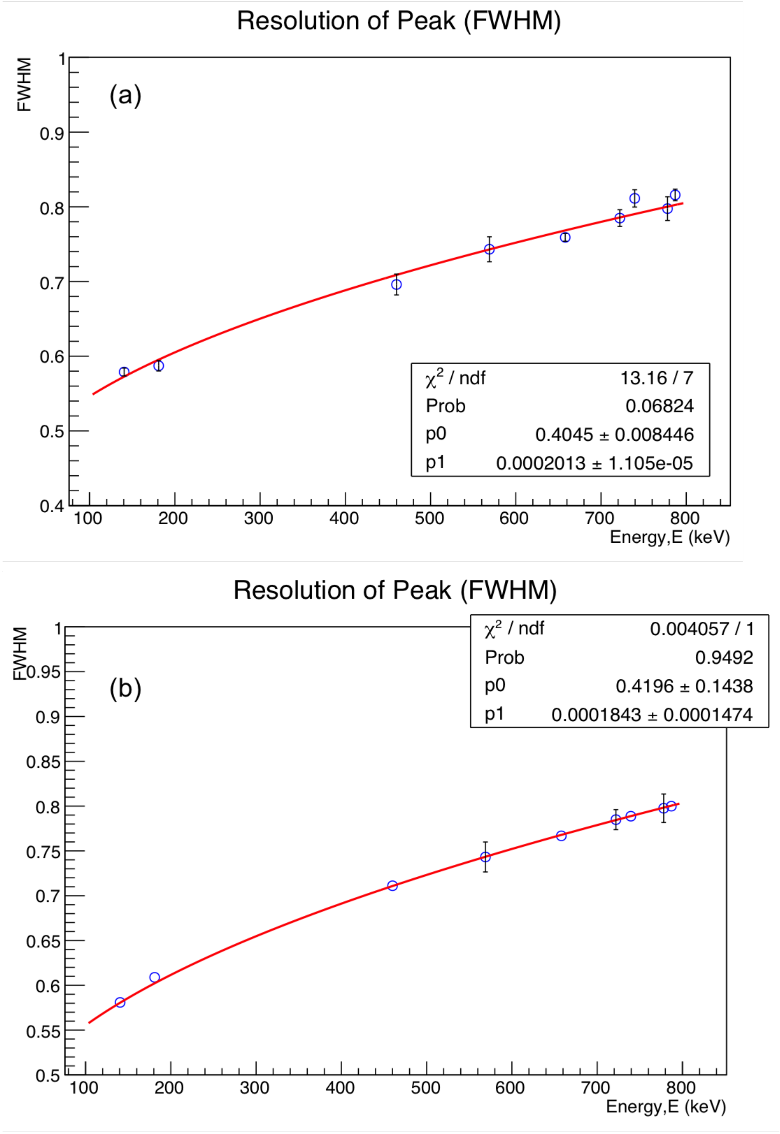

FIGURE 4.3: Consistency check with peak width (a) free (b) fixed parameter

Each peak is at first fit to free parameter of gaussian and linear function which gives the mean, constant and width value of each peak. The peak width of data, source and background peak are than plotted in the same graph to check the consistency of each peak (refer Figure 4.3).

4.2 Detector efficiency

Detector efficiency is calculated from the ratio of total events under peak and the multiplication of measurement time and the activity of the gamma yield corresponds to the current measurement time. Due to the close distance between target and detector in the delayed measurement, the efficiency is extrapolated by the solid angle and the size of germanium crystal of GMX1 to GMX3. The distance ratio of GMX1 with target and the Ge crystal size $\frac{R^2}{r^2} \approx 270$ times however, the crystal size of GMX1 and GMX3 is slightly different by a factor of 1.4 times. Thus, the efficiency of GMX3 is approximately

200times larger than the GMX1 is apply to this analysis and the efficiency simulation also has been done for consistency check. The efficiency curve for GMX3 is shown in figure 4.4.

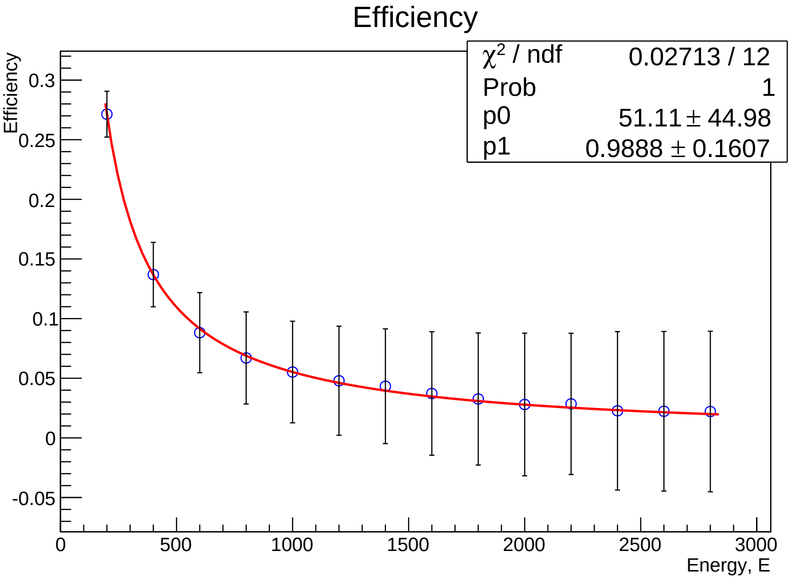

FIGURE 4.4: Efficiency curve by simulation

$$Extrapolation : Efficiency = 8.831 \pm 4.272 * Energy[keV] + 0.819 \pm 0.095 \tag{4.3}$$

$$Simulation : Efficiency = 51.11 \pm 44.98 * Energy[keV] + 0.99 \pm 0.16 \tag{4.4}$$

4.3 Delayed Gamma-ray spectrum

The delayed gamma spectrum is measured up to 120 hours after the irradiation at a low background environment with lead shielding. Most gamma rays observed are from the Nb isomer. Some peaks from Ge nuclei have been observed at 66.7keV and 70keV, might due to the interaction of emitted neutron with the Ge detector [31]. The peaks are fit by the gaussian and linear distribution evaluated using a least squarers fit which yielded the amplitude, width and centroid of each peak. The total events under each peak is estimated and corrected by the branching ratio and peak efficiency.

The strong gamma rays peak from ^{99m}Tc, ^{98}Nb,^{97m}Nb and^{96}Nb in delayed measurement are from the M1, M2, M3 and E2 transitions. Most of them are directly emitted from the excited state to the ground state except from 140.5keV(^{99m}Tc) which is exclusively from the 143keV level ($\tau_{1/2}$=6 hours) which populated by the β decay from ^{99}Mo RIs ($\tau_{1/2}$=66 hours) as a product of (μ,n) reaction on the ^{100}Mo isotope.

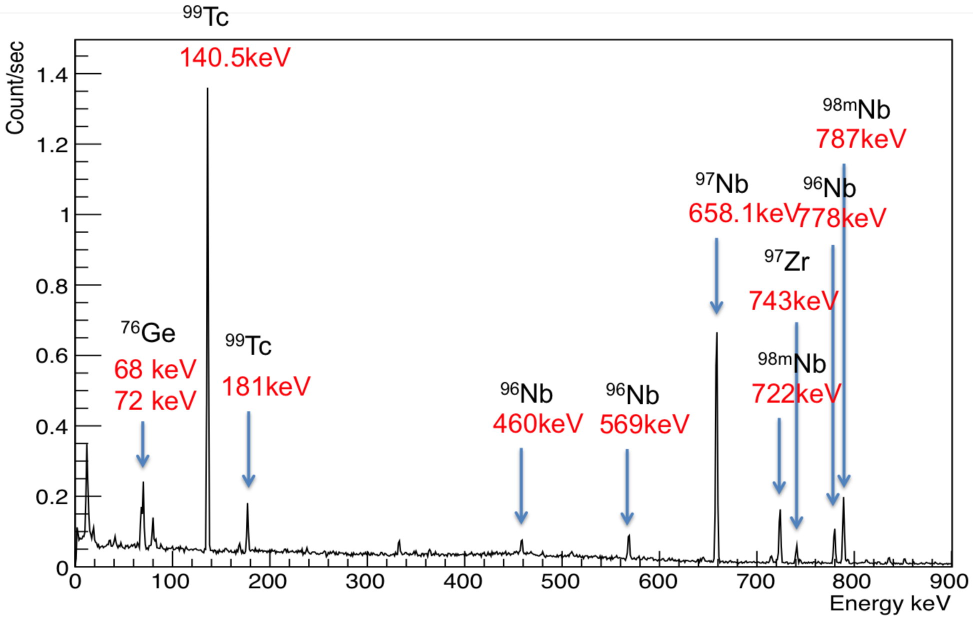

FIGURE 4.5: Energy spectra for off beam measurement

TABLE 4.1: Observed delayed gamma ray at offline measurement

Element	Transition	Energy,E (keV)	Half-life (hour)
^{99}Tc	$7/2^+ \to 9/2^+$	140.5 [32] [16]	66h+6h
^{99}Tc	$5/2^+ \to 9/2^+$	181.0 [32] [16]	66h
^{99}Tc	$1/2^+ \to 5/2^+$	739.5 [32] [16]	66h
^{98}Nb	$4^+ \to 2^+$	722.6 [33]	51.3m
^{98}Nb	$2^+ \to 0^+$	787.4 [33]	51.3m
^{97m}Nb	$7/2^+ \to 5/2^+$	657.9 [34] [16]	72.1m
^{96}Nb	$6^+ \to 3^+$	460.0 [35] [16]	23.35h
^{96}Nb	$6^+ \to 4^+$	568.9 [35] [16]	23.35h
^{96}Nb	$2^+ \to 0^+$	778.2 [35] [16]	23.35h

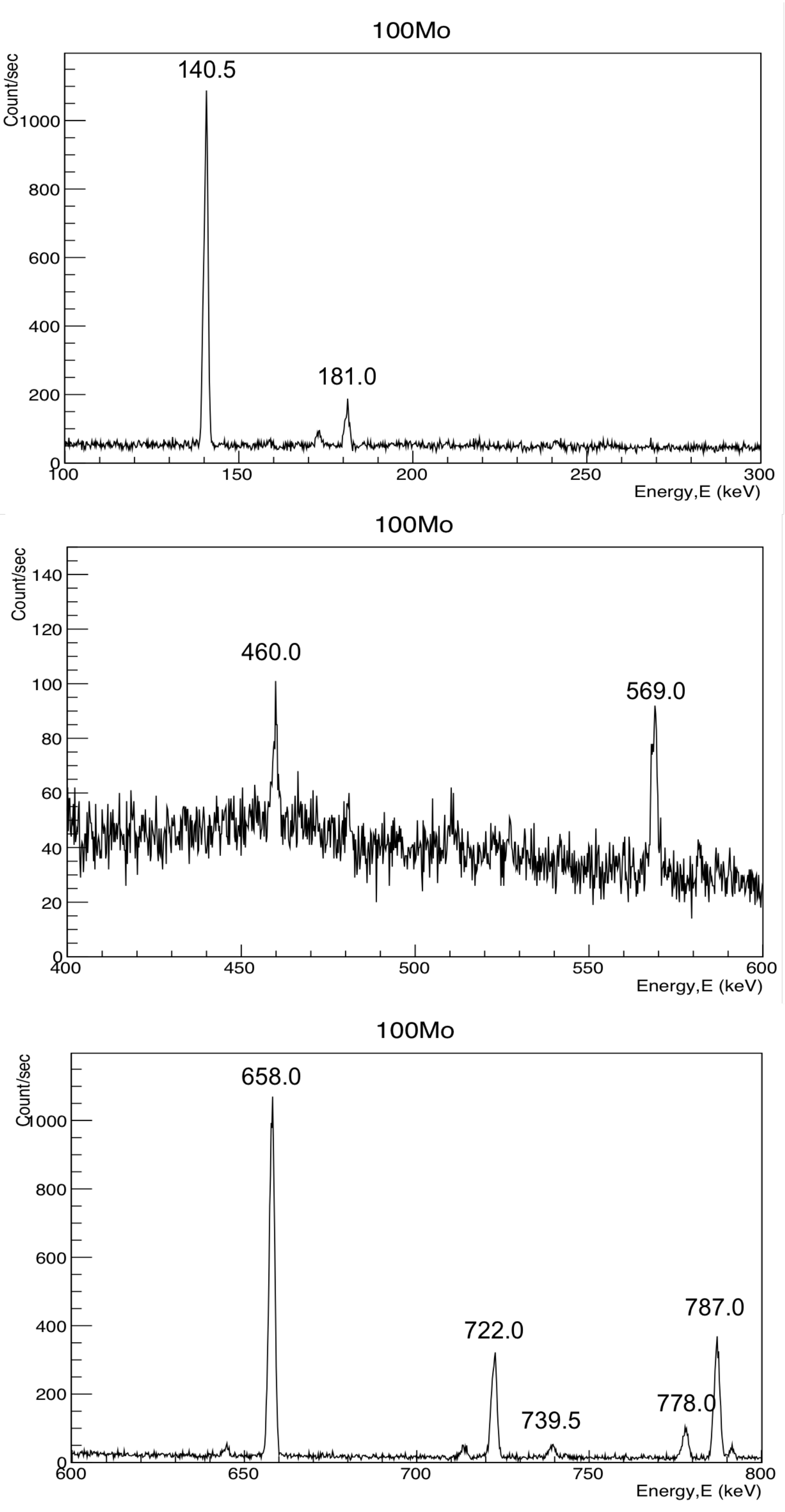

Figure 4.6: Delayed gamma spectra from off beam measurement

4.4 Gamma rays from ^{99}Mo

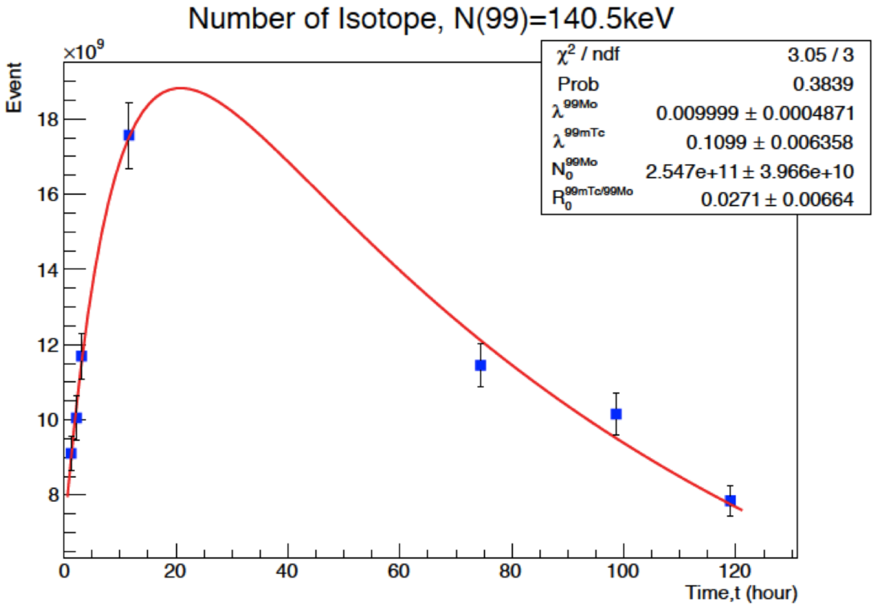

Figure 4.7: Decay curve of 140.5keV

Gamma rays of energy 140.5keV, 181.1keV and 739.5keV contribute to A=99 from ^{99}Mo($1/2^{+}$) → ^{99}Tc(g.s). ^{99}Mo decays by 65.9hours to 142.7keV level and 6hours to ground state. The strong gamma rays of 140.5keV is a cascade energy following 2.17keV from 142.68keV state. It is observed in combination of 69.3±20.5 hours and 6.31±1.73 hours. The number of isotope from N(99) is (6.7±1.3)x10^{9} as shown in figure 4.7. The isotope of 99 from 140.5keV is still observed even though after 120 hours due to its long half-life.

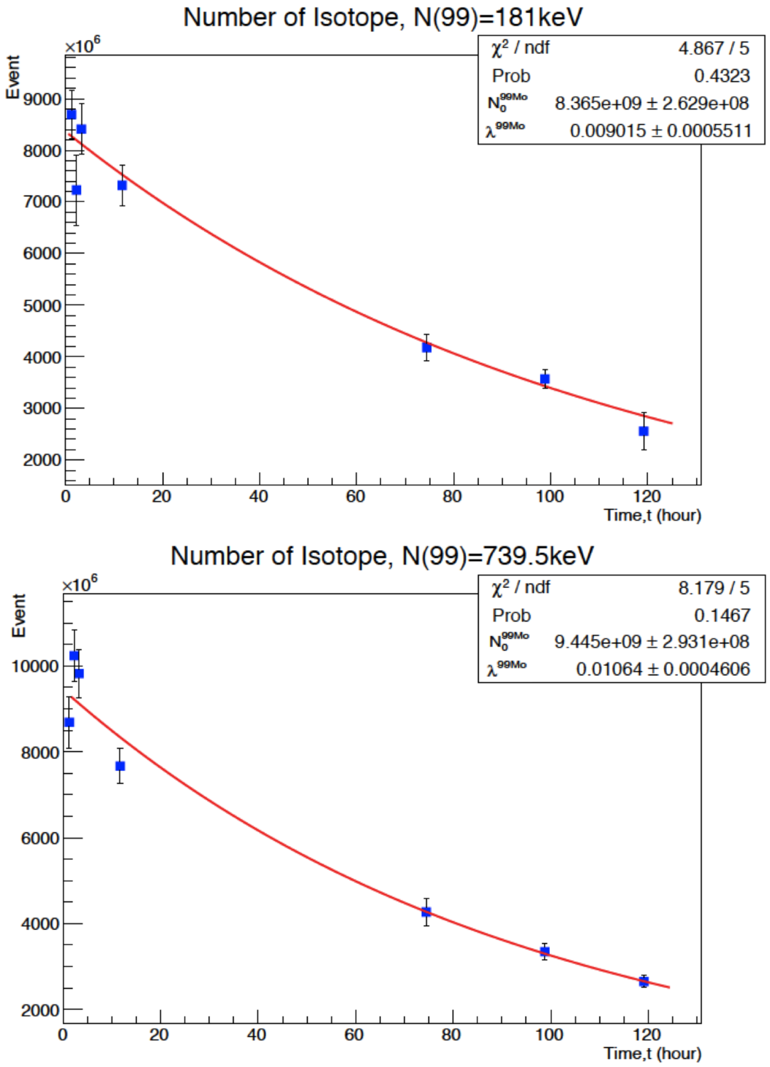

Figure 4.8: Decay curve of (a)181.1keV (b)739.5keV

In case of 181.1keV gamma rays from $5/2^+ \rightarrow 9/2^+$ transition of ^{99}Mo $\rightarrow$ ^{99}Tc is observed after nuclear cascade through 739.5keV which is also observed with number of isotope (8.9±0.4)x10^9 and (9.4±0.3)x10^9 respectively. The beta decay half-life of 181.1keV and 739.5keV is shown in figure 4.8. The number of isotope produced between these three gamma rays are almost the same and within the errors.

4.5 Gamma rays from ^{98}Nb and ^{98}Nb

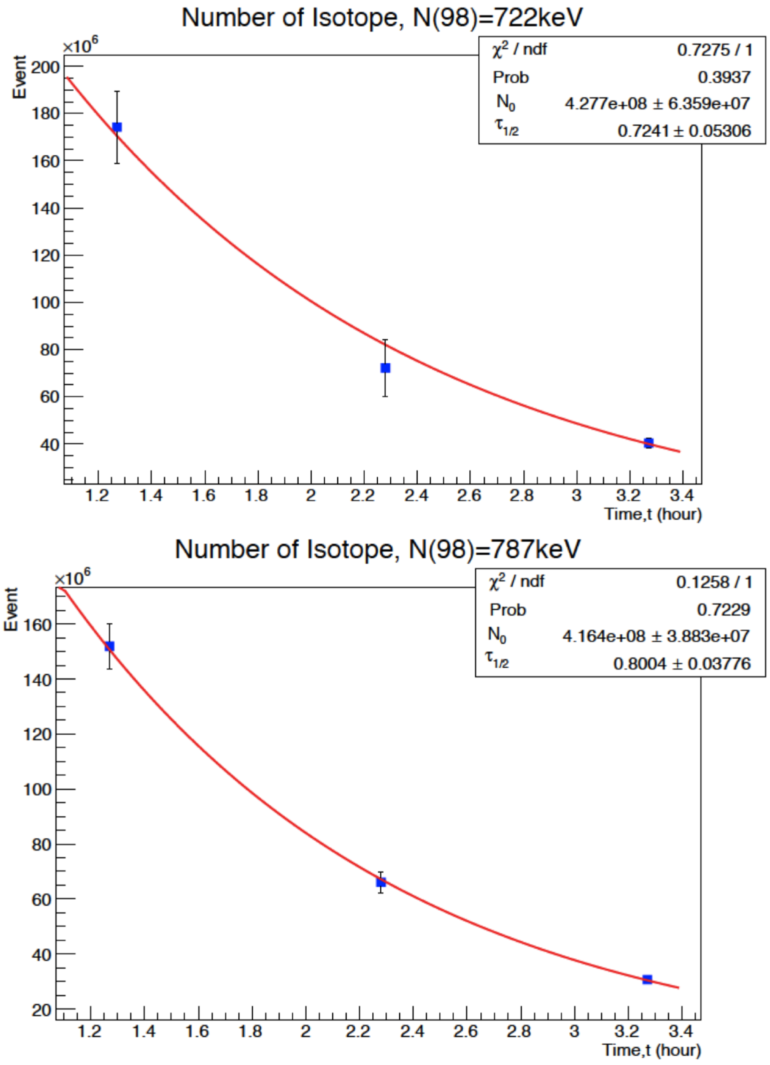

FIGURE 4.9: Decay curve of (a)722.6keV (b)787.4keV

γ rays at 722.6keV and 787.4keV of ^{98}Nb and ^{98m}Nb contributed to number of isotope population at A=98. The 530keV, 1168keV and 714keV gamma rays emits simultaneously with 722keV which allowed cascade effects to the count rate reduced by 67%, results in the number of isotope (4.3±5.5)x10^8 after decay with half life of 1.0±1.4hours (refer to figure 4.9 (a)).

The 787.4keV emitted together with 326keV and 645keV from ^{98}Nb(1^+) → ^{98}Mo(g.s) and three other gamma rays(530keV,1169keV and 1463keV) from ^{98}Nb(5^+) → ^{98}Mo(g.s). From the decay curve obtained by the yield of isotope over time, the half life of the decay is 0.9±2.1hours which is approximately the same with previously observed by [33] and the number of isotope produced at t=0 is (4.2±3.3)x10^8 as shown in figure 4.9 (b).

4.6 Gamma rays from ^{97}Nb

The 657.9keV decays with the half life of 1.86±5.02hours from ^{97}Nb($9/2^+$) → ^{97}Mo(g.s) isomeric transition together with 857keV gamma rays. The (3.6±0.2)x10^8 isotope are produced after the beam stop. The nuclear structure of ^{97}Nb is a simple one compared to other isotopes, the effects of nuclear gamma cascade is not crucial.

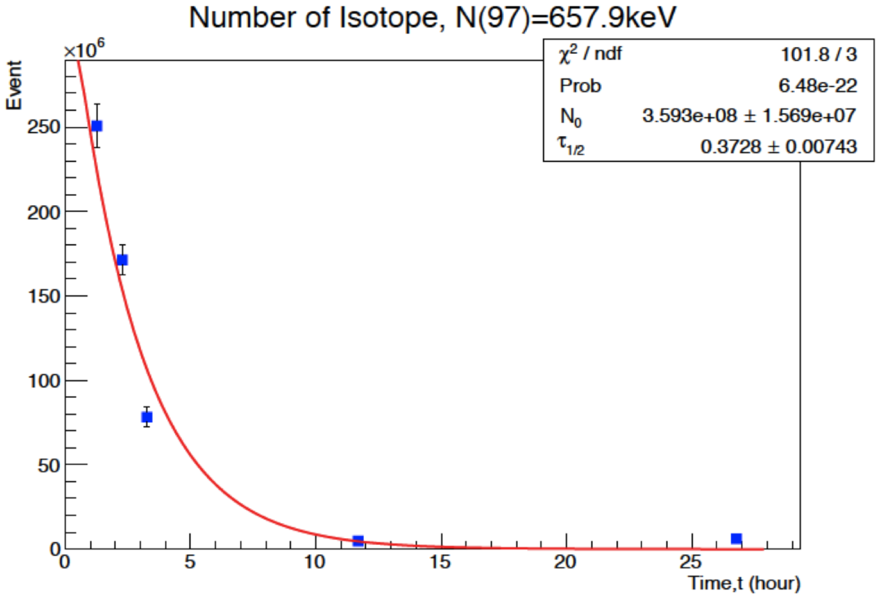

Figure 4.10: Decay curve of 657.9keV

4.7 Gamma rays from ^{96}Nb

The 460keV, 569keV and 778keV are commonly from the transition of ^{96}Nb(6^+) → ^{96}Mo(g.s) at different excited level. The 460keV decays with the half life of 33.4±13.7hours from 6^+ states to 3^+ together with 1200keV and 778keV gamma rays. The (8.2±0.2)x10^8 isotope are produced after the beam stop.

The isomeric transition from ^{96}Nb(6^+) → ^{96}Mo(4^+), emits 569keV together with 3 cascade gamma rays at 241keV, 849keV and 778keV. The (1.0±0.1)x10^9 isotope produced after the beam stop and follows the beta decay half life of 23.35hour by experimentally fit 27.8±3.5hours (shown in figure 4.11(b)).

In case of 778keV gamma rays from ^{96}Nb(2^+) → ^{96}Mo(g.s) isomeric transition is observed after nuclear cascade through 460keV and 1200keV which is observed with number of isotope (5.8±0.2)x10^8. The beta decay half-life of 778keV is shown in figure 4.11(c). The number of isotope produced between these three gamma rays are within the errors.

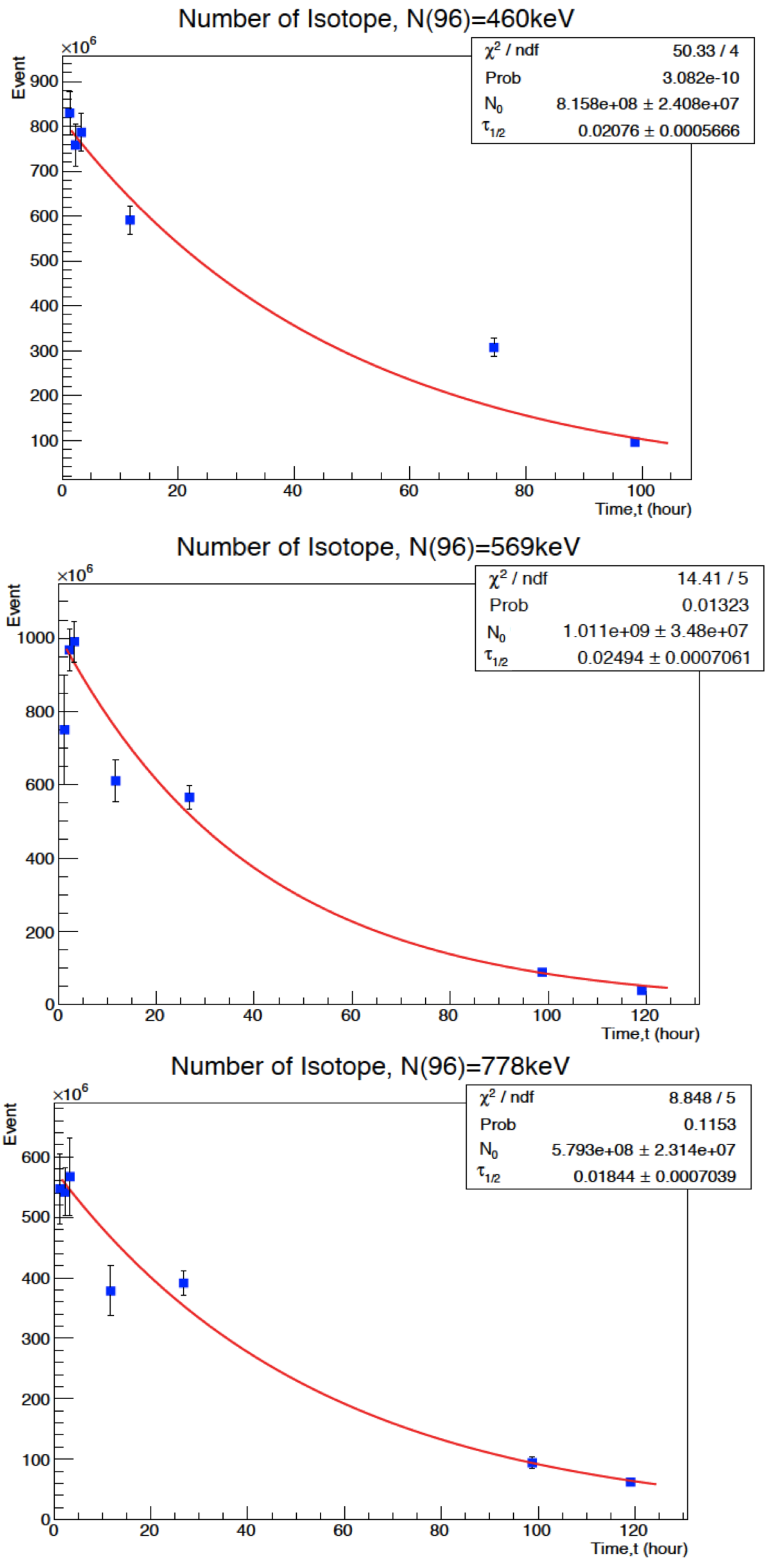

FIGURE 4.11: Decay curve of (a)460keV (b)569keV (c)778keV

4.8 Upper limit of ^{95}Nb

The upper limit of ^{95}Nb is estimated from the 24hours run at t=100hours after the beam stop. The upper limits of 765.8keV [36] from ^{95m}Nb ($9/2^-$) state is determine by using Bayes' rule. The upper limit of the count rates is obtained and undergo the efficiency and branching ratio corrections, resulting the isotope yield, Y(X') is (1.5±0.1)x10^9. Due to the known half life from [36] is about 34.99 days, the correction to number of isotope and gives N(Y) value is (4.9±0.2)x10^8.

4.9 Relative population of isotope

From the analysis of muon activation, the gamma ray yields and the reaction cross section is evaluated to get the population of isotope produce as a product of muon capture process. It is expected to have most isotope population concentrates to A=99 for the enriched molybdenum target since probability of one neutron emissions was higher compare to zero neutron emissions. This isotope population also indicated the probability of neutron emission after muon capture.

Eventhough the value of observed half life is not so different compared to the known half life from [32] [33] [34] [35] and [36]. Figure 4.12 illustrated the fixed half life fitting on the obtained data. The value of fitted N(Y) corresponded to known half-life is summarised in table below.

Table 4.2: Number of isotope, N(X') at fixed half life

Element	Energy,E (keV)	Half-life (h or m)	Number of isotope, N(X')
^{99}Tc	140.5 [32] [16]	66h+6h	(6.7±1.3)x10^9
^{99}Tc	181.0 [32] [16]	66h	(8.8±0.4)x10^9
^{99}Tc	739.5 [32] [16]	66h	(6.4±0.3)x10^9
^{98}Nb	722.6 [33]	51.3m	(5.3±0.3)x10^8
^{98}Nb	787.4 [33]	51.3m	(4.3±0.2)x10^8
^{97m}Nb	657.9 [34] [16]	72.1m	(5.8±0.3)x10^8
^{96}Nb	460.0 [35] [16]	23.35h	(9.3±0.5)x10^8
^{96}Nb	568.9 [35] [16]	23.35h	(1.1±0.1)x10^9
^{96}Nb	778.2 [35] [16]	23.35h	(7.0±0.3)x10^8

In the experiment, we observe many gamma lines with common atomic mass number, A. In order to check the population of isotope at each A, a careful analysis of each gamma lines with correction by detector efficiency, branching ratio and mean lifetime is applied to compare the production isotope. The isotope produced by similar atomic mass number should produce similar number of isotopes. Table 4.4 summarizes the number of isotope production was in the range of 10^8 to 10^9. The upper limit of ^{95}Nb is relatively high compared to other isotope produced after muon capture reaction.

From the fitting, we observed the half life of ^{99m}Tc at 69.0±0.0033 hours and 6.3±0.013 hours, ^{98m}Nb at 0.86±0.029 hours, ^{97}Nb at 1.86±0.0 hours and ^{96}Nb at 28.0±0.0031 hours. Half-life of ^{99m}Tc and ^{98m}Nb are consistent with the one observed by previous

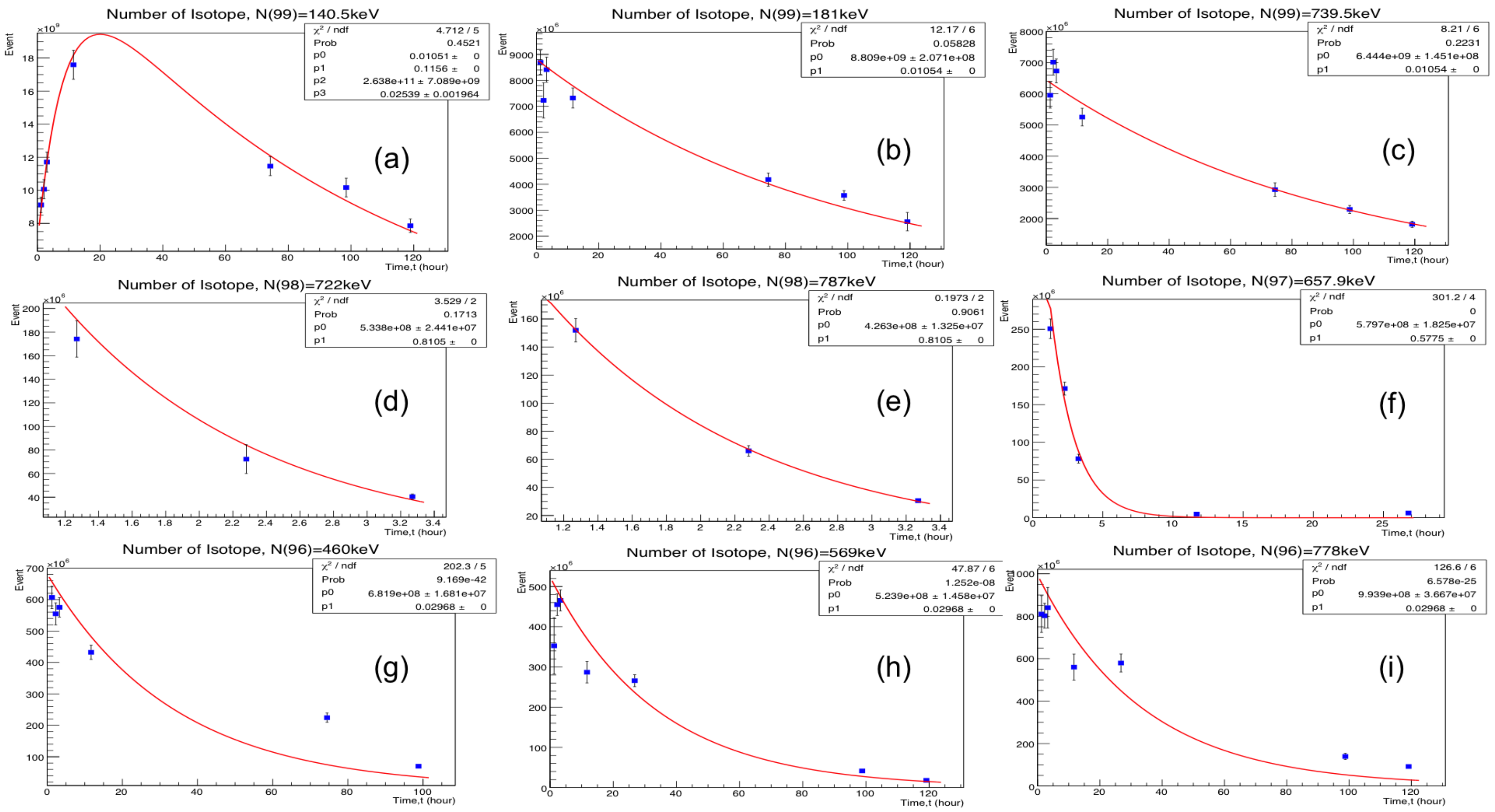

FIGURE 4.12: Decay curve with fixed half life (a)140.5keV (b)181.1keV (c)739.5keV (d)722.6keV (e)787.4keV (f)657.9keV (g)460keV (h)569keV (i)778keV

study reported in table of isotopes and nuclear data sheets shown in table 4.3. However, for gamma rays from ^{97}Nb and ^{96}Nb illustrate slightly different from previous study. Thus, the decay curve is fixed to the reference value and population is evaluated from the curve. By averaging the N(X') observables which have common A, the production rates of each isotope is calculated.

Table 4.3: Nuclear gamma rays half life

Element	Energy,E (keV)	Known $\tau_{1/2}$ (h or m)	Observed $\tau_{1/2}$ (h or m)
^{99}Tc	140.5 [32] [16]	66h+6h	(69.3±3.4)h + (6.3±0.4)h
^{99}Tc	181.0 [32] [16]	66h	(76.8±4.7)h
^{99}Tc	739.5 [32] [16]	66h	(65.1±2.8)h
^{98}Nb	722.6 [33]	51.3m	(0.9±0.1)h
^{98}Nb	787.4 [33]	51.3m	(0.87±0.04)h
^{97m}Nb	657.9 [34] [16]	72.1m	(1.86±0.04)h
^{96}Nb	460.0 [35] [16]	23.35h	(33.4±0.9)h
^{96}Nb	568.9 [35] [16]	23.35h	(27.8±0.8)h
^{96}Nb	778.2 [35] [16]	23.35h	(37.6±1.4)h

Table 4.4: Isotope population for different atomic mass, A

A	Energy,E (keV)	Number of isotope, N(X')	Comments
99	140.5 [32] [16]	$(6.9\pm1.1)\text{x}10^9$	
	181.0 [32] [16]	$(8.4\pm0.3)\text{x}10^9$	
	739.5 [32] [16]	$(6.5\pm0.2)\text{x}10^9$	
	average	$(7.2\pm0.4)\text{x}10^9$	
98	722.6 [33]	$(4.3\pm5.5)\text{x}10^8$	
	787.4 [33]	$(4.2\pm3.3)\text{x}10^8$	
	average	$(4.2\pm3.2)\text{x}10^8$	
97	657.9 [34] [16]	$(3.6\pm0.2)\text{x}10^8$	
96	460.0 [35] [16]	$(8.2\pm0.2)\text{x}10^8$	
	568.9 [35] [16]	$(1.011\pm0.035)\text{x}10^9$	
	778.2 [35] [16]	$(5.8\pm0.2)\text{x}10^8$	
	average	$(8.1\pm0.2)\text{x}10^8$	
95	765.8 [36]	$\leq(4.9\pm0.2)\text{x}10^8$	upper limit

4.10 Isotope Production, R(X')

The isotope production is determined from the calculated N(X') and strongly depends to the half-life of production isotope. Even though the number of isotope from the population shows small value of ^{98}Nb and ^{97}Nb population but the half-life is small and comparable to the irradiation time. Thus, the production rate of these two isotopes gave 25% and 15% of the production after the capture reaction. Due to the pile-up during irradiation measurement, the R(X') for ^{100}Nb in comparably small compare to other isotope. The calculated upper limit estimated for ^{95}Nb from the data is also very small. Thus, we ignored the value of ^{100}Nb and^{95}Nb in Figure 4.13

TABLE 4.5: Number of isotope, N(X') at fixed half life

A	Isotope Production, R(X')
99	$(7.2\pm0.5)\mathrm{x}10^{8}$
98	$(3.4\pm2.6)\mathrm{x}10^{8}$
97	$(2.1\pm0.1)\mathrm{x}10^{7}$
96	$(8.9\pm0.3)\mathrm{x}10^{7}$
95	$(1.9\pm0.5)\mathrm{x}10^{9}$

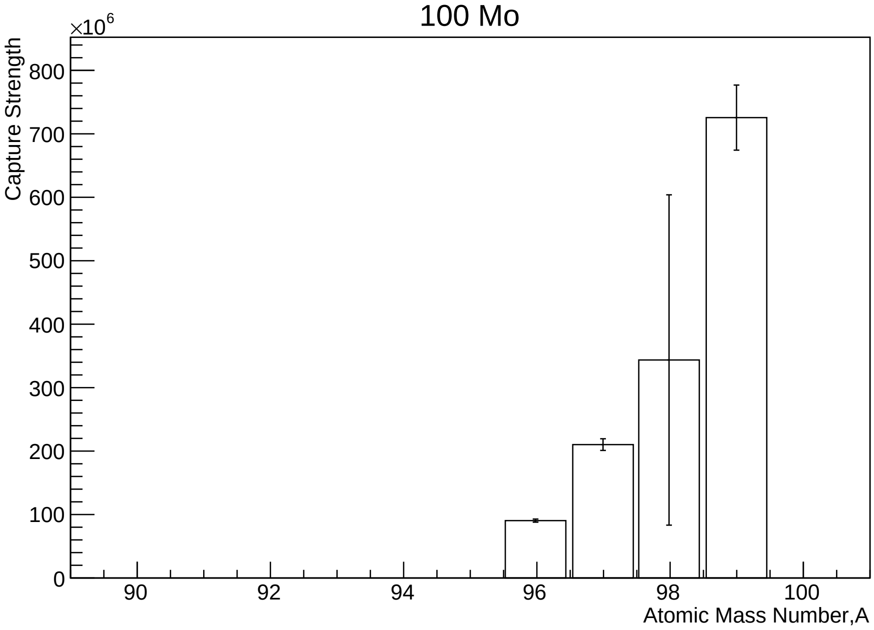

FIGURE 4.13: Capture strength distribution from muon capture reaction on ^{100}Mo

Chapter 5

Neutron Emission Statistical Model

In order to understand the neutron emission following muon capture reaction process and the giant resonances appear in medium-energy excitation region, a statistical calculator is developed from the Q-value of the reaction. With the idea of neutron decays after muon capture, the response strength can be studied. Several parameters are required to reenact the experimental reaction such as varying the percentage of direct and evaporation neutrons emission and the initial excitation energy distribution, E_0^{ex} of excited nuclei and excitation energy of excited nuclei after neutron emission,E_i^{ex}. It allows calculation of radioisotope products populations and beta strength distribution of the reaction. In this chapter, the basic principles of the neutron model will be provide in details. The distribution of kinetic energy, excitation energy and population will be explain explicitly.

5.1 Basic Principles and Assumption

Assuming a negative muon beam is captured by a nucleus at either excited state or ground state of the daughter nucleus, a compound and pre-compound nucleus are formed. The neutrino is emitted accompanying either 1, 2 or zero neutron emission depending on the neutron separation energy. Figure 5.1 will show the remaining energy and momentum of the nucleus after the muon capture reaction. In order for the reaction to satisfy the energy and momentum conservation, the equation below is followed:

$$P + p_{\nu_\mu} + p_n = 0 \tag{5.1}$$

and

$$T + E_{\nu_\mu} + E_i^n = E_0^{ex}. \tag{5.2}$$

Knowing that the nuclear weak response is extracted from squared of NME which consists of wave function at initial state and final state of daughter nucleus. The wave function of initial state is initially unknown, however the final state is obtained from the experimental results of capture strength response. If the initial excitation state exceeds the neutron separation energy, there will be a possibility of more than one neutron emission and formation of isotope with lower proton number, Z [12][7].

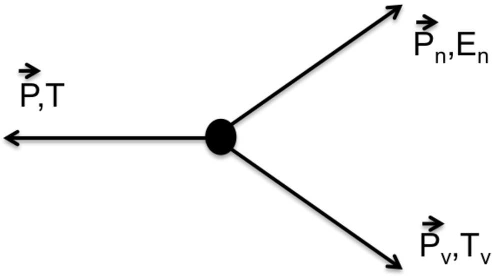

FIGURE 5.1: Momentum balance after the beta decay of a nucleus

$$F(E_i^{ex}) = F(E_\nu) = B(\mu)(E_i^{ex})^2 \tag{5.3}$$

where F(E_i^{ex}) is the distribution of excitation energy of compound nuclei, F(E_ν) is the energy distribution carried away by neutrino, B(μ) is the strength of the reaction at corresponding excitation energy E_i^{ex}. The capture strength indicated the reaction products after muon capture, in this case we defined from the isotope production from the population at low lying states. Refer to figure 5.2 for the illustration on the layout of the neutron statistical model. At different initial excitation energy, E_0^{ex} the number of neutron emission varies and will be followed by the transformation of either beta decay or delayed beta decay together with the transition of gamma rays to ground state [37].

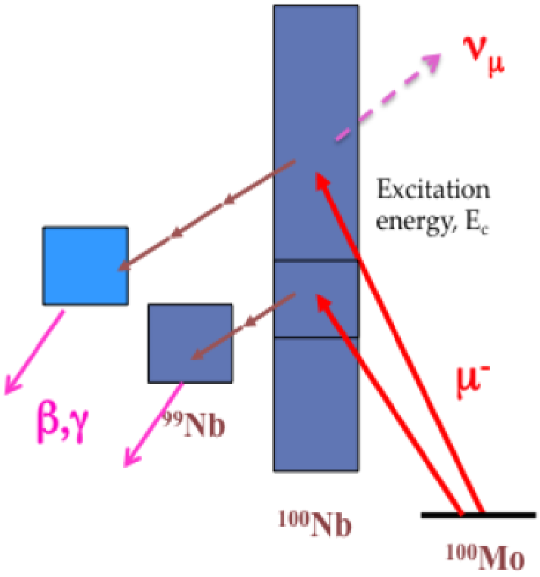

FIGURE 5.2: Layout of neutron statistical model with muon captures on target nuclei and emission of x neutrons

Some assumptions are used to simplify this model. There are listed as below [29]:

a) **All muon captures in nuclei will perform a compound and pre-compound nuclei which is excited and undergo isomeric transitions and neutron emission.**

When the muon beam energy interacts strongly with the clusters of nucleon in a target, the nuclear cascade are initiated and produces the excitons. If the energy is strong enough, reaction products may be emitted before reaching the thermal equilibrium, namely the pre-equilibrium(PEQ) phase. When the thermal equilibrium achieved, the equilibrium(EQ) phase was form and distributed over the whole nucleus.

b) **There is no proton emission due to Coulomb barrier.**
During the feasibility test using ^{Nat}Mo and current measurement using ^{100}Mo, we can not observed gamma rays related to one proton emission. Due to that, we assume that no proton emission occurs during the reaction corresponds to higher proton separation energy compared to the neutron binding energy contribute to high Coulomb barrier. In future, we will include some proton emission in the calculation.

c) **Neutron emission in pre-equilibrium (PEQ or direct neutron) state or equilibrium(EQ or evaporation neutron).**
As suggested by reference [12] and [17], when the high energy neutrino emitted causing some nucleus to be recoil and emission of neutron at any direction. Some neutrons contains higher energy and emitted directly after the reaction, some neutrons are only emitted after the thermal equilibrium are reached due to its low kinetic energy.

d) **The nuclear level density was set to be constant, a=12MeV.**
Phenomenologically, a=12MeV reproduced the neutron kinetic energy spectrum for nuclei with mass region of A=100 but it is not exactly the same value. Further study about the value of nuclear level density effects to the isotope population after muon capture should be studied.

e) **The nuclear temperature, T_{EQ} is defined from the excitation energy of nuclei and directly proportional to E_i^{ex}.**
The concept of nuclear temperature describe the formation and decay of the compound nucleus in particular reaction. Due to excitation by muon, the nuclear temperature is obtained from the excitation energy of the nucleus after the muon capture and after decay of neutron.

f) **A realistic neutron binding energy is used as the threshold energy of one neutron emission.**
The real value of the neutron binding energy are used in this calculation from the mass difference of the nuclei after one neutron emission.

$$B_i^n = -M(A,Z) + M(A-1,Z) + n \tag{5.4}$$

This statistical calculator allows the calculation of isotope-mass population by assigning some distribution to the initial excitation energy, E_0^{ex}. The effects of fraction of PEQ and EQ phase towards the isotope population are also studied. The following description of the neutron statistical model is referred from [12] and [37].

5.2 Initial Excitation Energy, E_0^{ex}

The study of the giant multipole resonance in nuclei received significant curiosity among nuclear physicist since the past quarter century. The excitation of giant resonances depends on the nuclear probe used on target nuclei in the range of light to heavy nuclei. In muon capture reaction, excitation of the giant multipole resonance(GMR) plays an important role as suggested by H.Uberall [38]. The generalised Goldhaber-Teller model and its extended effect of collective monopole and quadrupole oscillations of the nucleus in addition to the dipole states helps to explain the connection well. GMR is a highly collective modes of excitation in the nuclear continuum, the significant fraction of the nucleons inside the nucleus move along together and characterised as oscillations with various multi-polarities.

$$P(E_i^n) = 1 - exp[-(Q - B_i^n)/T_{EQ}] \tag{5.5}$$

In the study of neutron emission after muon capture on light nuclei such as ^{12}C by G. H. Miller [22] and ^{16}O by H.Uberall [38], the gamma de-excitation subsequently with the nuclear cascade process resulting final nuclear polarisation and gamma-neutrino angular correlation coefficient investigations. The studies give useful information about nuclear structure of excited nuclei.

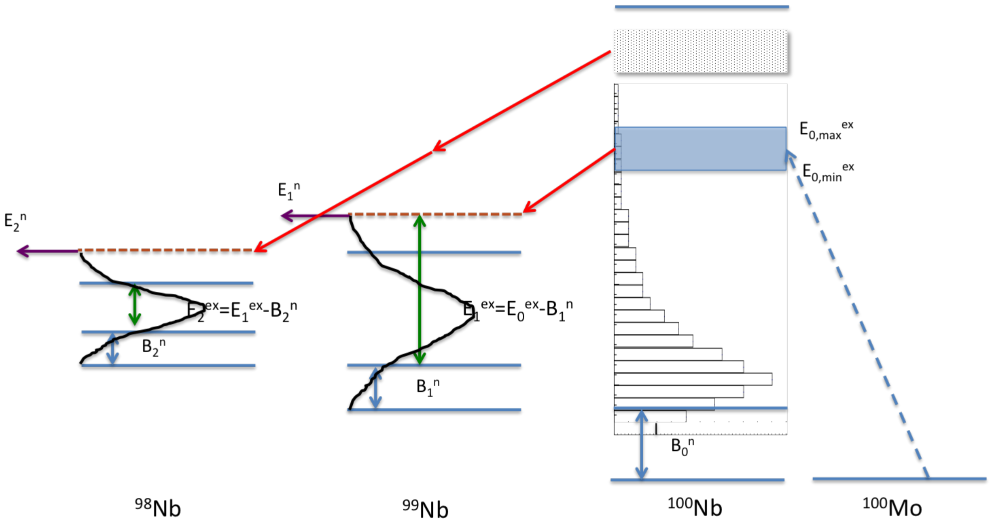

FIGURE 5.3: Excitation energy distribution of the statistical calculator

In this model, the maximum energy of E_0^{ex} corresponds to the Q-value of muon capture. Mukhopadhyay [26] suggested that there will be several excitation after muon capture as shown in figure 5.3. The initial excitation energy gives the number of maximum neutron emission and RIs production after neutron emission of ^{100}Mo is studied. E_0^{ex} is set to follow the normal distribution labelled as S(E_0^{ex}) in Figure 5.4.

5.3 Excitation Energy, E_i^{ex}

Excitation energy, E_i^{ex} corresponds to the energy of excited nuclei after muon capture. The maximum energy is defined when the E_0^{ex} is higher than threshold energy which are the neutron binding energy, B_i^n. The excitation energy of cascade nuclei after one neutron emission reduced by the emission of neutron kinetic energy and so on. Thus, the nuclear temperature of each compound nucleus also reduced until it reached the 0MeV excitation energy via cascade process. Due to mono energetic neutron emission, the range of E_i^{ex} becomes wider as the neutron emission increased.

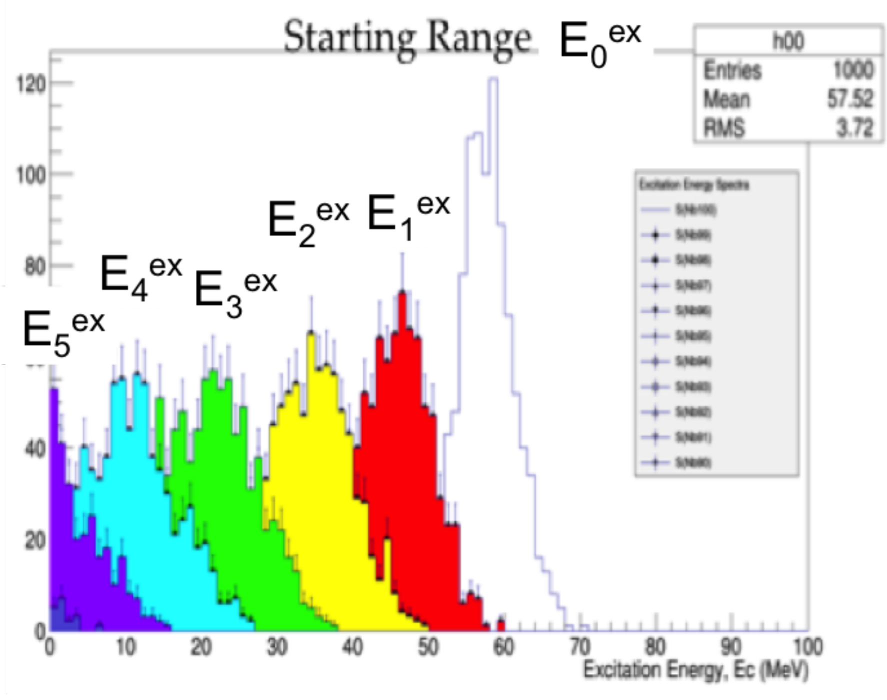

FIGURE 5.4: Excitation energy spectrum for ^{100}Mo

5.4 Neutron Kinetic Energy Distribution, E_i^N

In nuclear reaction, if the projectile energy is high enough to interact with nucleon or clusters in nuclei, nuclear cascade may initiates at pre equilibrium stage and some fast particles are emitted. Neutron emission following the capture reaction carrying some energy and usually emitted in equilibrium state (EQ) and pre equilibrium state (PEQ). The thermal neutron emission follows thermal equilibrium state shown by

$$F(E_i^n) = E_i^n exp(-\frac{E_i^n}{kT_{EQ}}) + x_p * E_i^n exp(-\frac{E_i^n}{kT_{PEQ}}) \tag{5.6}$$

If these PEQ and EQ reactions leave residual nuclei in excited states, they de-excite by emitting γ-rays or conversion electrons or both. By selecting properly the projectile (mass and charge), incident energy and target nucleus, one may populate a particular region of residual state in wide range of N, Z, E, I, K and T space. Experimentally, 10% neutron emission comes from PEQ state and the remaining 90% contributes to EQ state

[23]. The ratio of PEQ to total neutron emission is studied in this calculator in order to reproduce the experimental observation.

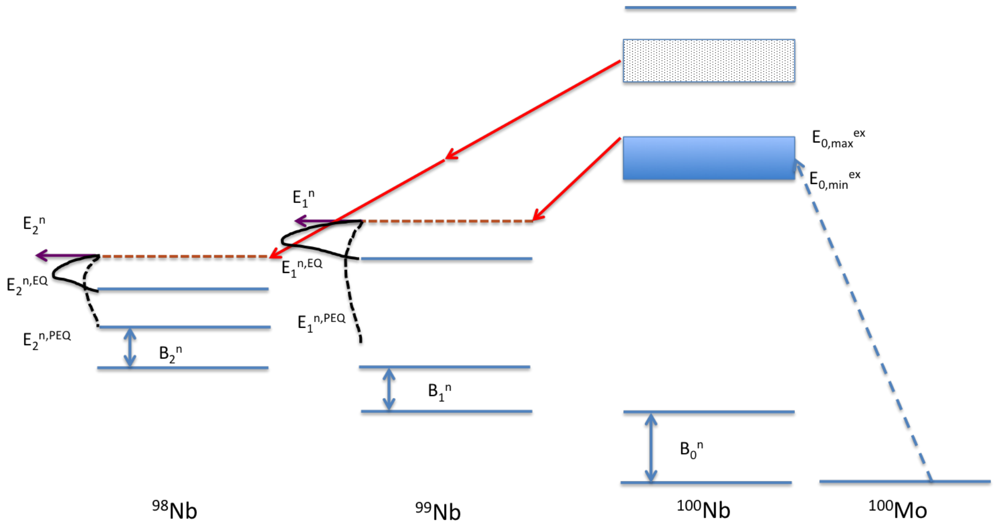

FIGURE 5.5: Distribution of neutron kinetic energy of the statistical calculator

In the previous work by Kaplan et al.[39] there is no experimental distinction between the direct (PEQ) and evaporation (EQ) neutrons. Thus, in their experiments appropriate percentage of neutrons emission should be included. They suggested 15-20% emission of direct neutron is in agreement with their study on aluminium to lead nuclei range. In order to estimate the error of the statistical calculator, three conditions of PEQ percentage which are 15%, 22% and 32% shown in Figure 5.6.

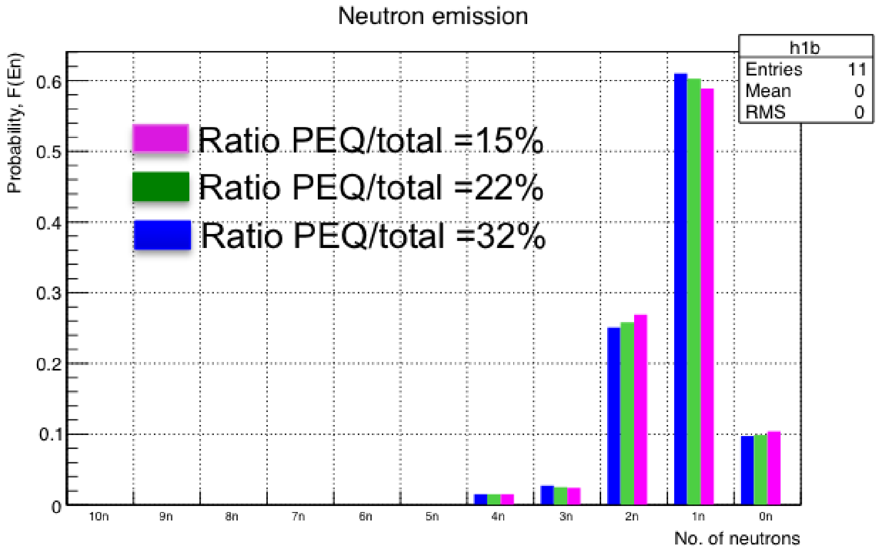

FIGURE 5.6: Neutron energy spectrum for ^{100}Mo (a) 15 percent of PEQ event (2) 22 percent of PEQ event (c) 32 percent of PEQ event

5.5 Population of low-lying levels

The distribution function of excited region is estimated from the energy of emitted neutrino. If the neutrino energy is high, the phase space constant is small. The distribution at first excited nuclei are subtracted with the neutron energy. Since the neutron energy is not mono-energetic, the excitation energy spectrum became wider as the neutron cascades. The more neutrons emitted from the nuclei, the wider the isotopes population are distributed.

Figure 5.4 shows that the statistical estimation of excitation region at each low-lying level. By referring to the natural abundance of the isotope, the fraction of enriched and natural isotope can be determined. The population of production isotope strongly dependence to their neutron binding energy and initial excitation region in GMR.

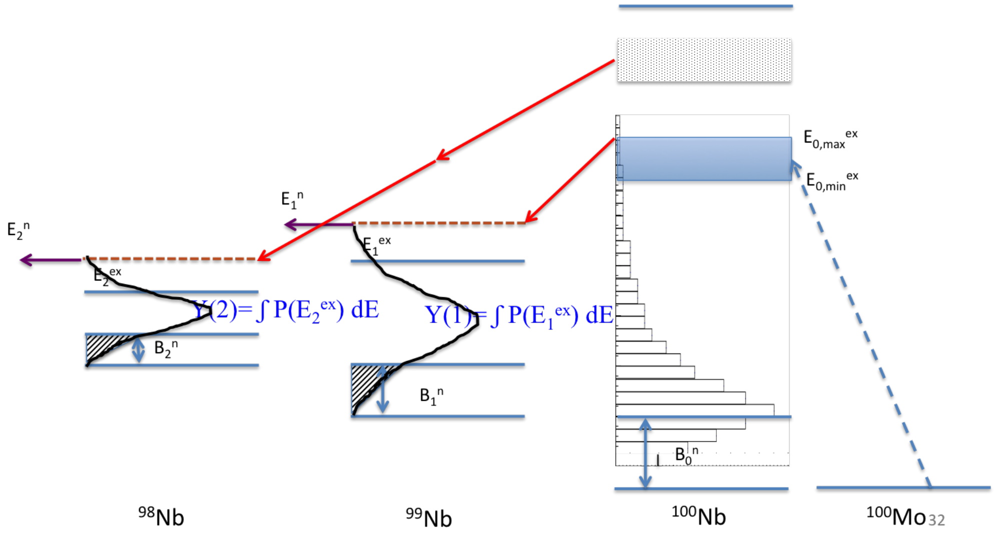

FIGURE 5.7: Isotope population distribution of the statistical calculator

In case of initial excitation energy, $S(E_0^{ex})$, if the energy of neutron is higher than the threshold boil off energy than there is probability to emit one or two neutron. The integration of the exception probability gives the population of low lying isotopes with probability of neutron multiplicities.

We compare the population of isotope for different fraction of neutron emitting in EQ and PEQ stage. When the initial excitation energy becomes higher, the population of isotope distribution becomes broader and the range of neutron emission becomes wider. The majority resonance peak also shifted as the excitation energy is increased. It corresponds to the Q value of muon capture as the maximum excitation and the neutron binding energy as the threshold point of neutron emission.

The population of isotope with excitation energy difference of 10MeV and 5MeV is studied to check the fraction of isotope from all level de-excitation. For the excitation at 0 to 10MeV, the binding energy is high enough to allow only a small fraction of neutron emission and leaving the remaining 63% of A=100 isotope populate at level without emission of neutron. At higher energy range 50 to 60MeV the binding energy is comparable to the excitation energy caused more neutron to emit up until 6n emission. The broader range of neutron emission can be observed. As the isotopes are further from the target atomic mass number, the binding energy became larger and the chance of neutron emission reduced. When the energy step is reduced, the probability of neutron emission is also reduced.

For the case of enriched molybdenum, there will be at least 1 or 2 neutrons emission at excitation energy difference of 5MeV compare to 3 or 4 neutrons emission when 10MeV energy difference. The significant difference between neutron emission by enriched or natural target following muon capture reaction strongly effected by the purity of the target and contribution of the impurity might vary the population of low lying states.

In order to estimate the error from different fraction of direct neutron and evaporation neutron. The increment from 15% to 35% of direct neutron gave small changes to the relative population production. Since the fraction of PEQ to EQ is never suggested in previous case and from the calculation by Miller suggested that the ratio of direct emission neutron is 15% of total neutron emission. The average for all population in 3 separate cases of neutron emission fraction only effected by about 3-5%. Thus, in the following estimation the fraction of 15% of PEQ and 85% is applied to all calculation.

Different treatment is assigned to the population distribution of ^{Nat}Mo and ^{100}Mo. In this section, the composition of isotope contains inside the target sample is very crucial. By simple approximation using natural abundance of ^{Nat}Mo and 100% abundance from ^{100}Mo may help to simplify the statistical model.

5.6 Performance of Neutron Statistical Model

The performance of the model is check by some initial excitation energy range, ΔE_0^{ex} of 5MeV. In section 5.2 we discussed the distribution of initial excitation energy following the realistic normal distribution. Let's assume that 100% contribution are from 5-10MeV, 10-15MeV, 15-20MeV and so on until the maximum excitation energy is the Q-value of muon capture reaction (shown in Figure 5.8).

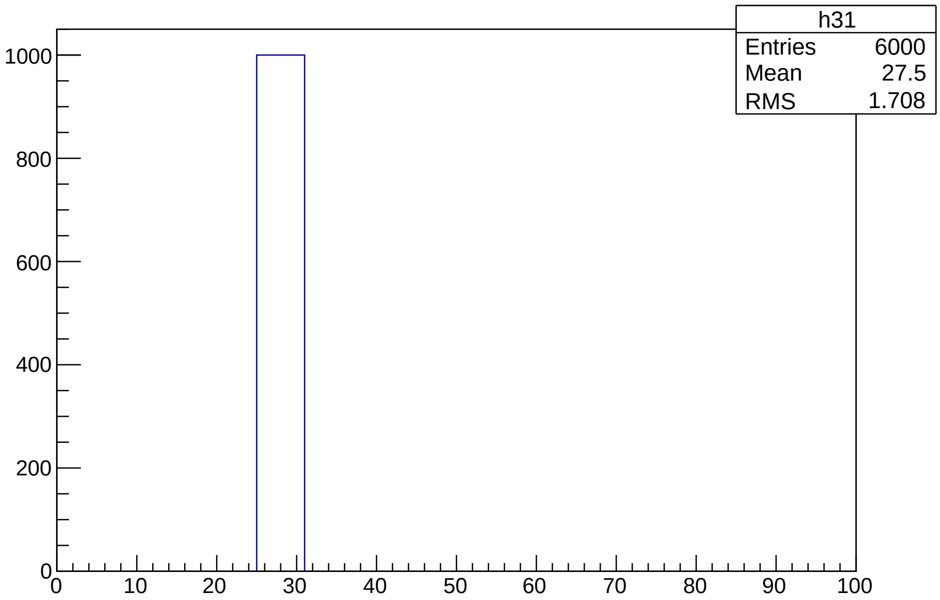

FIGURE 5.8: Initial excitation energy with energy difference 5MeV

The neutron of 22% of PEQ state fraction is used for the following model description of population distribution. The raw population distribution is observed to be up to 3 or 4 isotope population for different mass number,A indicates the neutron multiplicities after muon capture. From figure 5.9 it can be seen that the distribution becomes broadly distributed when the excitation energy is higher. The average of the population and excitation energy are plotted in figure 5.10 shows that at higher nuclear excitation, there is a possibility to observe the nucleus far away from β stability line.

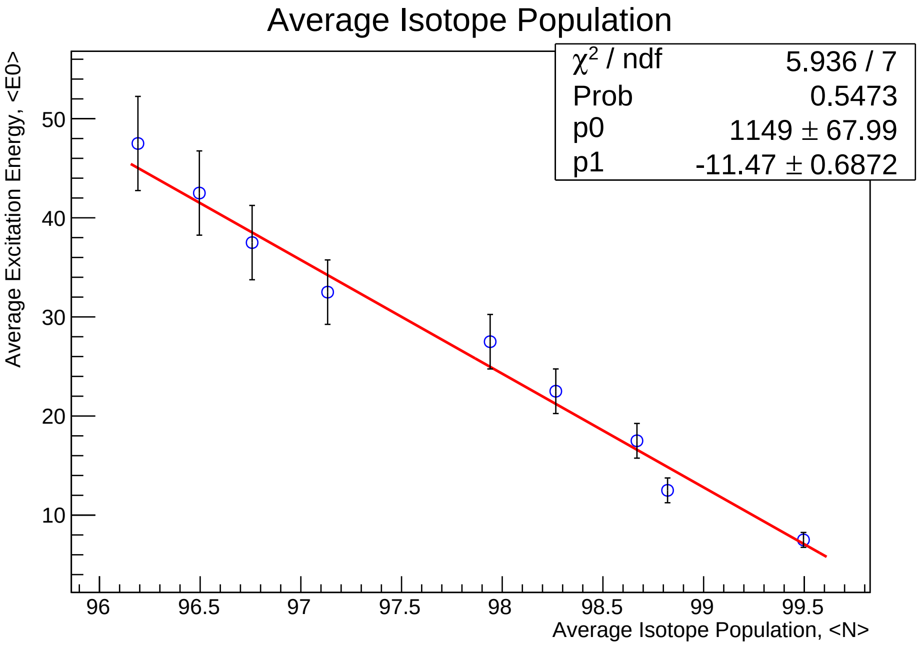

FIGURE 5.10: Average isotope population for corresponding nuclear excitation

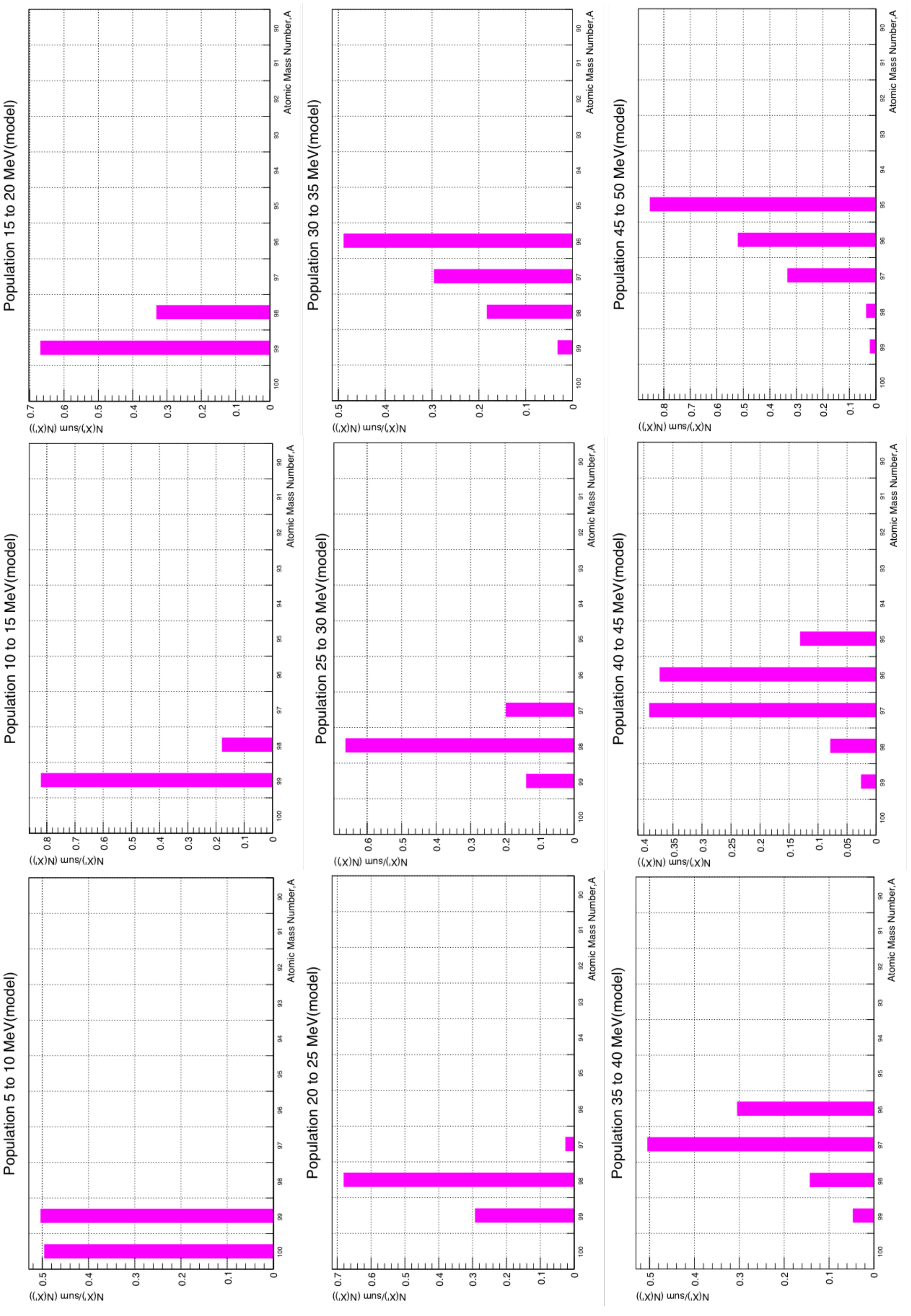

FIGURE 5.9: Raw population distribution when nuclear excitation from 5 to 50MeV

Chapter 6

Comparison with the Neutron Statistical Model calculations using various Capture-Strength Distributions

The analysis of number of isotopes is done by calculation of yield per time with the correction of branching ratio and the efficiency. The observed number of isotopes production is in the order of 10^8 to 10^9. Except for ^{100}Nb isotope, the peak is clearly observed in the spectrum but the total significant event is suppressed due to pile up problem in the measurement. Also the calculate upper limit of ^{95}Nb is too high compared to other observe isotopes. Thus, the result of ^{100}Nb and ^{95}Nb is not included in the comparison.

In this chapter, five models (A, B, C, D and E) are introduced to explain the nuclear excitation region of initial isotope. From observation shown in chapter 4, it can be found that most isotope populated after emission of 1 neutron. Thus, the models introduced have the largest contributions from excitation energy at 10 to 15MeV. We believe that some portion of excitation energy range is required to reproduce the experimental results. Thus, at each multistep excitation the neutron binding energy and are therefore important to explain the experimental results observed by ^{100}Mo measurements.

There are several parameters effected the isotope population distribution:

1) The energy step ΔE_0
2) The excitation energy, E_0 range (low, medium, high)
3) The position of main excitation peak (from experimental observation 10-15MeV)

Model A consists of low energy range excitation energy starting from 1 to 40MeV. From this proportion, only 99 isotopes are populated the most compare to other isotopes observed in MLF experiment as shown in figure **??**. This comparison shows that wider excitation energy is important to explain the remaining isotope in MLF cases.

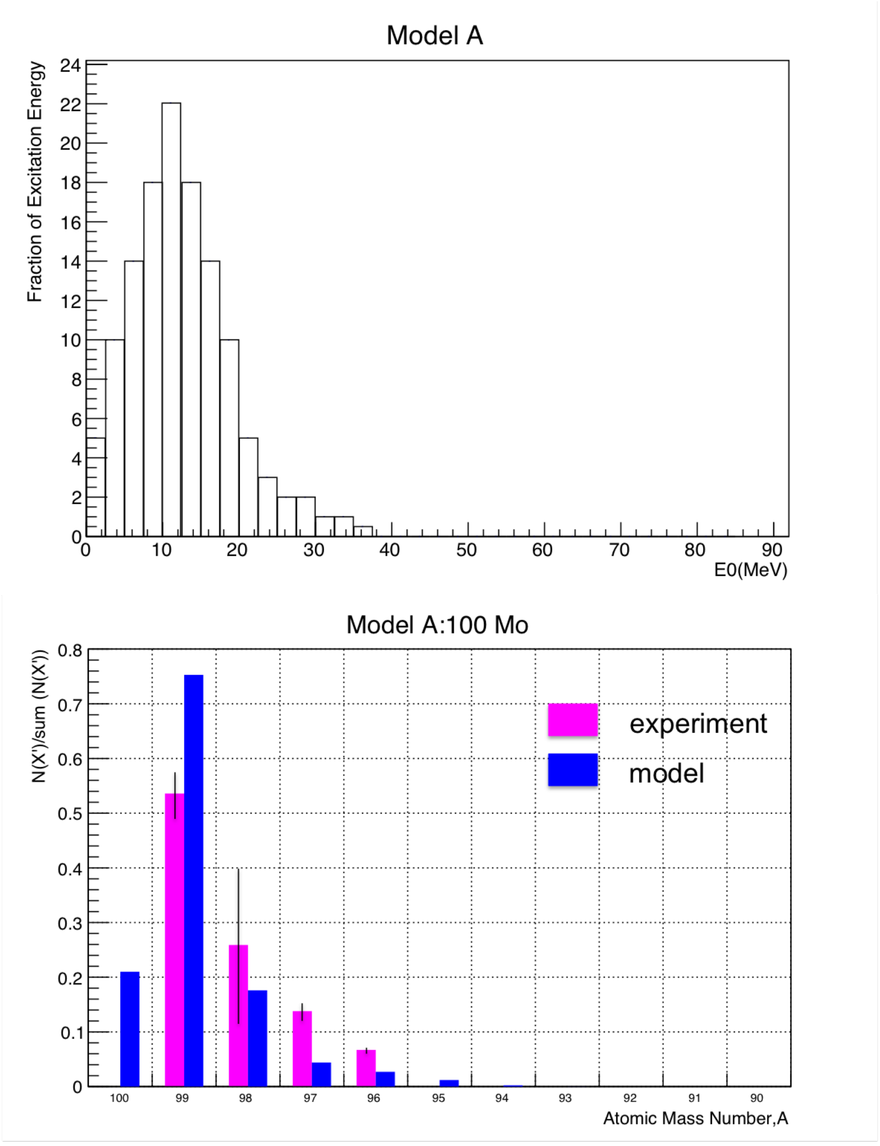

FIGURE 6.1: Model A: Nuclear excitation energy fraction and comparison model A with experimental observation by 100 Mo

Due to many isotope is not observed by the model A compared to the experimental results, we introduce model B which include wider E_0 range (0 to 70MeV). The outcome of this model is plotted in figure 6.2. The isotopes up to 3 or 4 neutron emissions are statistically observed by the model and the tail of isotope production which are far from the stability line have begin to populate. However, due to the position of maximum excitation is around 15 to 22MeV, the higher A isotope is populated less than observed in the experiment while more population is spotted at lower A isotopes.

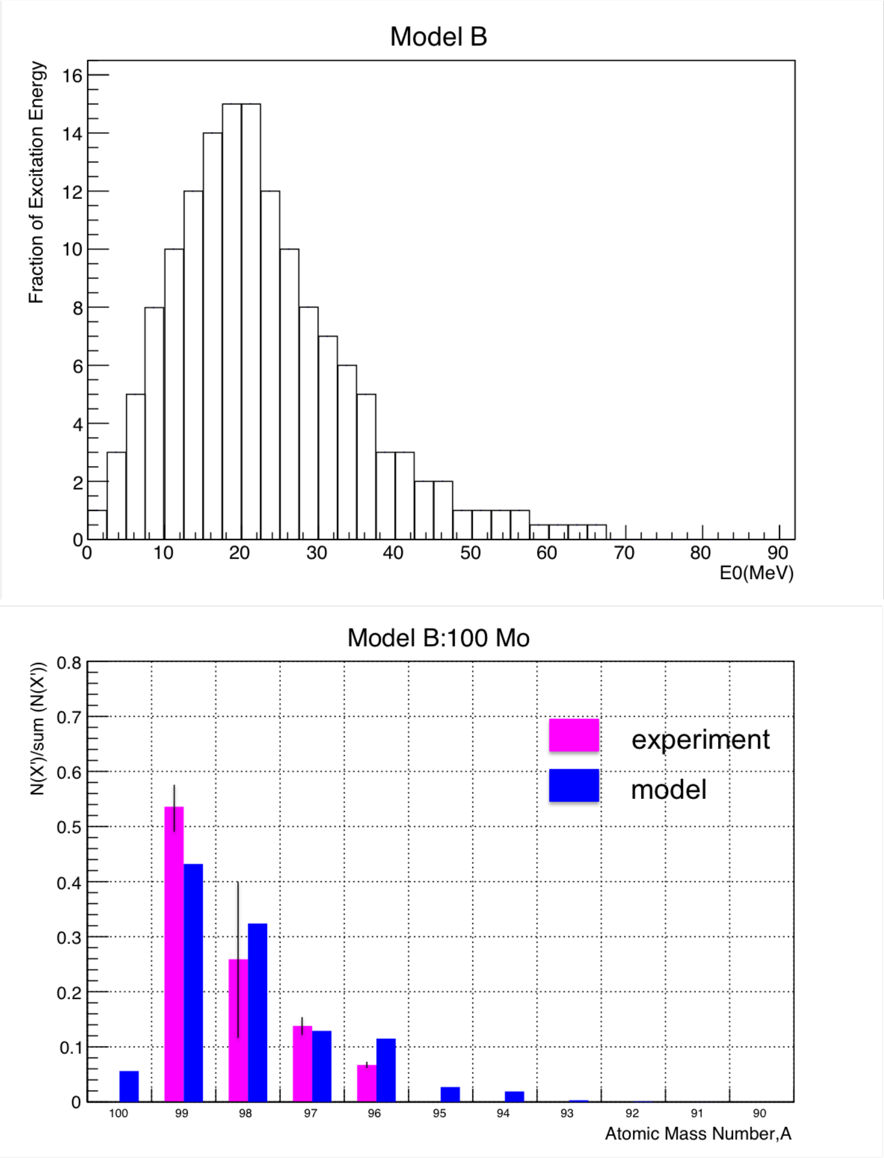

Figure 6.2: Model B: Nuclear excitation energy fraction and comparison model B with experimental observation by 100 Mo

Model C introduces the same excitation range as model B but the maximum excitation peak is in the range of 10 to 15MeV (see figure 6.3). It can be seen that all population generated by the statistical calculator resembles the experimental observation for MLF. The tail of isotope production which are far from the stability line (lower A) have begin to populate as a contribution of medium excitation energy tail is included.

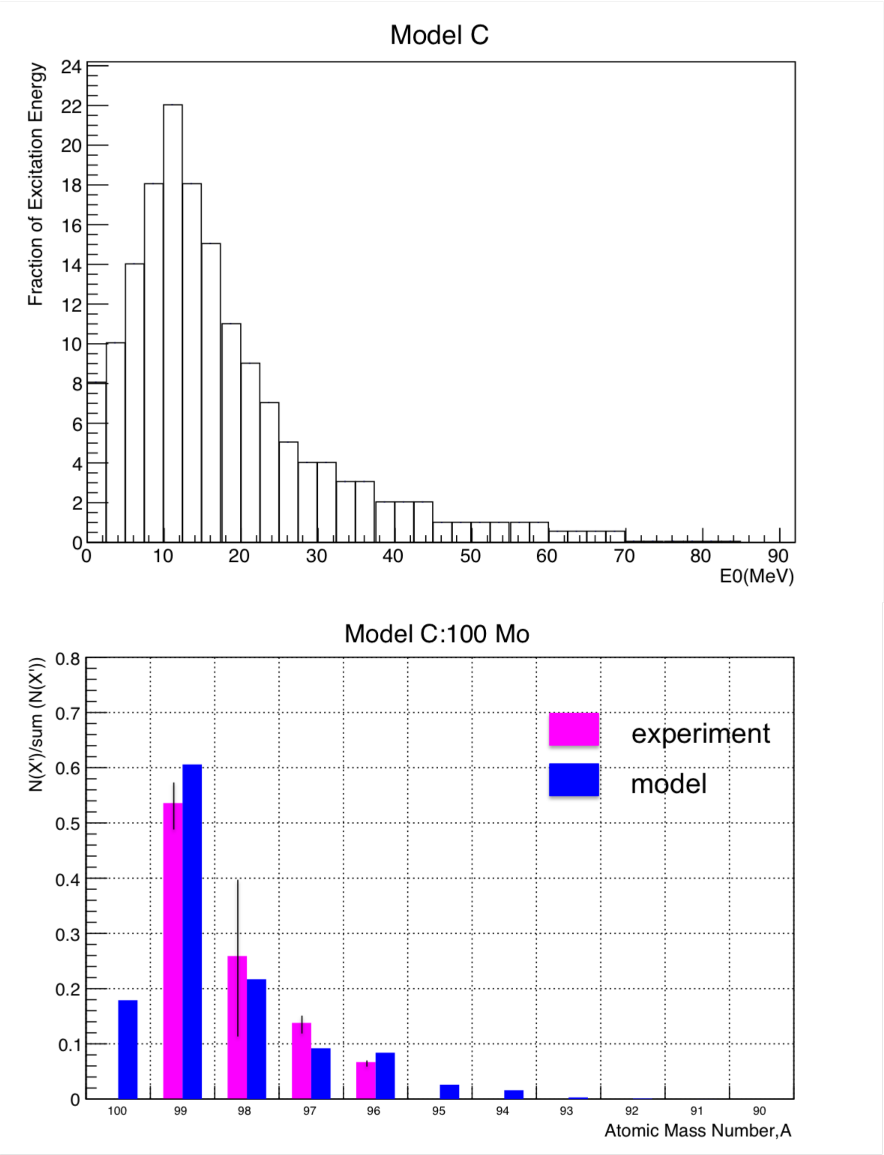

FIGURE 6.3: Model C: Nuclear excitation energy fraction and comparison model C with experimental observation by 100 Mo

In model D, the E_0 distribution is extended widely from 0 to 80MeV with the most probable excitation energy at 12.5MeV. The experimental results 100 Mo from MLF experiment was compared with the generated value from statistical calculator as shown by figure 6.4. The extended energy range increases the population of isotopes with low atomic mass number (A). From model C and model D, we can say that there is small portion of excitation energy tail during the real measurement.

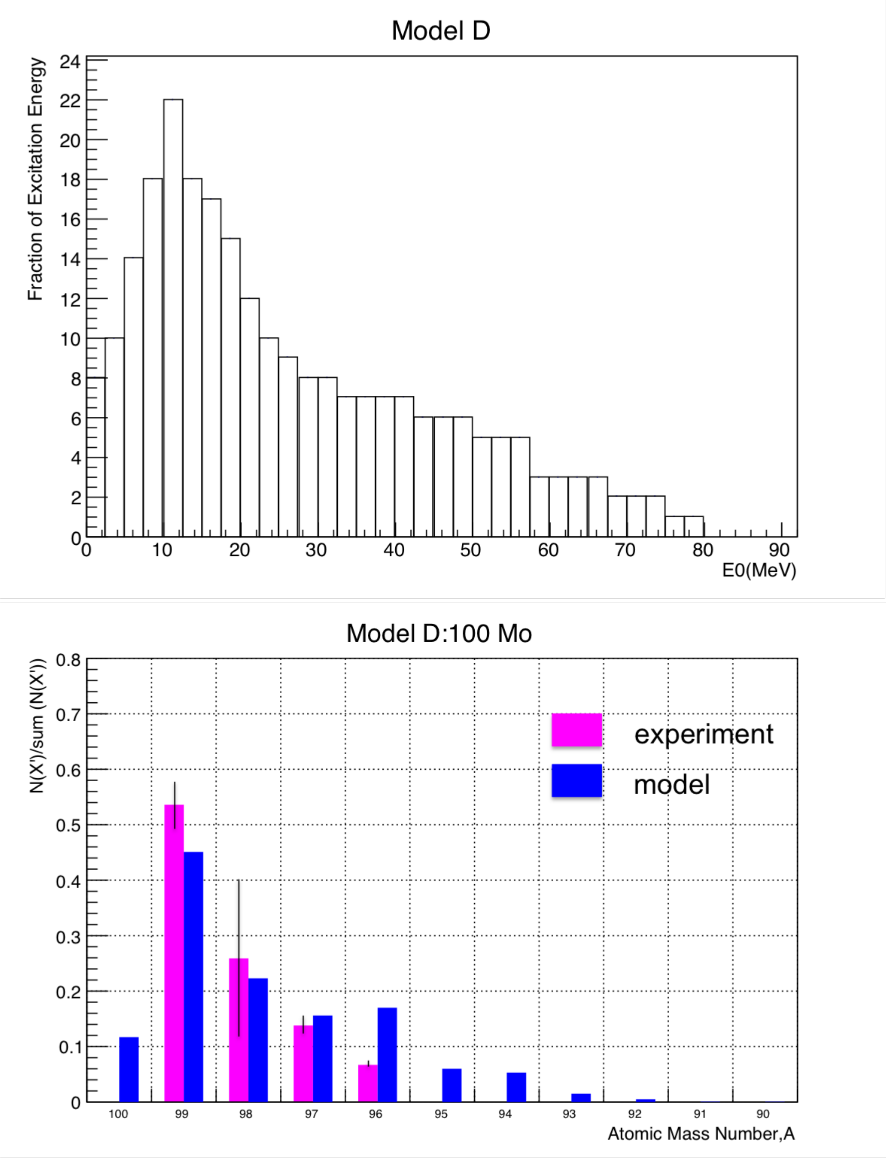

FIGURE 6.4: Model D: Nuclear excitation energy fraction and comparison model D with experimental observation by 100 Mo

Finally, model E is introduced to study the relationship of excitation energy with the phase space constant. The portion of E_0 is distributed from 0 to 90MeV with relatively decreases following (Q-E_0)^2. The observed model E was almost similar to model D as shown in figure 6.5. It can be conclude that the contribution of low excitation energy (0 to 10MeV) was nearly negligible due to the neutron binding energy which is sometimes higher than 10MeV.

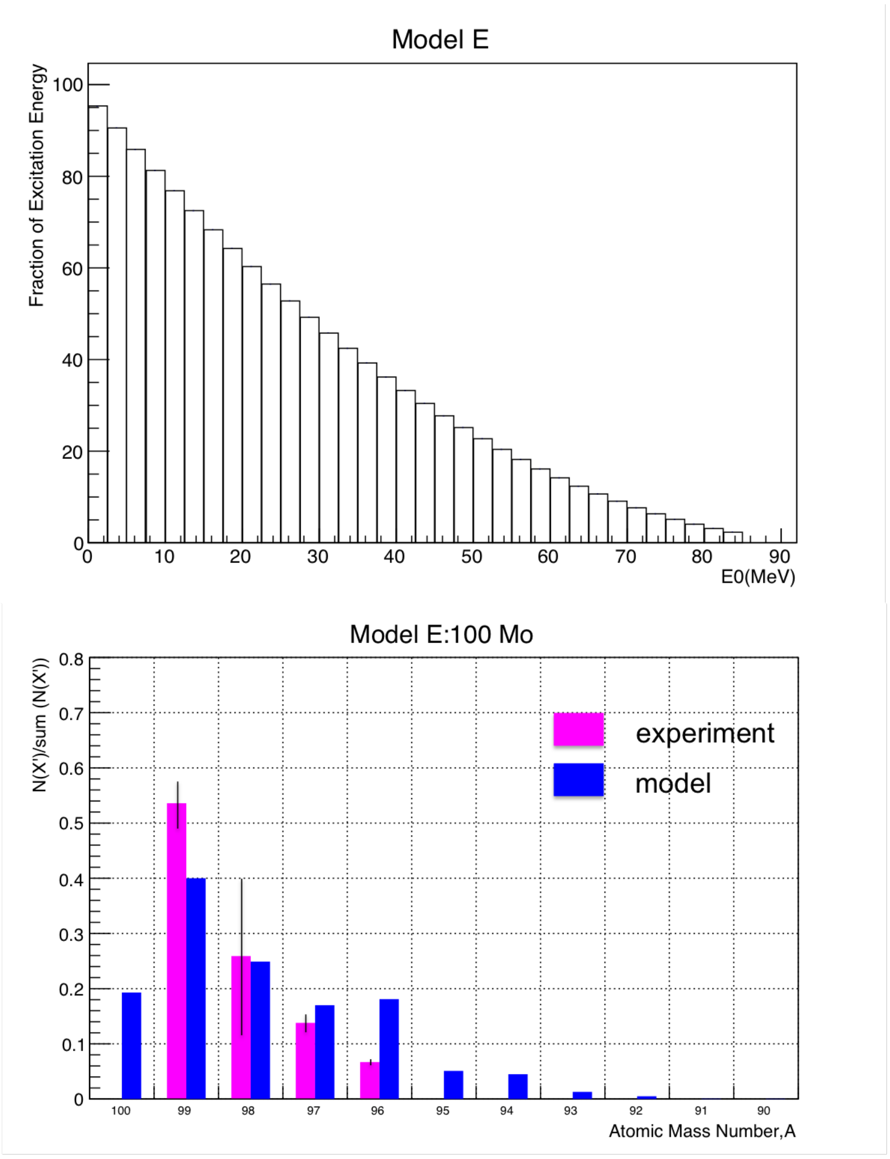

FIGURE 6.5: Model E: Nuclear excitation energy fraction and comparison model E with experimental observation by 100 Mo

From this 5 models, it can be conclude that model C shows the best agreement with the experimental observation in enriched molybdenum target. In order to quantitatively compare the population of 5 models, the χ^2 fitting is implemented to the isotope population. Table 6.1 indicates the χ^2 fit for all isotopes observed in the ^{100}Mo measurement. From this calculation we can see that the χ^2 values of isotopes in model C is within 1σ compare to other model which does not agree especially at isotope with A=99 and A=96.

$$\chi^2 = \sum_i \left(\frac{N_i^{data} - N_i^{model}}{\sigma_i^{data}}\right)^2 \tag{6.1}$$

We can comprehend that 1 neutron emission is a dominant process and 2 or 3 neutrons emission are reasonable in the reaction following nuclear muon capture. The excitation

Table 6.1: Chi-square fitting for all 5 models

Isotope	Model A	Model B	Model C	Model D	Model E
99	9.9	2.0	1.3	3.5	9.9
98	0.1	0.1	0.1	0.0	0.1
97	3.2	0.0	0.6	0.6	3.2
96	1.0	2.8	1.0	16.0	1.0
sum	14.0	4.9	3.0	20.0	14.0

energy range and maximum dominant peak plays important role in the isotope population distribution. However, if the maximum dominant peak is lower than the neutron binding energy, the effects is negligible.

The statistical calculation obtained from all the model is summarised in table 6.3. From the comparison of enriched molybdenum simulation and experimental results, it can confirmed that prediction of Mukhopadhyay [26] where the multiple excitation of nuclei have been occurred and dominant multipole excitations can be predicted even though we failed to explain the daughter level of preferential excitation.

Based on our observation the probability for zero neutron emission to the excited final states is 5% and the probability for single neutron emission following muon capture is observed to be ∼45%. These observation are in reasonable agreement with the results of G.R.Lucas [22] and reported by [17]. Two neutron and three neutron emission to excited states is observed to occur with 18-20% probability in agreement with the one calculated by S.Charalambous [40] from his study on stopping cosmic ray muons in the atmosphere and lithosphere. It is expected that the bound state is formed during the muon activation. In medium or heavy nuclei the bound state of the activated nuclei is close to each other, it would be difficult to distinguish each bound state.

Table 6.2: Calculated neutron emission probabilities.

Neutrons emission	0	1	2	3	4	5
Calculate by [40]	≤0.1	0.60-0.70	0.15-0.20	0.05	0.02	-
This Model	≤0.07	0.50-0.70	0.25-0.35	0.10	0.08	≤0.01

TABLE 6.3: Comparison of ratio to population of isotopes after muon capture reaction at MLF with neutron statistical calculator

A	MLF exp	Model A	Model B	Model C	Model D	Model E
100	-	(1.234±0.061)x10^{-4}	0.071±0.004	0.024 ±0.001	0.034±0.002	0.034±0.002
99	0.536±0.409	0.721±0.035	0.668±0.031	0.522±0.025	0.488±0.023	0.388±0.016
98	0.259±0.218	0.244±0.012	0.282±0.013	0.408±0.019	0.297±0.014	0.301±0.012
97	0.138±0.039	0.027±0.001	0.038±0.002	0.056±0.003	0.119±0.006	0.150±0.006
96	0.067±0.052	0.009±0.001	0.012±0.001	0.015±0.001	0.096±0.004	0.161±0.007
95	-	0.018±0.001	0.015±0.001	0.014±0.001	0.023±0.001	0.071±0.003
94	-	0.002±0.001	0.003±0.001	0.007±0.001	0.008±0.001	0.063±0.003

Chapter 7

Discussion and Concluding Remarks

Our aim from this study is to develop the experimental determination of neutrino nuclear response for NME study by the measurement of gamma rays following the muon capture reaction. In this chapter, we will provide discussion to the present achievement, problem we faced during the experiment, and the future prospect for this study. Finally, i will summarised the findings in the concluding remarks.

7.1 Achievements

7.1.1 Relative Weak Strength

Our main objective is to deduce absolute muon capture strength is still to be determined. However, this study provides the relative capture strength from the isotope population distributions and the NME determination is still far. The gross features of the weak strength distribution depends proportionally with the mass number. The current observation using ^{100}Mo showed the gross strength from relative population of observed isotope.

It have been emphasised by [22] that the relative abundance of excited isotopes after the muon capture process cannot measure directly the zero neutron emission population. Research by G.R.Lucas et al. [22] on the neutron emission following the muon capture on ^{142}Ce, ^{140}Ce, ^{138}Ba and ^{120}Sn shows the same patterns where 39 to 55% of isotope populates from one to three neutrons emission.

H.J. Evans [41] observed isotopes population on various atomic mass number from 28 to 196. From his observation, the most detected isotopes are from 1 neutron emission, 2 or 3 neutron emissions are also observed and a very small fraction of 1 neutron and 1 proton emission have been observed. Table 7.1 summarises the total isotope observed at [22] and [41].

In MLF beam test, we can said that we observed more than 70% of isotopes production after muon capture which causes the strength distribution is almost reproduced by theoretical estimation by neutron statistical model. From the strength distribution relative

Table 7.1: Comparison of total isotopes after muon capture reaction

Target	Resultant Isotope	Total Isotope(%)	Comments
^{28}Si	^{27}Al	16.0±3.0	[41]
^{48}Ti	^{48}Sc	11.1±0.9	[41]
	^{47}Sc	13.0±1.5	[41]
	^{46}Sc	8.1±1.0	[41]
	^{45}Sc	5.2±1.4	[41]
		$\sum$ 57.4±2.4	
^{89}Y	^{88}Sr	37.0±2.0	[41]
	^{87}Sr	5.7±1.1	[41]
		$\sum$ 42.7±3.1	
^{109}Ag	^{108}Pd	20.0±2.0	[41]
	^{106}Pd	6.4±1.4	[41]
	^{104}Pd	5.7±1.3	[41]
		$\sum$ 32.1±3.0	
^{142}Ce	^{142}La	0.9±0.2	[22]
	^{141}La	47.1±8.3	[22]
	^{140}La	4.2±1.0	[22]
	^{139}La	3.9±1.0	[22]
		$\sum$ 56.1±8.5	
^{138}Ba	^{138}Cs	2.0±0.4	[22]
	^{137}Cs	39.4±7.4	[22]
	^{136,138}Cs	10.0±1.4	[22]
	^{135}Cs	6.0±1.2	[22]
		$\sum$ 57.4±8.0	
^{197}Au	^{196}Pt	36.0±5.0	[41]
	^{194}Pt	3.2±0.8	[41]
		$\sum$ 39.2±2.2	

to the population of isotope of ^{100}Mo, we can deduced that the region of 8∼13MeV in excitation levels are strongly populated and this is supported by the neutron decay statistical calculation where excitation energy region of 10 to 15MeV. The same distribution observed previously by Columbia group for ^{209}Bi+μ reaction where the region of 6∼13MeV in excitation energy is strongly populated [14].

From this comparison, it can be conclude that this technique is reliable to observe more resultant isotope after the capture process. On the other hand, the neutron emission statistical model helps to estimate the absolute capture strength for isotope which are not observed during the experiment. However, we still requires more experimental data to deduce the initial excitation region involved during the reaction. Since the muon capture excited various modes of giant resonance, it is difficult to distinguish which strength responses are their origins. The muon capture lifetime measurement is required to estimate the absolute strength of the reaction.

7.2 Issues

7.2.1 Pile-up problems in short lived nuclei of ^{100}Nb, ^{99}Nb and X-rays measurement

For the on-beam measurements, the Nb nuclei are produced by the ^{100} Mo(μ,xn) reaction. At the present prompt gamma ray spectra, only a few Nb isomer have been observed after muon capture. The observed γ rays are well separated and the yields are as large as 10^5-10^6/ 10 hour. The observable of clear muonic X-ray carbon line is due to interaction of muon with the target holder. The muonic X-rays and known BG lines are presented as background contamination are identified, the remaining lines are assumed to be the γ ray transitions or unidentified BG lines which is in common to several prominent observations.

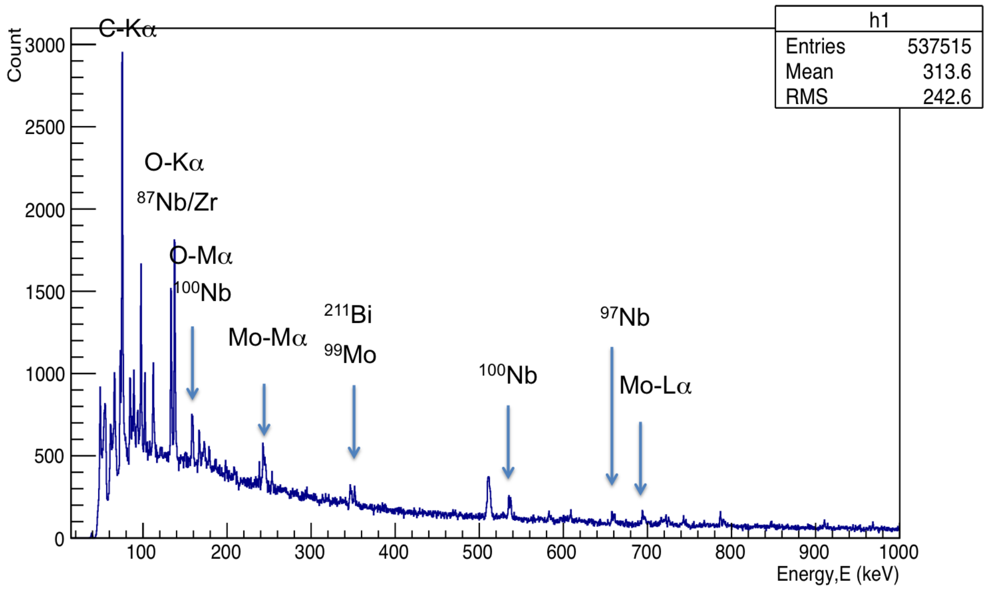

Figure 7.1: Energy spectra for on beam measurement

Muonic X-ray from carbon and oxygen contributed to high activity yield on 137keV and 159keV which also belongs to ^{99}Nb and ^{100}Nb. The effect of muonic X-ray causes the activity of gamma ray peaks to become larger and incomparable to higher gamma ray intensity from ^{100}Nb at 535keV. Due to muonic X-ray contamination, only 535keV peak is used to observe A=100 population.

The importance of observing the muonic X-ray is to ensure that the muon is capture by the target and we can study the total capture rates including neutron and proton emission reaction. The intensity of muonic X-ray Lα ($3d_{5/2}-2p_{3/2}$) is 0.70 ± 0.06 while the Mα muonic X-ray ($3p_{1/2}-2s_{1/2}$) observed at 242keV is 0.69 ± 0.08. Most of the observed muonic X-rays are in good agreement with the values estimated by muonic cascade calculator [25] and previous observation by Engfer et.al [21]. The energy shift observed in the transitions to the lowest level due to strong interactions with the nucleus. The errors are evaluated by propagating the uncertainties of the peak areas(statistical error) including the determination of energy calibration and detection efficiency function (10∼20%).

$$N_{stop} = P(stop) \times N_{yield} \tag{7.1}$$

The number of muon stopped in the sample is derived from the difference between the measurements for the sample and for the empty holder. The ratio of muon stopping efficiency is than simulated by Geant 4 (refer to Appendix A) and calculated the stopping muon by the above equation.

The 535keV gamma-rays from the on beam measurement corresponds to the zero neutron channel, came from isomeric transition in ^{100}Nb(1^+) → ^{100}Mo(g.s) and ^{100}Nb(5^+) → ^{100}Mo(g.s) which decay at half life of 1.5sec and 2.99sec [42] as shown in figure C.1 and C.2. The gamma rays are emitted following the cascade of 1391keV and 159.5keV in ^{100}Nb(1^+) → ^{100}Mo(g.s) and 1567.4keV and 549.7keV in ^{100}Nb(5^+) → ^{100}Mo(g.s). Due to the distance between the target and HPGe detector in on beam is large, the solid angle is small and caused the cascade effect to be negligible. The number of isotope from N(100) is (1.530±0.103)x10^6 obtained from the activation analysis.

On the other hand, 137.1keV gamma-rays is from the 1 neutron channel. It is important to know the isotope population value from the decay of ^{99}Nb, even though we also observed three gamma rays peak belongs to the isotope of A=99. The value from 137.1keV gamma-rays can be use for comparison and consistency check.

Table 7.2: Observed gamma and muonic X-ray at on beam measurement

Element	Transition	Energy,E (keV)	Half-life (sec)
Mo	Mα1	242.0	prompt
Mo	Lα2	695.0	prompt
Mo	Kα2	2682.0	prompt
^{100}Nb	$0^+ \to 2^+$	159.0 [42]	1.5s+2.99s
^{100}Nb	$2^+ \to 0^+$	535.6 [42]	1.5s+2.99s
^{99}Nb	$9/2^+ \to 9/2^+$ (g.s)	137.1 [32]	15.0s

The significant events lost due to the effects from gamma ray spectrometer system including the effects from germanium detector crystal, preamplifier, amplifier, analog-digital converter (ADC), multichannel analyser (MCA) or computer. This effects are generally refers as pile-up, which can be observe in the prompt gammas and X-ray "online" measurement. The short-lived gamma in few seconds to 100hours is measured in this MLF beam test.

The pile-up caused by the multiplicities of production particles such as muonic X-ray, neutron and gamma rays which produce in consequences to the capture reaction. These particles enters the HPGe detector at the same time, thus reduce the detected significant events. However, this pile-up events does not occur during the whole measurement. Sometimes only one gamma and one neutron enters the HPGe crystal causing the pile-up events effects is not so severe. At times where 4 or 5 gamma rays and neutrons emitted in total, the peak efficiency reduced due to multiple peak observation and caused the total events suppressed.

The pulse beam structure of D2 beam line, helps to detects 535keV and 137.1keV gamma rays belongs to A=100 isotope($\tau_{1/2}$=1.5sec and 2.99sec) and A=99 ($\tau_{1/2}$=15sec). The number of isotope calculated from prompt measurement is somehow in order of magnitude smaller than the one observed in off beam measurement. The isotope population produces by muonic X-ray was estimated to equal to the total production of isotope from A=95 to A=100 including gamma rays accompanied by proton emission, caused the gain change during the measurement, peak shift and pile-up problems the value is lower than expected.

The effects of pile-up in on-beam measurement contribute to net loss of 13% of the significant events. In order to reduce the pile up effects, we should placed the HPGe detector more farther than the target or use lower momentum muon and increases the irradiation time. We are hoping that the new MuSIC beam line might help to overcome the pile-up problem during the on beam measurement with clean and lower intensity muon beam irradiation.

7.3 Future Prospects

7.3.1 The new MuSIC beam line

At different beam structure, the total of gamma yield is almost similar either for continuous and pulse beam structure. From observation at MuSIC, the observed gamma yield was 10^6 events per 12 hours [16]. In current observation at MLF gamma yield 10^5 to 10^6 events per 12 hours which is much higher yield. On the other hand, the use of DC muon beam can help to gain information of muon capture reaction occurs between the pulsed beam which causes the pile up problem.

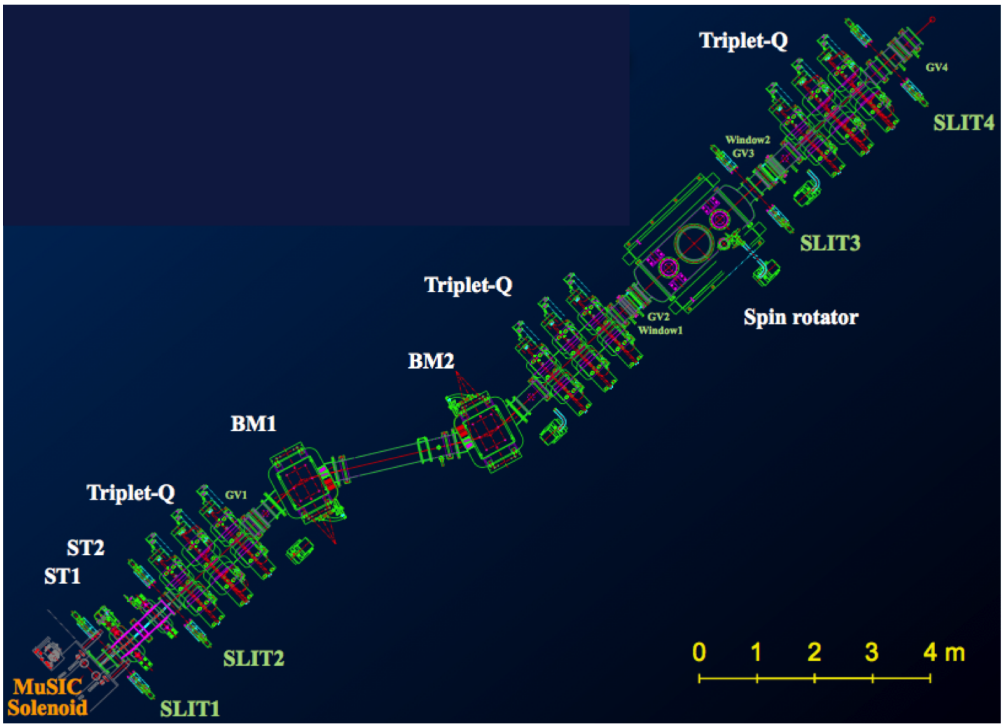

FIGURE 7.2: The new MuSIC beam line at RCNP, Osaka University

A complete MuSIC beam line might provide up to 10^4 clean and continuous muon beam which is slightly smaller than the muon beam intensity produced by J-PARC, MLF. The current negative muon beam momentum of 50MeV/c and positive muon beam of momentum 30MeV/c can help to provide steady muon beam for this kind of research. The lifetime measurement between production of muonic X-ray and gamma transition from excited state to the nuclear ground state can also be performed. The larger isotope range with prompt half-life and long half-life can be studied in larger variety of nucleus selection with different surface density since new MuSIC beam line provides wide momentum selection for various studies.

7.3.2 Prospects to deduce NME using ^{100}Mo data

In the current reports presented the observation of relative weak strength distribution from the RIs production rate. The final nuclear matrix element is not yet concluded since it is requires to study the phase space factor involving the excitation energy range by the neutron and neutrino emission and also the lifetime measurement at J-PARC, MLF is important to deduce the absolute muon capture strength.

The relative weak strength data provides by this reports can provides the final distribution of relative strength from muon capture reaction. The theoretical physicists are encouraged to reproduce the strength distribution by their theoretical model, especially Quasi-Particle Random Phase Approximation (QRPA) which is suitable for medium and heavy nuclei. If they successfully reproduces this distribution by their assigned coupling constant and spin isospin correlation parameters, they can say that their calculation are almost correct. If it does not reproduces this distribution, they need to adjust these parameters and finally check with the response from NME for deducing the coupling constant and spin isospin correlation parameters for DBD.

The value obtained in this study is not exactly the β^+ strength for DBD experiment but the it is relevant to be used for checking. This is caused by the DBD NME is a product of β^+ and β^- responses of NMEs, so the phase (either + or - phase) of NME is needed. However, the muon captures strength is the square of NME, thus it does not give the phase of NME.

7.3.3 Future Plan

In future, we plan to complete the data analysis of ^{93}Nb and ^{181}Ta which are also irradiated at J-PARC, MLF beam test. The relative strength of these samples will be evaluated by the neutron emission statistical model to get the initial excitation energy range. The measurement of ^{100}Ru is also needed to give the direct information about the β^+ side of DBD.

The short-lived gamma rays and muonic X-ray will be studied at the new MuSIC beam line and to get the absolute capture strength of ^{100}Mo. The life time measurements using pulsed muon beam is needed to deduce the absolute muon capture rate.

7.4 Application of Muon Capture Reaction

The muon capture reaction can be used to study a wide variety of science, for instance, from elementary particle physics, nuclear physics, and solid-state physics. It has been long since it is used for non-destructive trace elements analysis, archeology and chemistry and biology, and the energy-production issues.

This study mention in [16] that the muon capture reaction can also be used to study the isotope detection. Theoretical calculations of the weak nuclear responses (matrix elements) are not easy since they are very sensitive to nuclear correlations and nuclear medium effects. Thus, experimental studies of them are very valuable. Recent nuclear response of M(β^-) have been studied extensively by using high energy resolution charge exchange reaction by (^{3}He,t) reaction at RCNP. On the other hand M(β^+) requires highly sensitive probe like muon capture.

As a final remarks, we note that the Muon Capture Isotope Detection (MuCID) is a non-destructive detection (assay) of composite and impurity nuclear isotopes by measuring γ rays following muon capture reaction products is useful for the nuclear isotopes study of astro-nuclear and other of those particle physics, geological and historical interests and scientific point of view such as RPID [43] and μ-X rays for elemental assay [18] [21].

7.5 Summary

As a final conclusion, this present reports achieved to provide the new method to study the neutrino nuclear response information relevant to double beta decay experiments by nuclear muon reaction. Even though, this result are preliminary and does not include the isotope population from zero neutron channel.

a) The current enriched molybdenum irradiation results studies the excitation energy range of $E_0^e x = 0$ to 100 MeV by measuring the detailed γ-rays emission.

b) The muon probe is shown to be useful to study the neutrino nuclear response information relevant to double beta decay.

c) The $\mu - \gamma$ spectroscopy is reliable to study the higher momentum transfer responses of the intermediate nucleus of J$^\pi$ state of the intermediate nuclei of double beta decay in comparison with the lower momentum-transfer states observed by electron captures.

d) The isotope population from muon capture reactions are well studied from the delayed gamma rays from the decay of ^{99m}Tc, ^{98}Nb, ^{97}Nb and ^{96}Nb.

The neutron emission statistical model to study the initial excitation energy of the muon capture reaction is developed. The neutron statistical calculations successfully simulate the experimental results and estimate the absolute capture strength.

a) The neutron emission following muon capture reactions on natural molybdenum and enriched molybdenum showed that 1 neutron emission is dominant process and 2 or 3 neutron emissions are appreciable.

b) The statistical neutron decay model with different fraction of PEQ-EQ neutron stage gave small effects approximately less than 5% to the population of isotope at low lying level.

c) The dominant excitation is predicted at lower energy excitation around 10 to 15MeV.

d) The absolute strength of the capture reaction is still not been determined. Several more experiments especially towards the observation of zero neutron emission is required to determine the absolute β^+ strength.

The weak strength distribution shown by model C successfully agrees with the experimental observation with its maximum strength at 10 to 15 MeV and some strength at 20-30 MeV. The relative strength distribution, together with the muon capture lifetime can be used to evaluate muon capture responses (muon capture matrix elements) which are used help determine the nuclear responses for double beta decay.

Appendix A

Appendix A: Geant 4 Simulation

A Geant4 simulation package was used to estimate the probability of muon stopping, acceptance and peak efficiency of the experiment. At first we must try to reproduce the experimental setup as identical as possible. In this experiment, Mo target, trigger counter, detector Ge and shieldings are included in the simulation see figure *A*.1. The γ-ray was emitted isotropically from a random position within the sources. At this time, the energy of the γ-ray energy of X-ray you want to see each match (Mo-Mα: 242keV). The γ-rays are incident on the Ge crystal in the detector; the deposit energy due to the crystal drop was used to calculate the energy.

The muon stopping probability was define when the muon passing through the upstream counter and stop on the target. In this estimation, muon beam was generate at the end of solenoid exit and two virtual detector was placed as upstream and downstream trigger

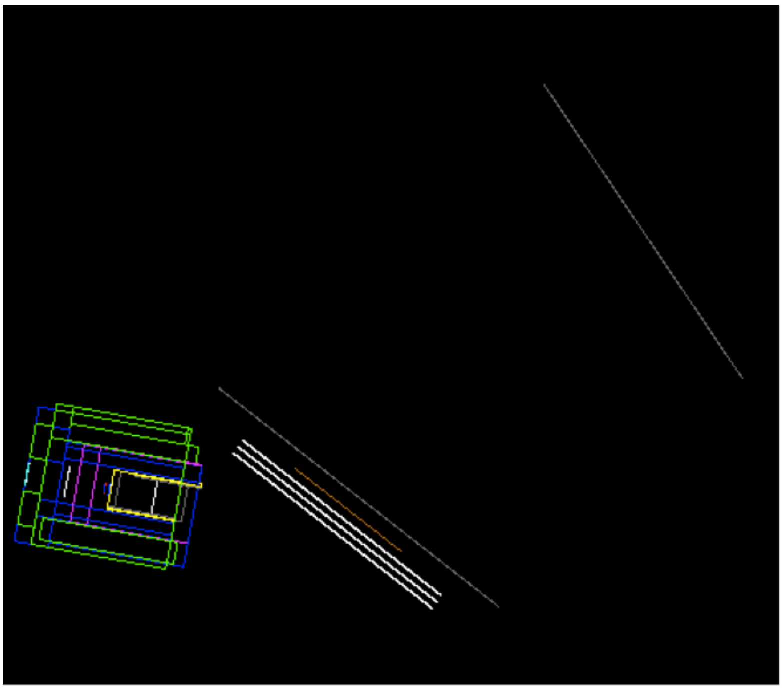

Figure A.1: Geant 4 simulation estimation of probability of muon stopping, acceptance and peak efficiency.

counter. The stopping probability,

$$\eta_{stop} = \frac{Number of muon stop on target}{Number of hit at upstream counter}.$$

The acceptance define as how many emission enters the detector as the gamma emitted isotropically from the target. Acceptance or so called solid angle was defined as below

$$\frac{\Omega}{4\pi} = \frac{number of hit on detector}{total particle emission}.$$

The peak efficiency corresponds to the ratio of the number of counts in full energy peak at a particular energy by the number of photons with energy, E emitted by the source (F(E)).

$$\epsilon_{peak} = \frac{total event at full energy peak}{fraction of peak from total number of emitted particle}$$

Appendix B

Appendix B: Energy calibration Source

The energy calibration run was taken in every experiment in order to check the acceptance and efficiency of each peak. A standard source was used to check the peak efficiency of data and compared with the simulation. The date of manufactures of the source is very important in order to know the current activity of each gamma peak. The suitability of selecting the source for energy calibration is depending on the range of expected gamma ray from the irradiation and also the availability of the source and its detail information.
Manufactured date: December 16,1988.
Half-life: 10.51years.

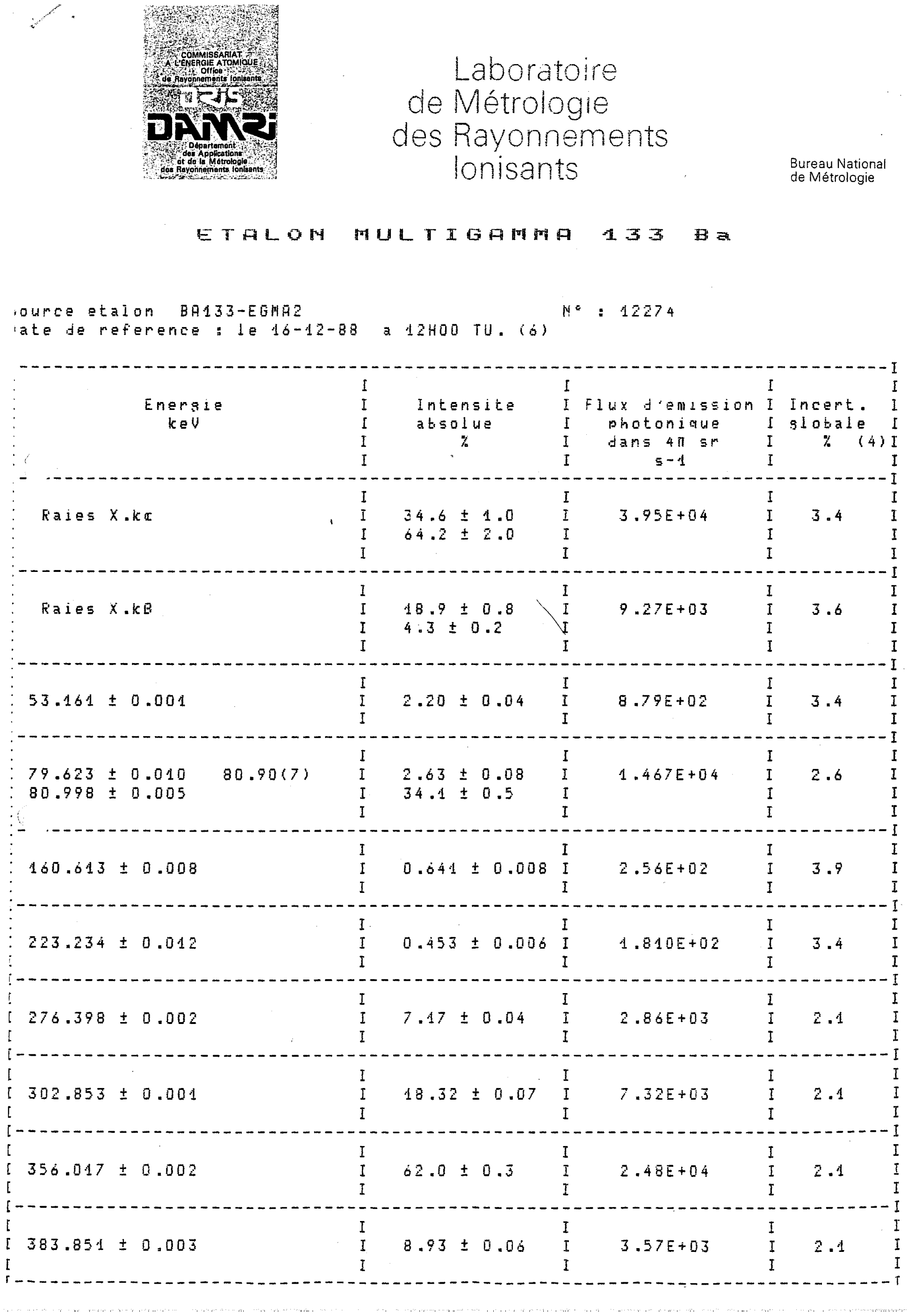

COMMISSARIAT A L'ENERGIE ATOMIQUE
Office de Rayonnements Ionisants
DAMRI
Département des Applications et de la Métrologie des Rayonnements Ionisants

Laboratoire
de Métrologie
des Rayonnements
Ionisants

Bureau National
de Métrologie

ETALON MULTIGAMMA 133 Ba

ource etalon BA133-EGMA2 N° : 12274
ate de reference : le 16-12-88 a 12H00 TU. (6)

Energie keV	Intensite absolue %	Flux d'emission photonique dans 4π sr s-1	Incert. globale % (4)
Raies X.kα	34.6 ± 1.0 64.2 ± 2.0	3.95E+04	3.4
Raies X.kβ	18.9 ± 0.8 4.3 ± 0.2	9.27E+03	3.6
53.161 ± 0.001	2.20 ± 0.04	8.79E+02	3.4
79.623 ± 0.010 80.90(7) 80.998 ± 0.005	2.63 ± 0.08 34.1 ± 0.5	1.467E+04	2.6
160.613 ± 0.008	0.641 ± 0.008	2.56E+02	3.9
223.234 ± 0.012	0.453 ± 0.006	1.810E+02	3.4
276.398 ± 0.002	7.17 ± 0.04	2.86E+03	2.1
302.853 ± 0.001	18.32 ± 0.07	7.32E+03	2.1
356.017 ± 0.002	62.0 ± 0.3	2.48E+04	2.1
383.851 ± 0.003	8.93 ± 0.06	3.57E+03	2.1

FIGURE B.1: Calibration source for MLF measurement

Appendix C

Appendix C: Properties of Radio Isotopes

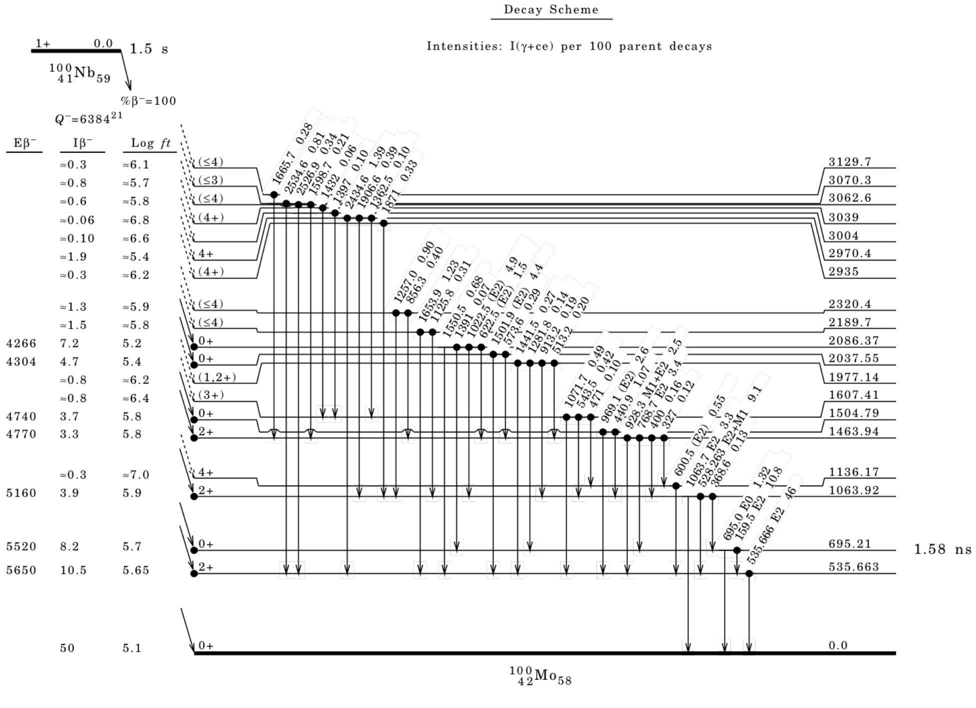

FIGURE C.1: Level diagram of ^{100}Mo[50]

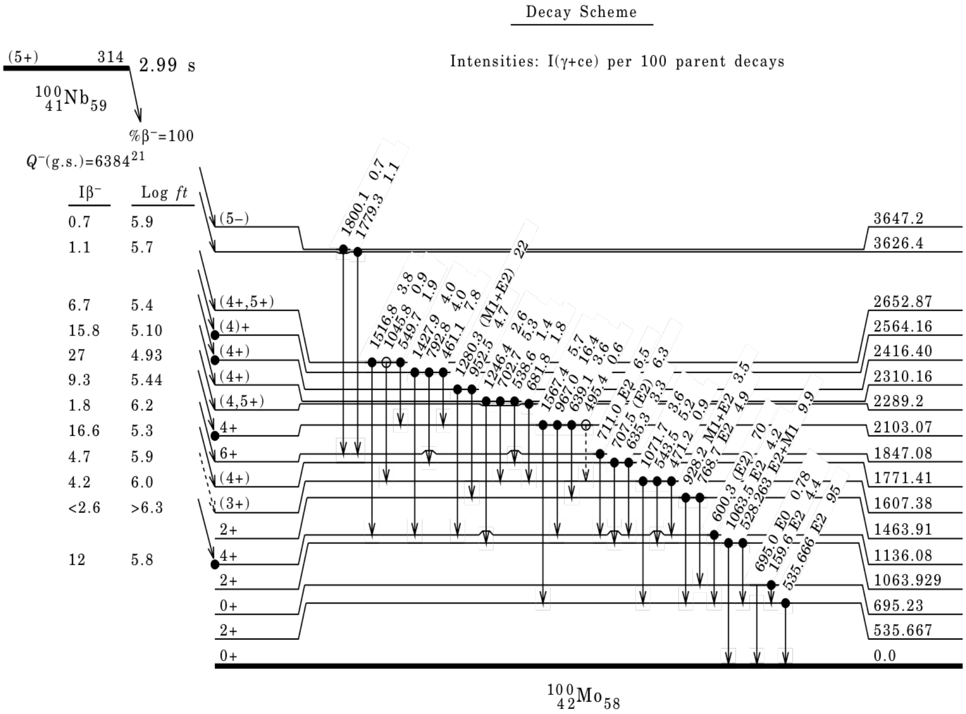

FIGURE C.2: Level diagram of ^{100m}Mo[50]

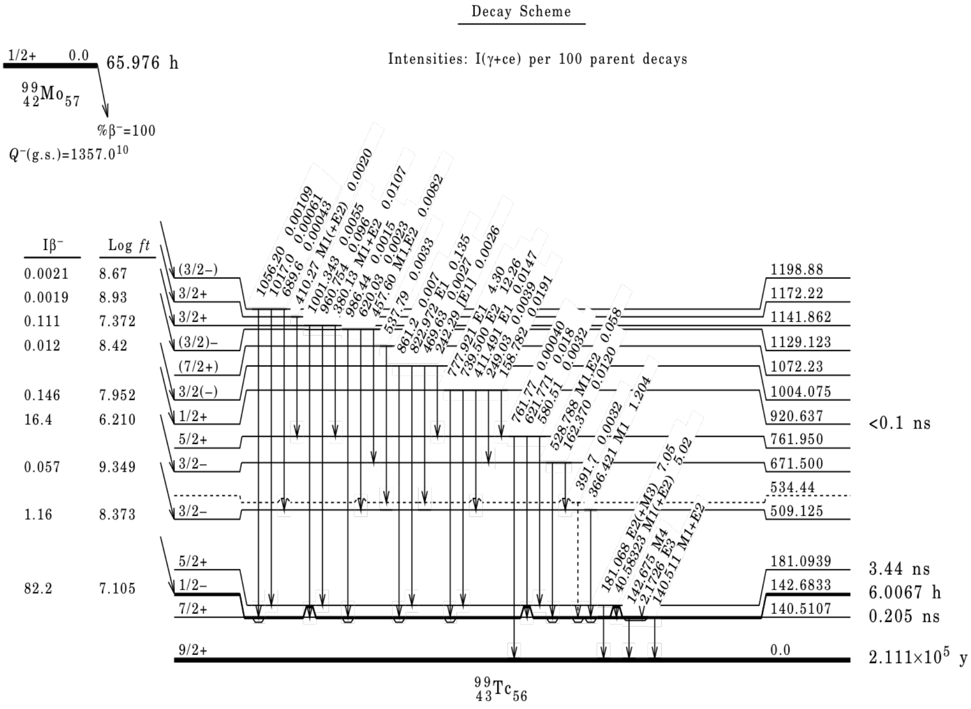

FIGURE C.3: Level diagram of ^{99}Mo [43]

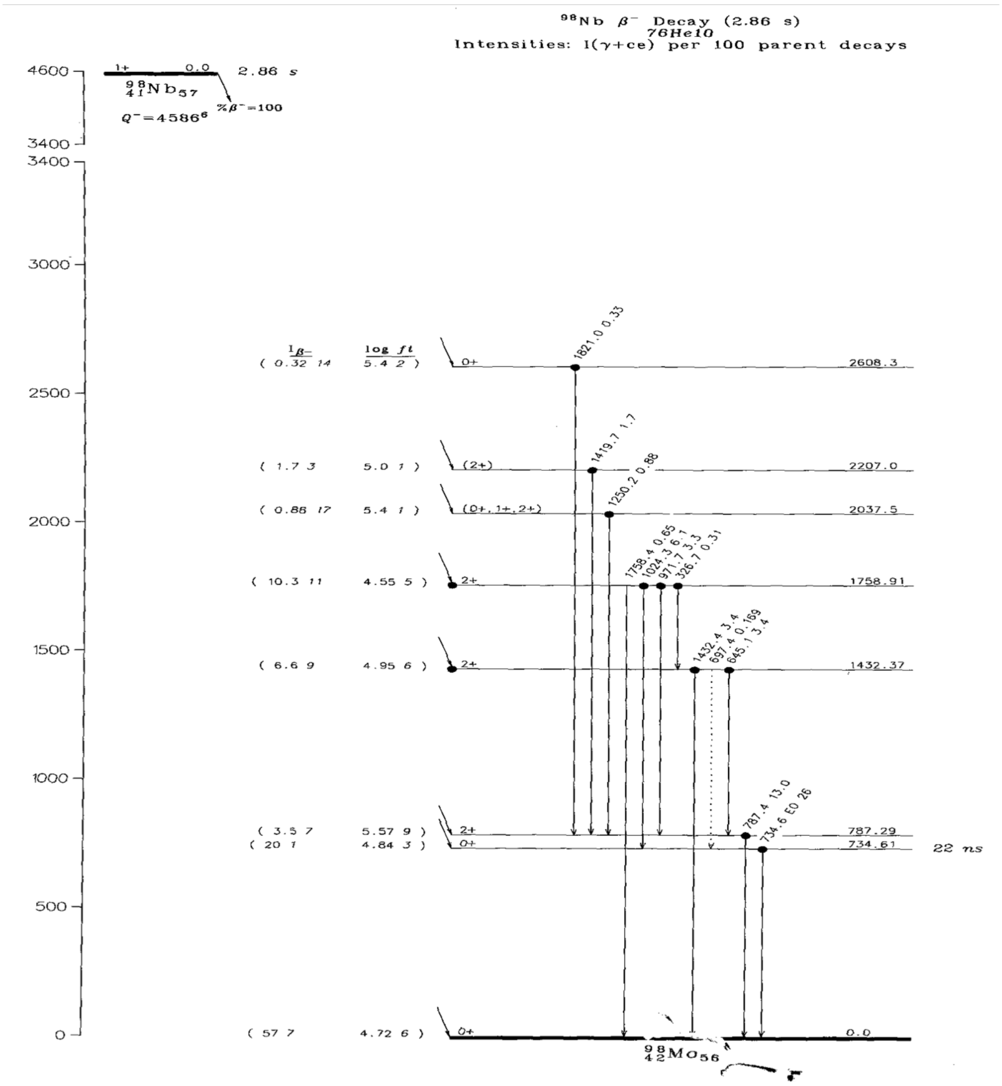

FIGURE C.4: Level diagram of ^{98}Mo [39]

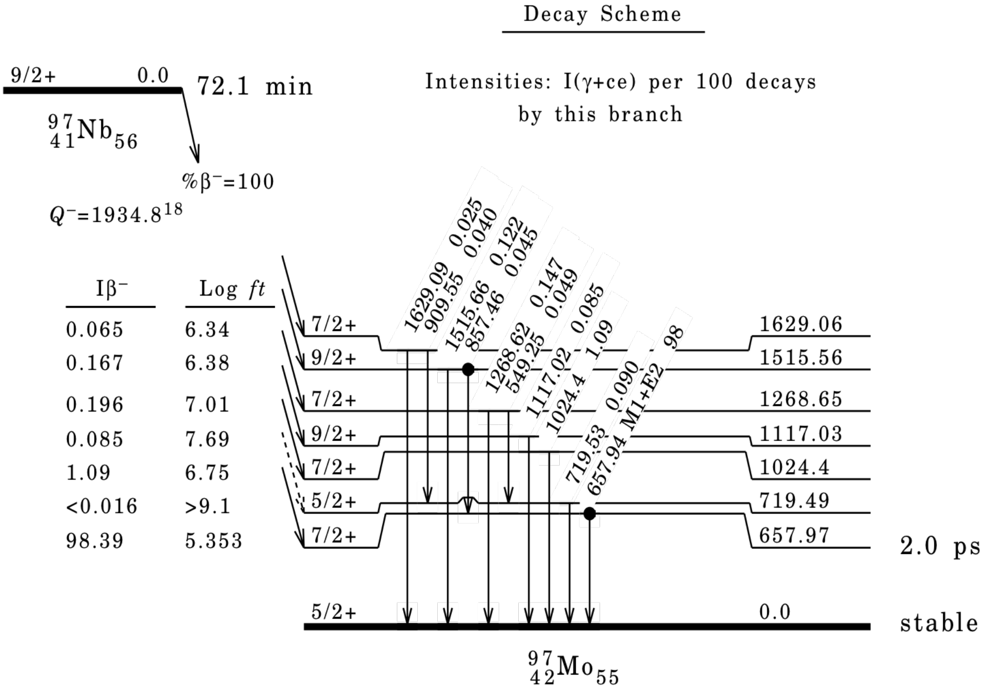

FIGURE C.5: Level diagram of ^{97}Mo [40]

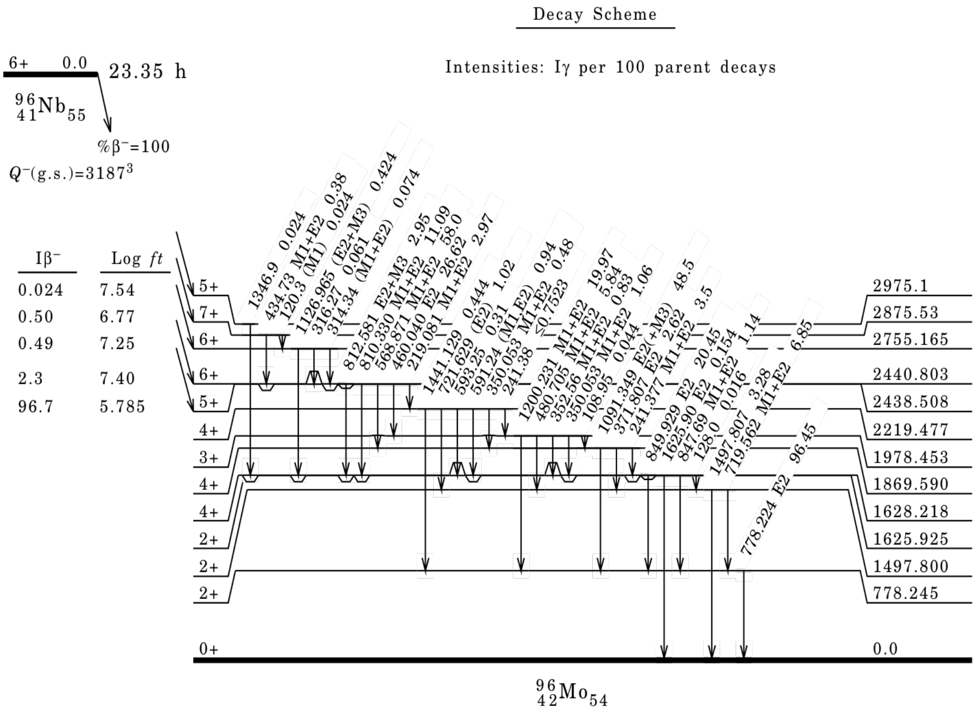

FIGURE C.6: Level diagram of ^{96}Mo [41]

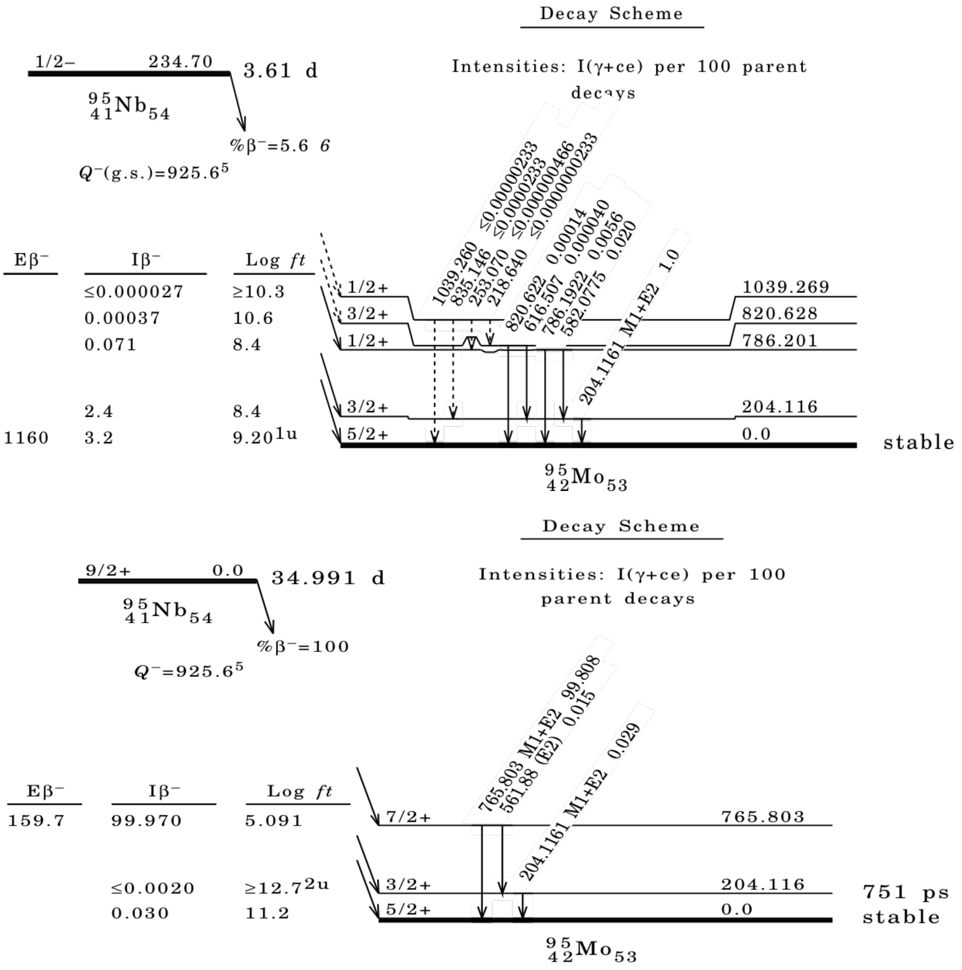

FIGURE C.7: Level diagram of (a) ^{95}Mo (b)^{95m}Mo [42

Bibliography

[1] F.Close. *Neutrino*. Oxford University Press, Oxford, NY, 2010.

[2] G.Rajasekaran. Fermi and the theory of weak interactions. *History and Philosophy of Physics*, 19(1):18–44, January 2014. URL `http://arxiv.org/abs/1403.3309v1`.

[3] F.Reines. A brief history of neutrino experiment at lampf. Los Alamos Science, 1997.

[4] J.D Vergados, F.Simkovic, and H.Ejiri. Theory of neutrino less double-beta decay. *Reports on Progress in Physics*, 75(10):1–52, September 2012. URL `http://iopscience.iop.org/0034-4885/75/10/106301/`.

[5] H.Ejiri. Double-beta decays and neutrino masses. *Progress in Particle and Nuclear Physics*, 48(00124):185–200, November 2002.

[6] H.Ejiri. Double beta decays and neutrino masses. *Journal of Physical Society of Japan*, 74(8):2101–2127, August 2005.

[7] H.V. Klapdor-Kleingrothaus and A. Staudt. *Non-accelerator Particle Physics*. Oxford Science Publications, Oxford, NY, 1998.

[8] H.Yoshida. *Limit on Majorana Neutrino Mass with Neutrinoless Double Beta Decay from KamLAND-Zen*. Tohoku, Japan, 2013.

[9] M. Kortelainen and J.Suhonen. Ordinary muon capture as a probe of virtual transitions of double beta decay. *Europhys. Letter*, (58):666–672, January 2002. URL `http://arXiv:nucl-th/0201007`.

[10] M. Kortelainen and J.Suhonen. Microscopic study of muon capture transitions in nuclei involve in double beta decay processes. *Nuclear Physics A*, 2(713):501–521, September 2003. URL `http://doi:10.1016/j.nuclphysbps.2005.01.216`.

[11] M. Kortelainen and J.Suhonen. Probing double beta decay by nuclear muon capture. *Nuclear Physics B Proceeding Suppl.*, 2(143):551, January 2005. URL `http://doi:10.1016/j.nuclphysbps.2005.01.216`.

[12] H.Ejiri and M.J.A de Voigt. *Gamma-Ray and Electron Spectroscopy in Nuclear Physics*. Oxford Science Publications, Oxford, NY, 1989.

[13] J.Schweiger et al. Double beta decay to excited states in 76ge within renormalized qrpa. *Journal of Physics G: Nuclear and Particle Physics*, 23(11):1647, November 2012. URL `http://doi:10.1088/0954-3899/23/11/012`.

[14] H.Ejiri. Isospin core polarization and charge exchanged giant resosnances. *Research Report of Laboratory of Nuclear Science*, 5(1):261–271, 1972.

[15] H.Ejiri. Muon induced reaction for gamma-rays spectroscopy. *Meson*, (39):44–49, 2014.

[16] Hiroyasu Ejiri and I.H.Hashim et. al. Nuclear gamma rays from stopped muon capture reactions for nuclear isotope detection. *Journal of Physical Society Japan*, 82 (044202):1–5, March 2013. URL `http://dx.doi.org/10.7566/JPSJ.82.044202`.

[17] D.F. Measday. The nuclear physics of muon capture. *Physics Reports*, 354:243–409, December 2001.

[18] K.Ninomiya et. al. Development of elemental analysis by muonic x-ray measurement in j-parc. *Journal of Physics:International Symposium on Advanced Science Research 2009*, 225(012040):1–4, 2010.

[19] G.L. Borchert et. al. High precision spectroscopy of pionic and muonic x-rays to extract an upper limit for the muon-neutrino mass. *Acta Physica Polonica B*, 29: 131–139, 1998.

[20] P.Singer. *Emission of particles following muon capture in intermediate and heavy nuclei*. Haifa, Israel, 1973.

[21] R.Engfer et. al. Charge-distribution parameters, isotope shifts,isomer shifts and magnetic hyperfine constants from muonic atoms. *Atomic Data and Nuclear Data tables*, 14(5):509–597, 1974.

[22] G.R.Lucas and Jr. P. Martin et al. Neutron emission following muon capture in ^{142}ce, ^{140}ce, ^{138}ba and ^{120}sn. *Physical Review C*, 7(4):1678–1686, April 1973.

[23] V.Devanathan. *Observable in nuclear muon capture*. World Scientific, Osaka, Japan, 1989.

[24] F.Myhrer S.I.Ando and K.Kubodera. Capture rate and neutron helicity asymmetry for ordinary muon capture on hydrogen. *Physical Review C*, 63(015203):1–7, December 2000. URL `http://doi:10.1103/PhysRevC.63.015203`.

[25] P.Vogel. Muonic cascade:general discussion and application to the third row elements. *Physical Review A*, 22(4):1600–1609, October 1980.

[26] Nimai C. Mukhopadhyay. Nuclear muon capture. *Physics Reports*, 30(1):1–144, July 1977.

[27] Glenn F.Knoll. *Radiation detection and measurement*. John Wiley and Sons Inc., Michigan, USA, 2003.

[28] W.R.Leo. *Techniques for nuclear and particle physics experiment*. Springer-verlag Publications, Switzerland, 1994.

[29] H.Ejiri and I.H.Hashim. et. al. Nuclear weak responses by measuring gamma rays from muon capture reactions. Proposal for MLF J-PARC, 2013.

[30] N.Kudomi and T.Shima et al. Preparation of large and thin source films for studying nuclear rare decays. *Nuclear Instruments and Methods in Physics Research A*, 322: 53–56, April 1992.

[31] P. Bossew. A very long-term hpge-background gamma spectrum. *Applied Radiation and Isotopes*, 62:635–644, 2005.

[32] E.Browne and J.K.Tuli. Nuclear data sheets for a=99*. *Nuclear Data Sheets*, 112: 275–446, 2011.

[33] Balraj Singh. Nuclear data sheets update for a=98*. *Nuclear Data Sheets*, 67: 693–807, 1992.

[34] N.Nica. Nuclear data sheets for a=97*. *Nuclear Data Sheets*, 111:525–716, 2010.

[35] D. Abriola and A.A.Sonzogni. Nuclear data sheets for a=96*. *Nuclear Data Sheets*, 109:2501–2655, 2008.

[36] G.Mukherjee S.K. Basu and A.A.Sonzogni. Nuclear data sheets for a=95*. *Nuclear Data Sheets*, 111:2555–2737, October 2010.

[37] Herbert R. Faust. Fragment excitation, kinetic energy distributions and neutron evaporation in nuclear fission calculated from a random excitation model. *International Journal of Modern Physics E*, 13(1):1–6, Oct 2003.

[38] R.Raphael and H.Uberall et al. Neutron emission following muon capture in 16 o. *Physics Review Letters B*, 24(1):15–18, December 1966.

[39] MacDonald and S.N. Kaplan et al. Neutrons from negative muon capture. *Physical Review*, 139(5B):1253–1263, September 1965.

[40] S.Charalambous. Nuclear transmutation by negative stopped muons and the activity induced by the cosmic-ray muons. *Journal of Nuclear Physics A*, 166:145–161, July 1971.

[41] H.J.Evans. Gamma rays following muon capture. *Nuclear Physics A*, (207):379–400, March 1972.

[42] Balraj Singh. Nuclear data sheets for a=100*. *Nuclear Data Sheets*, 109:297–516, 2008.

[43] Hiroyasu Ejiri and Tatsushi Shima. Resonant photo nuclear isotope detection using medium-energy photon beam. *Physical Review Special Topics - Accelerator and Beams*, 15(024701):1–6, Feb 2012. URL `http://dx.doi.org/10.1103/PhysRevSTAB.15.024701`.